Università degli Studi di Padova

Centro Interdipartimentale "Centro Ricerche Fusione"

Universidade de Lisboa

Instituto Superior Técnico (IST)

JOINT EUROPEAN RESEARCH DOCTORATE IN FUSION SCIENCE AND ENGINEERING

Cycle XXIX

Advanced Tools for Three-Dimensional Modeling and Control of Thermonuclear Fusion Devices

Coordinator:

Prof. Paolo Bettini

Supervisors:

Dr. Tommaso Bolzonella

Prof. Paolo Bettini

Prof. Bernardo Brotas de Carvalho

Ph.D. Student: Leonardo Pigatto

Padova, January 2017

UNIVERSITÀ DEGLI STUDI DI PADOVA

JOINT EUROPEAN RESEARCH DOCTORATE IN FUSION SCIENCE AND ENGINEERING

Network Partners:

- Instituto Superior Técnico (IST) Lisboa, Portugal
- Università degli Studi di Padova, Italy
- Ludwig-Maximilians-Universität München, Germany

In collaboration with:

- Consorzio RFX, Italy
- IPP Garching, Germany

Leonardo Pigatto: *Advanced Tools for Three-Dimensional Modeling and Control of Thermonuclear Fusion Devices*, , January 2017

To my grandmother Teresa

To the loving memory of my grandmother Angela

FOREWORD

The research work presented in this thesis has been carried out at Consorzio RFX in Padova, within the framework of a European Research Doctorate in Fusion Science and Engineering. During the last few years I have been given the chance to develop professional skills and experience in research, thanks to the people that I have met and worked with along the way. The most obvious purpose of this thesis is to draw the conclusions of a long journey that has nevertheless gone by very fast. As a secondary objective, I would like to convey my personal satisfaction for the work done and my passion for the subject. As a small note on the text itself, the structure of the manuscript reflects the evolution of my activities in time, with the exception of the introductory part in which I tried to summarize the main background concepts in a neither lengthy nor simplistic way. I hope I have found a good compromise that does not fall into boredom. In the core chapters following the introduction, papers and conference contributions where the content has been presented are explicitly mentioned. I have made this choice to highlight where and when the results have been presented to the community. I have also added a quotation at the beginning of each chapter, taken from some of my favorite classical and contemporary authors. These quotes do not necessarily refer to the content of the chapters as much as they are meant for entertainment and inspiration, which I often find to be lacking in scientific literature. I hope the reading of this thesis will be enjoyable as well as interesting.

Padova, January 2017

Ergo vivida vis animi pervicit, et extra
processit longe flammantia moenia mundi
atque omne immensum peragravit mente animoque,
unde refert nobis victor quid possit oriri,
quid nequeat, finita potestas denique cuique
quanam sit ratione atque alte terminus haerens.

— Titus Lucretius Carus, De Rerum Natura

ABSTRACT

This thesis represents the summary of the research activities carried out during a three-years Ph.D. project. The work is divided into two parts, with the common feature of investigating the physical properties related to stability and control of Magneto-Hydro-Dynamic modes in fusion relevant plasmas. One of the aims of the work is to better understand the interaction between such plasmas and a wide range of 3-dimensional electro-magnetic boundary conditions. This part of the research has been carried out on the RFX-mod device, where advanced control strategies have been developed thanks to its state-of-the-art magnetic feedback system. A variety of interlaced problems have been addressed, starting with the improvement of the vacuum magnetic field spectrum through actuator-sensor decoupling, compensation of broken or deactivated coils with simple and real-time applicable strategies and multi-modal Resistive Wall Mode control with varying coil number and geometry. This has allowed to develop relevant control optimization techniques and knowledge for both the Reversed Field Pinch and Tokamak configurations. The former is an excellent playground for RWM studies, given the instability spectrum that is naturally developing. For the latter configuration instead, RWM stability is considered to be one major milestone to be achieved along the road to a commercial fusion reactor. The second part of the work is dedicated to this issue, and deals with the stability properties of Advanced Tokamak scenarios, with reference to the JT-60SA experiment in particular. Studies to understand RWM physics in high β plasmas, where fluid rotation profiles and hot ions populations from Neutral Beams can play an important role, have been carried out with the MARS-F/K linear MHD codes. If detailed physics such as kinetic effects is coupled to a simplified description of the passive/active structures

on one side, on the other hand a simplified plasma can be coupled to a complex 3-D model of the structures to assess realistic active control capabilities of a given system. Different tools are used and described for studying RWM damping physics, and to five a proof-of-principle for feedback control of such instabilities in Advanced Tokamak plasmas operating beyond the no-wall pressure limit.

SOMMARIO

Questa tesi rappresenta la raccolta delle attività svolte durante i tre anni di un progetto di Dottorato di Ricerca. Il lavoro è stato diviso principalmente in due parti, con il comune denominatore di investigare le problematiche relative alla stabilità e al controllo di instabilità Magneto-Idro-Dinamiche in plasmi di interesse fusionistico. Uno dei principali obiettivi di questo lavoro è lo studio di come questi plasmi interagiscano con diverse condizioni al contorno, strutturali ed elettro-magnetiche, con caratteristiche tridimensionali. Questa parte della ricerca è stata svolta sull'esperimento RFX-mod, dove è stato possibile sviluppare peculiari strategie di controllo grazie all'avanzato sistema di controllo attivo. Sono state affrontate varie problematiche tra loro interconnesse, a partire dallo sviluppo di tecniche per il miglioramento del contenuto armonico dei campi magnetici di vuoto tramite disaccoppiamento attuatori-sensori. Da ciò è stato sviluppato un metodo semplificato e applicabile in tempo reale per la compensazione di attuatori rotti o disattivati, con il medesimo obiettivo di migliorare il contenuto armonico dei campi magnetici prodotti dal sistema di controllo reale. A conclusione di questa parte il controllo multi-modale di modi di parete resistiva (RWM) è stato affrontato, dal punto di vista modellistico e sperimentale. Le strategie sviluppate e gli studi effettuati sono rilevanti sia per la configurazione Reversed Field Pinch sia per il Tokamak. Il primo è un ottimo terreno di prova per studiare i modi RWM, per via dello spettro di instabilità che naturalmente sviluppa. Per la seconda configurazione invece, la stabilizzazione dei modi RWM è considerato uno dei principali obiettivi da raggiungere sulla strada verso un reattore a fusione commerciale. La seconda parte del lavoro è relativa proprio alla problematica della stabilità RWM nella configurazione Tokamak, in particolar modo negli scenari

avanzati in fase di sviluppo per l'esperimento JT-60SA. Una serie di studi è stata portata avanti con i codici MARS-F/K per determinare le proprietà dei modi RWM in plasmi ad alto β, nei quali i profili di rotazione e le popolazioni di ioni sovra termici provenienti dagli iniettori di neutri possono giocare un ruolo importante. Da un lato una descrizione dettagliata del plasma, includendo gli effetti cinetici, è stata accoppiata a un modello semplificato e bidimensionale delle strutture passive. D'altra parte una più semplice descrizione del plasma è stata considerata per l'accoppiamento con un modello dettagliato e tridimensionale delle strutture attive e passive, in quest'ultimo caso è stato possibile sviluppare un modello di controllo attivo in catena chiusa dei modi RWM.

RESUMO

Esta tese representa o resumo das atividades de pesquisa realizadas durante um projeto de doutorado de três anos. O trabalho é dividido em duas partes com a característica comum de investigar as propriedades físicas relacionadas à estabilidade e ao controle dos modos magnetoidrodinâmicos em plasmas relevantes para fusão. Um dos objetivos do trabalho é entender melhor as interações entre estes plasmas e um amplo intervalo de condições de contorno eletromagnéticas tridimensionais. Essa parte da pesquisa foi realizada no dispositivo RFX-mod onde avançadas estratégias de controle foram desenvolvidas graças ao seu moderno sistema de *feedback*. Uma variedade de problemas entrelaçados foi abordada começando pela melhora do espectro de campo magnético no vácuo através do desacoplamento atuador-sensor, compensação de bobinas danificadas ou desativadas com estratégias aplicáveis simples e em tempo real e controle de multimodal Resistive Wall Mode com numero de bobina e geometria variável. Isso permitiu o desenvolvimento de relevantes técnicas de controle e otimização e o conhecimento para ambas as configurações: Reversed Field Pinch e Tokamak. O primeiro é um excelente "parque de diversões" para os estudos de RMW, dado o espectro de instabilidade que se desenvolve naturalmente. Para esta ultima configuração, no entanto, a instabilidade RMW é considera como um dos marcos a ser alcançado na estrada para um reator de fusão comercial. A segunda parte do trabalho é dedicada a essa questão e trata das propriedades de estabilidade no cenário de

Tokamaks avançados com referência, em particular, ao experimento JT-60SA. Estudos para compreender a física dos RMW em plasmas com alto β, em que o perfil de rotação do fluido e as populações superaquecidas de íons proveniente das partículas neutras podem desempenhar um papel importante, foram realizados com os códigos MHD lineares MARS-F/K. Se por um lado detalhes físicos como efeitos cinéticos são acoplados para uma descrição simplificada das estruturas passiva/ativa, por outro lado, um plasma simplificado pode ser acoplado a um modelo complexo 3-D das estruturas para avaliar capacidades realistas de controle ativo de um determinado sistema. Diferentes ferramentas são usadas e descritas para o estudo da física de amortecimento dos RMW e para encontrar uma prova de princípio para o controle de *feedback* de tais instabilidades em Tokamaks avançados operando além do limite de pressão sem parede.

CONTENTS

LIST OF FIGURES

LIST OF TABLES

ACRONYMS

MHD Magneto-Hydro-Dynamic

XK External Kink

RFP Reversed Field Pinch

RFX-mod Reversed Field eXperiment

RWM Resistive Wall Mode

RP-RWM Resistive-Plasma-RWM

MARS MAgnetohydrodynamic Resistive Spectrum

EPs Energetic Particles

NBI Neutral Beam Injector

ITER International Thermonuclear Experimental Reactor

JT-60SA Japan Torus Super Advanced

SP Stabilizing Plate

DEMO DEMOnstration Power Station

MIMO Multiple-Input-Multiple-Output

PID Proportional-Integral-Derivative

THD Total Harmonic Distortion

AT Advanced Tokamak

ITB Internal Transport Barrier

CMC Clean-Mode-Control

N-NBI Negative Neutral Beam Injector

P-NBI Positive Neutral Beam Injector

ECRF Electron Cyclotron Radio-Frequency

ECCD Electron Cyclotron Current Drive

NTM Neoclassical Tearing Mode

Part I

INTRODUCTION

1

THERMONUCLEAR FUSION AND PLASMA CONFINEMENT

"Unless you can make the world wag better than it does at present, King, your reign will be an endless series of petty battles."

— T.H. White, The Once and Future King

Standards of living and quality of life in our civilization are known to be directly related to energy consumption, indicators of human development are often determined by the per capita consumption of electricity. Industrialized and developing countries have ever-growing energy requirements to sustain food production, industrial facilities, transport and communication. This energy must be produced with a reasonable efficiency and a convenient price. The world's main energy resource in the last centuries has been primary fossil fuels such as coal, oil and natural gases that are nowadays showing availability problems. Furthermore the usage of these sources has caused severe issues in terms of greenhouse gases production, with documented negative effects on the environment. The most notorious of these effects is surely global warming and climate issues in general, which require massive reduction of greenhouse gases production in the future, up to 80% in the next decades. The price to pay for a *greener* energy is to gradually cease exploitation of the already depleted oil reserves while not increasing the usage of largely available yet extremely polluting coal veins.

Conventional fission nuclear power has been vastly deployed and developed over the last few decades, representing a viable alternative to fossil fuels and allowing the rise of today's world powers. This technology could possibly provide energy for thousands of years once elements such as ^{239}Pu and ^{233}U are considered beyond the standard ^{235}U. Public opinion however has not been kind with fission technology for many reasons: the atomic fear of Cold War era has resulted in proliferation concerns, storing for centuries dangerous and slowly decaying radioactive wastes is a non-negligible and unsolved issue, catastrophic scenarios such as Chernobyl or the more

recent case of Fukushima have mined further development of traditional nuclear energy in many countries.

Alternative energy sources that meet the requests of renewability and environmental sustainability are being researched and increasingly deployed for electricity production. Solar and wind energy could be viable alternatives to fossil fuels in the near term but still lack the efficiency and cost of production requirements to represent long term investments. Solar energy is maybe the most important renewable resource and it is widely used in industrialized countries both in photo-voltaic and thermal technologies. Today's commercial solar panels however have very low efficiencies, around $12 - 18\%$, and although great effort is being put into improving this aspect there are other reasons suggesting that solar power will still play a supportive role for many years: the lack of high energy density required to operate large facilities and the high initial investment and maintenance costs. Other minor resources such as hydroelectricity play an important role in specific geographical areas and Italy relies on hydroelectric power for about 18% of its national electricity production. While it is clearly incapable of sustaining massive urban and industrial complexes, hydroelectric energy could be a good solution to meet the request in peak hours and play a supportive role.

In this complex background fusion power could play an important role in providing a sustainable, solid and long term energy source [1]. Nature itself seems to have chosen fusion to power stars: in these immense spatial objects fusion reactions produce the energy that has allowed for life on Earth to develop. The environment in which fusion occurs in nature however, is hardly comparable to that on Earth; the laws of physics governing fuel confinement, thus creating the conditions for the reaction to take place, are radically different. Hypothetical human-scale fusion plants could help reducing global warming without many of the potential biological hazard of today's fission technology. If the CO_2 emission of a fusion reactor is somehow comparable to that of a traditional fission plant, the potential danger coming from long living radioactive waste and operational safety is greatly reduced. Of course risk reduction does not mean complete safety, a fusion reactor would still consume and produce radioactive material such as tritium, which is the main fuel of today's concepts, and rely on neutron acti-

vated components; proper materials must be therefore chosen and developed that would not require hundreds of years of absolute containment.

A fusion reaction takes place when two light nuclei gain enough kinetic energy to overcome the Coulomb barrier and get in the strong nuclear force range; this force is responsible for atomic nuclei being tightly bound and it drives the fusion of two nuclei when the reaction is convenient in terms of energy. The product of a fusion reaction is one or more heavier nuclei with slightly less mass that the sum of first two, this difference in mass accounts for the energy release. In tomorrow's power plants the main fuel will probably be represented by deuterium (D) and tritium (T). The former is largely present on Earth and can be extracted from natural water, the latter instead is a radioactive isotope $\beta-$unstable with a half-life of about 12.6 years. Clearly tritium must be produced and cannot be stored in long term facilities. A viable option for a reactor could be the breeding of T on-site thanks to the interaction of slowed down neutrons with a lithium mantle. Four different nuclear reactions are considered important for fusion purposes [2] [3]:

$$
\begin{aligned}
&D + T \longrightarrow {}^4He(3.5\ \ MeV) + n(14.1\ \ MeV) \\
&D + D \longrightarrow T(1.01\ \ MeV) + p(3.02\ \ MeV) \qquad 50\% \\
&D + D \longrightarrow {}^3He(0.82\ \ MeV) + n(2.45\ \ MeV) \qquad 50\% \\
&D + {}^3He \longrightarrow {}^4He(3.6\ \ MeV) + p(14.7\ \ MeV)
\end{aligned}
$$

The D-T reaction is the easiest to obtain in terms of cross-section and required temperature, this is the reason why the first generation of reactors, as well as experiments like the ITER project, will use a D-T mixture plasma confined in a toroidal chamber. If in space the enormous mass of stars balances thermal expansion with gravitational attraction, on Earth other particle and energy confinement methods are clearly required. There are currently two ways of approaching this challenge: *magnetic* confinement and *inertial* confinement. The latter will not be considered in the present work, let it suffice to say that it consists in heating to ignition temperatures solid pellets of fuel that generate net power before falling apart in micro-explosions. This thesis is set instead in the magnetic confinement framework where the primary objective is, as the name suggests, confining a hot plasma by means of external magnetic fields. Many techniques

and devices have been developed in the past century to face this challenge, some of the most promising have culminated in the International Thermonuclear Experimental Reactor (ITER): the largest magnetic confinement experimental power plant currently being built in Cadarache (France). The project is managed by an international collaboration and funded by European Union (EU), India, Japan, China, Russia, South Korea and the United States. Much effort is being put into the ITER project which would hopefully be the first reactor to achieve a positive power gain, targeting operations at $Q = \frac{P_{output}}{P_{input}} \approx 10$. The power gain criterion is obviously fundamental for a power plant to be successful, the minimum requirement being $Q > 1$. Another fundamental parameter that ought to be mentioned is the β factor. Defined as the ratio of kinetic to magnetic pressure, $\beta = \frac{p}{B^2/2\mu_0}$, it evaluates the effectiveness of plasma magnetic confinement. The achievable value of β is often limited by plasma instabilities.

High β values are desirable for robust confinement, this can be expressed by introducing the triple product $n\tau_E T$, where n is the particle density, τ_E the energy confinement time and T the temperature. This product can be used to estimate the so-called ignition condition, in which the power produced by the plasma itself (through α particles) is sufficient to balance the losses and sustain the reaction with non external heating. Among the many criteria that can be used for the ignition condition calculation, one of the first to be introduced is the Lawson criterion. Assuming that the total power leaving the plasma, including losses and fusion products, is converted to electricity with efficiency $\eta \sim 30\%$, the condition for which fusion power can heat the plasma by itself is:

$$P_b + P_L = \eta \left(P_b + P_L + P_f\right) \tag{1}$$

where P_b represents radiation losses (mainly *bremsstrahlung*), P_L the transport losses and P_f the power produced by fusion reactions. This condition can be translated into:

$$n\tau_E > \frac{12T}{\frac{\eta}{1-\eta}\langle\sigma v\rangle E_f - 4\alpha_b T^{1/2}} \tag{2}$$

where $\langle\sigma v\rangle = \langle\sigma v\rangle(T)$ is the reactivity, E_f the energy produced by a single fusion reaction (17.6 MeV for D-T) and $\alpha_b = 5.35 \times 10^{-37} W m^3 keV^{-1/2}$ is a constant related to radiation losses.

In the present thesis a series of studies on stability and control of Magnetohydrodynamic instabilities is shown. The first part gives a general introduction to the main topics of the work. Starting with MHD theory, a short review of the studies carried out on instabilities such as the Resistive Wall Mode, with their relevance for high β operation, is given in Chapter 2. The MARS-F/K codes are described in Chapter 3 while Chapter 4 gives a useful introduction on control theory. This part of the manuscript is closed by Chapter 5, which describes the main experimental devices on which the work has been carried out. The second part of the thesis includes studies on the optimization of the RFX-mod control system. With the main focus being active control of Resistive Wall Modes, the task of actuator-sensor decoupling is tackled with a lightweight, real-time applicable strategy, as described in Chapter 6. The same concept is used to take into account the faulting or shutting down of sparse actuators. Chapter 7 describes how a matrix-based compensation method can help in reducing the harmonic distortion of the magnetic field produced by a non-uniform coil array. A study on the effects of missing coil compensation on first wall heating is also presented. The part concerning RFX-mod is closed by Chapter 8, with a numerical study aiming at assessing the multi-modal control capabilities of reduced arrays of active coils. The third and final part of the thesis is focused on Resistive Wall Modes characterization and control in JT-60SA Advanced Tokamak, high β, fully non-inductive scenarios. The characterization of Resistive Wall Mode physics, damping mechanisms, effect of fluid rotation and kinetic particles, has been carried out with the MARS-F/K codes and is shown in Chapter 9. An important result is then shown in the final Chapter 10, with a numerical study on feedback control of the n=1 Resistive Wall Mode on JT-60SA.

2

INTRODUCTION TO EQUILIBRIUM AND STABILITY

"Books only change the world
if the world is capable of digesting them."

— Luther Blissett, Q

A fusion relevant plasma is a hot fully ionized gas whose behavior is dominated by long range electric and magnetic forces that make this plasma a very good conductor. The microscopic reason for good plasma conductivity lies in high temperature and low density that cause long range Coulomb interactions, and thus resistance, to be very weak. A practical consequence of conductivity is the shielding from electric fields whereas magnetic fields penetrate making plasma confinement possible. Thermonuclear fusion plasmas have typical densities and temperatures of respective order $n \sim 10^{20}\ m^{-3}$ and $T \lesssim 10\ keV$. Describing a plasma with a microscopic single particle approach would be a tremendous task in terms of math or computational requirements. Fluid models on the other hand present less of a challenge and either two-fluid or single-fluid equations can provide self consistent models that allow an accurate analysis of major issues in plasma physics such as equilibrium and stability. This Chapter deals with the Magneto-Hydro-Dynamic (MHD) single-fluid model and specifically with its application to fusion relevant plasmas confined by means of magnetic fields. This model can be derived both from the two-fluid model and from single particle guiding center theory, this is not reported here and can be found [4]. A complete derivation of the model from fundamental assumptions on the fluid an scales of interest is given in [5], which will be followed for part of this introduction. In Section 2.1 the MHD model is introduced, the toroidal equilibrium description is given in Section 2.2 with the Grad-Shafranov equation and introduction of the useful flux functions. The linearized MHD equations are given in Section 2.3, along with the plasma displacement definition and discussion of the ideal force operator as a foreword to stability. The ideal MHD energy principle is outlined in Section 2.4. A brief discussion on the ideal kink instability is presented in Section

2.5, while a description of the Tokamak and RFP configurations closes the Chapter with Sections 2.6 and 2.7 respectively.

2.1 MHD PLASMA DESCRIPTION

In MHD description the plasma is considered as a single conducting fluid, thus coupling fluid-dynamics with the Maxwell equations. With physical quantities being averaged over physically infinitesimal volumes, an ordering of length scales is assumed:

$$\lambda \sim a_0 << \delta < L \tag{3}$$

where λ is the mean free path in atomic collisions, a_0 the atomic radius, δ the distance which is considered *physically infinitesimal* and L is the smallest relevant macroscopic distance to be considered. This also implies an ordering or frequencies (i. e.time scales) which concentrates on low-frequency phenomena, therefore $V^2/c^2 << 1$ where V is the characteristic fluid velocity and c the speed of light. The single-fluid equations of the MHD model can be written, in the Eulerian frame, as:

MHD Model

$$\frac{\partial \rho}{\partial t} + \nabla \cdot \rho \mathbf{V} = 0 \tag{4}$$

$$\rho \left(\frac{\partial \mathbf{V}}{\partial t} + \mathbf{V} \cdot \nabla \mathbf{V} \right) = -\nabla p + \frac{1}{\mu_0} (\nabla \times \mathbf{B}) \times \mathbf{B} + \nabla \cdot \mathbf{\Pi} \tag{5}$$

$$\frac{\partial \rho}{\partial t} + \mathbf{V} \cdot \nabla p = -\Gamma p \nabla \cdot \mathbf{V} + (\Gamma - 1) \left[-\nabla \cdot \mathbf{q} + \mathbf{\Pi} \cdot \nabla \mathbf{V} + \eta J^2 \right] \tag{6}$$

$$\frac{\partial \mathbf{B}}{\partial t} = \nabla \times \left(\mathbf{V} \times \mathbf{B} - \frac{\eta}{\mu_0} \nabla \times \mathbf{B} \right) \tag{7}$$

$$\nabla \cdot \mathbf{B} = 0 \tag{8}$$

Where ρ is the mass density, p the scalar pressure, $\mathbf{B}$ the magnetic field, Γ the adiabatic index, $\mathbf{\Pi}$ the stress tensor, $\mathbf{q}$ the heat flux and η the plasma resistivity. Specification of the last three unknowns are required in order to close the system. For the work that will be presented in the following chapters the system can be simplified to the so-called ideal case, in which $\mathbf{q}$, $\mathbf{\Pi}$ and η are neglected. The described plasma is therefore considered a perfect electrical conductor with no viscosity of thermal conductivity. This is of course not true for a real plasma, such a model can nevertheless give a good approximation of some properties of hot and highly magnetized plasmas, as will be-

come clear throughout this introduction. Under the aforementioned conditions, the above equations can be reduced to:

Ideal MHD Model

$$\frac{\partial \rho}{\partial t} + \nabla \cdot \rho \mathbf{V} = 0 \tag{9}$$

$$\rho \left(\frac{\partial \mathbf{V}}{\partial t} + \mathbf{V} \cdot \nabla \mathbf{V} \right) = -\nabla p + \frac{1}{\mu_0} (\nabla \times \mathbf{B}) \times \mathbf{B} \tag{10}$$

$$\frac{\partial \rho}{\partial t} = -\mathbf{V} \cdot \nabla p - \Gamma p \nabla \cdot \mathbf{V} \tag{11}$$

$$\frac{\partial \mathbf{B}}{\partial t} = \nabla \times (\mathbf{V} \times \mathbf{B}) \tag{12}$$

$$\nabla \cdot \mathbf{B} = 0 \tag{13}$$

2.2 TOROIDAL EQUILIBRIUM

Magnetic field lines in toroidal axisymmetric configurations lie on nested toroidal surfaces, these can be found as level surfaces of the solutions of the Grad-Shafranov equation [6]. Consider a cylindrical coordinate system (R, z, ϕ) where $R = 0$ gives the major axis of the torus and ϕ is the toroidal direction. The magnetic field can thus be written as:

$$\mathbf{B} = B_\phi \hat{e}_\phi + \mathbf{B}_p$$

where $\mathbf{B}_p$ is the field on the poloidal $(R - z)$ plane. The components of the poloidal field can be used to define the *poloidal flux function* $\psi(R, z)$:

$$\begin{cases} B_R = -\frac{1}{R} \frac{\partial \psi}{\partial z} \\ B_z = \frac{1}{R} \frac{\partial \psi}{\partial R} \end{cases} \qquad \Longrightarrow \quad \mathbf{B}_p = \frac{1}{R} \left(\nabla \psi \times \hat{e}_\phi \right)$$

This function is the flux of the magnetic field through the surface enclosed between the magnetic axis and a generic magnetic surface. ψ is found to be constant along the magnetic field lines:

$$\mathbf{B} \cdot \nabla \psi = 0 \tag{14}$$

The very same procedure can be applied to the current density to obtain a *current flux function*:

$$\begin{cases} J_R = -\frac{1}{R} \frac{\partial f}{\partial z} \\ J_z = \frac{1}{R} \frac{\partial f}{\partial R} \end{cases}$$

at the same time Ampère's law in its stationary form gives:

$$\nabla \times \mathbf{B} = \mu_0 \mathbf{J} \implies \begin{cases} J_R = -\frac{1}{\mu_0}\frac{\partial B_\phi}{\partial z} \\ J_z = \frac{1}{\mu_0}\frac{1}{R}\frac{\partial (RB_\phi)}{\partial R} \end{cases} \implies f = \frac{RB_\phi}{\mu_0}$$

The $f(R, z)$ plays the same role as ψ and again is constant along the current lines:

$$\mathbf{J} \cdot \nabla f = 0 \tag{15}$$

From the force balance Eq. 10 we can see that both $\mathbf{B}$ and $\mathbf{J}$ are orthogonal with respect to the pressure gradient, that is to say: the pressure is constant both on the magnetic surfaces and along the current lines. The force balance can be expressed in the previously introduced notation:

$$\begin{aligned} \nabla p &= \mathbf{J}_p \times \hat{e}_\phi B_\phi + \hat{e}_\phi J_\phi \times \mathbf{B}_p \\ &= \frac{1}{R}\left(\nabla f \times \hat{e}_\phi\right) \times \hat{e}_\phi B_\phi + \hat{e}_\phi J_\phi \times \frac{1}{R}\left(\nabla \psi \times \hat{e}_\phi\right) \\ &= -\frac{B_\phi}{R}\nabla f + \frac{J_\phi}{R}\nabla \psi \end{aligned}$$

Writing p and f as functions of the poloidal flux:

$$\nabla f(\psi) = \frac{df}{d\psi}\nabla \psi \tag{16}$$

$$\nabla p(\psi) = \frac{dp}{d\psi}\nabla \psi \tag{17}$$

the following expression for the toroidal component of the current is obtained:

$$\begin{aligned} J_\phi &= R\frac{dp}{d\psi} + B_\phi \frac{df}{d\psi} \\ &= R\frac{dp}{d\psi} + \frac{\mu_0}{R} f \frac{df}{d\psi} \end{aligned}$$

Grad-Shafranov Equation

The Grad-Shafranov equation is finally obtained comparing the previous result with the toroidal component of the Ampère law:

$$\begin{aligned} \mu_0 J_\phi &= \frac{dB_R}{dz} - \frac{dB_z}{dR} \\ &= -\frac{1}{R}\frac{\partial^2 \psi}{\partial z^2} - \frac{\partial}{\partial R}\left(\frac{1}{R}\frac{\partial \psi}{\partial R}\right) \end{aligned}$$

$$R\frac{\partial}{\partial R}\left(\frac{1}{R}\frac{\partial \psi}{\partial R}\right) + \frac{\partial^2 \psi}{\partial z^2} = -\mu_0 R^2 p'(\psi) - \mu_0^2 f(\psi) f'(\psi) \tag{18}$$

2.3 LINEARIZATION FOR SMALL DISPLACEMENTS

Applying a linear perturbation to an otherwise stable equilibrium simplifies the stability problem reducing its equations to the form of an eigenvalue problem, with the eigenvalue being the growth rate of the perturbation. The idea is to slightly perturb the plasma from its equilibrium state, examining the time dependence of the small amplitude perturbation. The procedure starts by splitting the problem into an equilibrium and a stability part, i. e.expanding all dependent variables as the sum of an equilibrium solution plus the perturbation. Assuming that the quantities of interest can be linearized about their equilibrium values:

$$A(\mathbf{r}, t) = A_0(\mathbf{r}) + \tilde{A}_1(\mathbf{r}, t)$$

where $\frac{\tilde{A}_1}{|A_0|} \ll 1$ is a small first order perturbation, which takes the general form:

$$\tilde{A}_1(\mathbf{r}, t) = A_1(\mathbf{r})\, e^{-\imath\omega t} \tag{19}$$

The simplest definition of stability could be the following: if any of the system's eigenfunctions ω corresponds to exponential growth (i.e. $\Im(\omega) > 0$) the system is said to be exponentially unstable. In the given definition the assumption that modes are discrete with distinguishable frequencies is implicit. With the assumption of a stationary plasma (i. e.$\mathbf{V}_0 = 0$) and by dropping all non-linear terms, the linearized MHD system can be written as follows:

Linearized MHD Model

$$\frac{\partial \rho_1}{\partial t} = -\nabla \cdot \rho_0 \mathbf{V}_1 \tag{20}$$

$$\rho_0 \frac{\partial \mathbf{V}_1}{\partial t} = -\nabla p_1 + \mathbf{J}_0 \times \mathbf{B}_1 + \mathbf{J}_1 + \mathbf{B}_0 \tag{21}$$

$$\frac{\partial p_1}{\partial t} = -\mathbf{V}_1 \cdot \nabla p_0 - \Gamma p_0 \nabla \cdot \mathbf{V}_1 \tag{22}$$

$$\frac{\partial \mathbf{B}_1}{\partial t} = \nabla \times (\mathbf{V}_1 \times \mathbf{B}_0) \tag{23}$$

$$\nabla \times \mathbf{B}_0 = \mu_0 \mathbf{J}_1 \tag{24}$$

$$\nabla \cdot \mathbf{B}_1 = 0 \tag{25}$$

As a first step to simplify these equations we can extract the time dependence by means of a normal mode expansion, i.e. rewriting all the perturbed observables as:

$$\tilde{A}_1(\mathbf{r}, t) = A_1(\mathbf{r})\, e^{-\imath\omega t}$$

In the above equation ω is a complex frequency. A possible approach to stability involves the study of its imaginary part, if $\Im\omega > 0$ the perturbation grows exponentially and the system is therefore unstable. If on the other hand $\Im\omega < 0$ the perturbation is either exponentially damped of oscillates about an equilibrium position. The problem can be further simplified by introducing the so-called *plasma displacement* $\boldsymbol{\xi}(\mathbf{r}, t)$:

Plasma Displacement

$$\mathbf{V}_1 \equiv \frac{\partial \boldsymbol{\xi}}{\partial t} = -\imath\omega\boldsymbol{\xi}(\mathbf{r})\, e^{-\imath\omega t} \tag{26}$$

The previous linearized equations can now be written in terms of this new quantity:

$$\begin{aligned}
\rho_1 &= -\boldsymbol{\xi}\cdot\nabla\rho_0 - \rho_0\nabla\cdot\boldsymbol{\xi} \\
p_1 &= -\boldsymbol{\xi}\nabla p_0 + \Gamma p_0\nabla\boldsymbol{\xi} \\
\mathbf{Q} \equiv \mathbf{B}_1 &= \nabla\times(\boldsymbol{\xi}\times\mathbf{B}_0) \\
\mathbf{J}_1 &= \frac{1}{\mu_0}\nabla\times[\nabla\times(\boldsymbol{\xi}\times\mathbf{B}_0)]
\end{aligned} \tag{27}$$

Where the time dependent factors $e^{-\imath\omega t}$ cancel out in every term. There is one last equation remaining: the momentum conservation represented by Eq. 21. Using 27 into 21 we obtain:

Ideal MHD Force Operator

$$\begin{aligned}
\rho_0\frac{\partial^2\boldsymbol{\xi}}{\partial t^2} &= \frac{1}{\mu_0}(\nabla\times\mathbf{B}_0) + \frac{1}{\mu_0}\nabla\times[\nabla\times(\boldsymbol{\xi}\times\mathbf{B}_0)] + \\
&+ \frac{1}{\mu_0}\nabla\times[\nabla\times(\boldsymbol{\xi}\times\mathbf{B}_0)]\times\mathbf{B}_0 + \nabla\cdot(\boldsymbol{\xi}\cdot\nabla p_0 + \Gamma p_0\nabla\boldsymbol{\xi}) \\
&= \frac{1}{\mu_0}(\nabla\times\mathbf{B}_0)\times[\nabla\times(\boldsymbol{\xi}\times\mathbf{B}_0)] + \frac{1}{\mu_0}\nabla\times[\nabla\times(\boldsymbol{\xi}\times\mathbf{B}_0)]\times\mathbf{B}_0 + \\
&\quad + \nabla(\boldsymbol{\xi}\nabla p_0 + \Gamma p_0\nabla\boldsymbol{\xi}) \\
&\equiv \mathbf{F}(\boldsymbol{\xi})
\end{aligned} \tag{28}$$

Eq. 28 is to be solved as an eigenvalue problem where $\mathbf{F}$ is called *force operator* and has the property of being self-adjoint. This property, proof of which be found in [7], has important consequences such as the existence of an energy principle. Continuing the analysis of the small displacements problem, or normal modes approach, we suppose the desired solutions take the form:

$$\boldsymbol{\xi}_n(\mathbf{r}, t) = \boldsymbol{\xi}_n(\mathbf{r})\, e^{-\imath\omega_n t}$$

Ideal MHD Wave Equation

then Eq. 28 can be written as:

$$\mathbf{F}(\xi_n) = -\omega_n^2 \rho_0 \xi_n \tag{29}$$

This has clearly the form of an eigenvalue problem where the eigenfunctions are ξ_n and ω_n^2 the corresponding eigenvalues. Given the self-adjointness of the force operator $\mathbf{F}$ we can show that ω_n^2 are forced to be real; for a generic eigenfunction ξ_n and its complex conjugate ξ_n^*:

$$\int \xi_n^* \cdot \mathbf{F}(\xi_n)\, dV = \int \xi_n \cdot \mathbf{F}(\xi_n^*)\, dV$$

This property can be used in Eq. 29 once integrated over volume multiplying both members by ξ_n^*:

$$\begin{aligned}\omega_n^2 \rho_0 \int \xi_n^* \cdot \xi_n dV = \\ &= -\int \xi_n^* \cdot \mathbf{F}(\xi_n)\, d\tau = \\ &= -\frac{1}{2}\int \xi_n^* \cdot \mathbf{F}(\xi_n)\, dV - \frac{1}{2}\int \xi_n \cdot \mathbf{F}(\xi_n^*)\, dV\end{aligned}$$

Therefore for the generic n^{th} eigenvalue we can write:

$$\begin{aligned}\omega_n^2 &= -\frac{1}{2\rho_0}\frac{\int \xi_n^* \cdot \mathbf{F}(\xi_n)\, dV + \int \xi_n \cdot \mathbf{F}(\xi_n^*)\, dV}{\int \xi_n \cdot \xi_n^* dV} = \\ &= -\frac{1}{\rho_0}\frac{\Re\left[\int \xi_n \cdot \mathbf{F}(\xi_n^*)\, dV\right]}{\int \xi_n^2 dV}\end{aligned} \tag{30}$$

which is a real quantity. Therefore, due to the self-adjointness of the force operator, its eigenvalues are real and the ideal MHD normal modes are either purely oscillating or purely growing/-damped.

2.4 IDEAL MHD ENERGY PRINCIPLE

The discussion on the force operator outlined in the previous sections suggested that, because of the self-adjointness property, the stability of a system could be assessed by using a variational approach. An energy variational principle allows to do so without solving the plasma displacement equation (Eq. 28). The task of solving a stability problem requires writing an expression for plasma potential energy and minimizing it using plasma displacements $\xi(\mathbf{r}, t)$ as test functions. It can be shown that the plasma potential energy can be written as a functional of displacement vectors. By recalling the definition of plasma

displacement, Eq. 26, we define the total kinetic energy of the system as:

$$K = \frac{1}{2}\int \rho_0 \dot{\xi}^2 dV$$

To find the potential energy we should examine how the kinetic energy varies with time, remembering as well the self-adjointness of $\mathbf{F}$, its linearity and the fact that the derivative of plasma displacement $\frac{\partial \xi}{\partial t}$ is also a solution to Eq. 29:

$$\begin{aligned}
\frac{dK}{dt} &= \frac{1}{2}\int \rho_0 \frac{\partial}{\partial t}\left(\dot{\xi}^2\right) dV = \int \frac{\partial \xi}{\partial t}\cdot\frac{\partial^2 \xi}{\partial t^2} dV = \int \frac{\partial \xi}{\partial t}\cdot \mathbf{F}(\xi)\, dV \\
&= \int \xi \cdot \mathbf{F}\left(\frac{\partial \xi}{\partial t}\right) dV \\
&= \frac{1}{2}\int \frac{\partial \xi}{\partial t}\cdot \mathbf{F}(\xi)\, dV + \frac{1}{2}\int \xi \cdot \mathbf{F}\left(\frac{\partial \xi}{\partial t}\right) dV \\
&= \frac{1}{2}\int \frac{\partial \xi}{\partial t}\cdot \mathbf{F}(\xi)\, dV + \frac{1}{2}\int \xi \cdot \frac{\partial}{\partial t}\mathbf{F}(\xi)\, dV \\
&= \frac{1}{2}\int \frac{\partial}{\partial t}\left[\xi \cdot \mathbf{F}(\xi)\right] dV = \frac{d}{dt}\left[\frac{1}{2}\int \xi \cdot \mathbf{F}(\xi)\, dV\right]
\end{aligned}$$

From this latter expression we see that the time variation of the total kinetic energy can be written as:

$$\frac{d}{dt}\left[K - \frac{1}{2}\int \xi \cdot \mathbf{F}(\xi)\, dV\right] = \frac{d}{dt}(K + \delta W) = 0 \tag{31}$$

this represents the total energy conservation and defines the variation of the system potential energy with respect to equilibrium as:

$$\delta W = -\frac{1}{2}\int \xi \cdot \mathbf{F}(\xi)\, dV \tag{32}$$

Calculating this energy variation allows to distinguish between stable and unstable equilibra. If $\delta W > 0$ then every plasma displacement ξ_n causes potential energy to increase and the tested equilibrium is therefore stable because corresponding to a minimum of potential energy. Recalling the eigenvalue problem introduced in the previous Section (Eq.29) and the discussion on the eigenvalues ω_n^2 being real, we can rewrite the potential energy variation:

$$\delta W = -\frac{1}{2}\int \xi_n \cdot \mathbf{F}(\xi_n)\, dV = \frac{1}{2}\omega_n^2 \int \rho_0 \xi_n^2 dV$$

The eigenvalues then take the following form:

$$\omega_n^2 = \frac{\delta W}{\frac{1}{2}\int \rho_0 \xi_n^2 \, dV}$$

From this last expression it appears clearly that the $\delta W > 0$ condition corresponds to a stable mode because $\omega_n^2 > 0$ implies $\omega_n \in \mathbb{R}$. On the other hand the opposite situation $\delta W < 0$ leads to instability because $\omega_n^2 < 0$ implies a purely imaginary eigenvalue ω_n that causes exponential growth of the corresponding plasma displacement mode.

In order to apply the energy principle to specific problems, it has to be extended to include contributions from vacuum regions and plasma/vacuum boundaries. The total potential energy of the perturbed system can then be written as [4]:

$$\delta W = \delta W_F + \delta W_S + \delta W_V \tag{33}$$

with the three components being *fluid*, *surface* of the plasma/-vacuum interface and *vacuum* respectively. These can be expressed as follows:

$$\delta W_F = \frac{1}{2}\int_{V_F} dV \left[\frac{|\mathbf{Q}|^2}{\mu_0} - \xi_\perp^* \cdot (\mathbf{J}\times\mathbf{Q}) + \Gamma p_0 |\nabla\cdot\xi|^2 + (\xi_\perp\cdot\nabla p_0)\,\nabla\cdot\xi_\perp^*\right] \tag{34}$$

$$\delta W_S = \frac{1}{2}\int_S dS |\hat{\mathbf{n}}\cdot\xi_\perp|^2 \hat{\mathbf{n}}\cdot\nabla\left[\!\!\left[p + \frac{B^2}{2\mu_0}\right]\!\!\right] \tag{35}$$

$$\delta W_V = \frac{1}{2}\int_V dV \frac{1}{\mu_0}\left|\nabla\times\hat{\mathbf{A}}\right|^2 \tag{36}$$

2.5 EXTERNAL KINK INSTABILITY AND RESISTIVE WALL MODES

Extensive stability analysis of ideal MHD plasmas has allowed for the identification of the External Kink (XK) instability as one of the major obstacles to the increasing of pressure in fusion experiments. This has been expressed in terms of the β_N parameter since the discovery of the Troyon scaling law [8]. *External Kink*

$$\beta_N = \%\beta \frac{a B_\phi}{I_p} \tag{37}$$

where a is the plasma minor radius, B_ϕ the toroidal magnetic field and I_p the plasma current in MA. According to this scaling the maximum achievable β_N was predicted to be constant for

all Tokamaks. With no external wall surrounding the plasma. In these conditions the growth rate of such instabilities is on the Alfvén time scale ($\tau_A = R/(B_\phi/\sqrt{\mu_0\rho})$, with ρ being the plasma density and R the major radius). This makes the XK mode particularly dangerous, causing disruptions and limiting the thermonuclear power of an eventual plant. Studies on the effect of a resistive wall surrounding the plasma have been carried out [9], proving that XKs cannot be stabilized by introducing walls with finite electrical conductivity, while at the same time it is not possible to enclose a reactor-relevant plasma in a superconducting first wall. Nevertheless the resistivity of the wall material reduces the growth rate of the XK to the time scale of the magnetic perturbation penetration time in the wall itself ($1/\tau_W$). The resultant instability is called Resistive Wall Mode (RWM) and it can be considered a new declination of the XK. To summarize the information on XKs stability, we can say that with no external wall (i. e.$\tau_W = 0$) the plasma is unstable for $\beta_N > \beta_N^{no-wall}$. If an ideal wall is present instead (i. e.$\tau_W = \infty$), the plasma is stable up to the so-called ideal-wall limit. When a finite wall resistivity is introduced, the RWM branch appears, leading to a slower instability growing on wall time scales in the range $\beta_N^{no-wall} < \beta_N < \beta_N^{id-wall}$. According to present understanding three factors are of key importance for determining these stability limits: the current profile (i. e.the plasma internal inductance), the pressure profile (i. e.the pressure peaking factor) and the minimum value of the safety factor profile (i. e.q_{min}).

Resistive Wall Mode

No-Wall Limit

Ideal-Wall Limit

2.5.1 *Rotation Stabilization and Kinetic Effects*

A first response to the challenge of understanding RWMs and going towards stabilization has been given Bondeson and Ward in [10], proposing that low toroidal number modes could be fully stabilized by resistive walls in a plasma rotating at a fraction of the Alfvén speed. In this model plasma dissipation occurs through ion Landau damping, transferring momentum from the plasma to the RWM which would be rotating with respect to the wall, thus leading to stabilization. A critical rotation value is found above which a stability window opens from low β_N up to the ideal-wall limit. This critical rotation is found to be only a few per cent of the Alfvén velocity, such values are easily reached in present day Tokamaks relying on Neutral Beam Injector (NBI) heating and current drive. Both numerical and experimental studies have been carried out for the verification

and investigation of RWM rotational stabilization [11]. From the theoretical point of view it is worth mentioning introduction of the kinetic approach by Hu and Betti [12], with the inclusion of the potential energy δW_k in the dispersion relation:

RWM Kinetic Dispersion Relation

$$\gamma \tau_W = -\frac{\delta W_\infty + \delta W_k}{\delta W_b + \delta W_k} \tag{38}$$

where δW_∞ is the no-wall fluid potential energy, while δW_b is the potential energy with an ideal wall at radius b. The kinetic contribution can either be calculated using the fluid RWM eigenfunction or from a complete eigenfunction with the self-consistent inclusion of diamagnetic and magnetic drifts. This latter is the so-called self-consistent drift-kinetic approach introduced by the MARS-K code which will be described in Chapter 3. The MARS code has been extensively used to study the critical rotation and damping mechanisms for RWMs. In the first years of experimental activities on RWMs studies have been carried out on JT-60 to assess mode characteristics in rotating plasmas [13] and the growth rate dependence on plasma-wall relative position [14]. The important relationship between RWMs and disruptions has been studied on DIII-D [15] [16], with the observation that the onset of the mode caused a plasma β collapse. Further experiments on JT-60U [17] and DIII-D [18] have achieved lower stabilization thresholds with respect to previous results with plasma rotation. Values lower that 0.3% of the Alfvén speed have been achieved by reducing neutral beam torque and magnetic braking. The role of plasma resistivity on RWM stability has also been investigated as one possible damping channel. The possibility of stabilizing RWMs with very small plasma rotation has been introduced [19] for the case in which a resistive plasma is considered. Further studies have confirmed the stabilizing role of resistivity [20] [21] for the so-called Resistive-Plasma-RWM (RP-RWM). The topic however is still under investigation, recent theoretical work has applied an energy principle [22] to modes interacting with resistive wall in a plasma with a resistive layer [23], finding a destabilizing contribution to be introduced by resistivity. To conclude this short review we can say RWM stabilization is one of the crucial tasks for future fusion devices, particularly when aiming at steady state operation and high plasma pressure. For this reason the problem of understanding the physical mechanisms lying underneath these modes, including the possible damping channels, has been challenged in theory and experiments [8][24][11][25][26]. Dealing with Resistive Wall Modes, which

although slowed down by passive structures are still strong ideal instabilities, can be a complex task and has been done in different ways, mainly using passive and active techniques. Passive stabilization is usually sought with a combination of plasma flow and different damping mechanisms such as viscosity or the so-called kinetic resonance with particle drift motions. Plasma rotation has been theoretically found to have a stabilizing effect on the RWM in Tokamak plasmas [27][10][28] and many studies are being carried out on the interaction with particle drift motions [29][30][31]. The effect of precession drift resonance for trapped particles has been seen important in particular [32][12][33].

2.5.2 *Feedback Stabilization*

According to the discussion so far, it is well known that an external resistive wall can provide transient stabilization for ideal MHD modes by reducing instability growth rates. On time scales longer than the wall penetration time though, the residual instability known as RWM is observed. In Reversed Field Pinch (RFP) as well as in Tokamak devices RWM stabilization is crucial for fusion research, with the sophisticated control systems above mentioned plasma stabilization by feedback control studies are being conducted [34] [35] [36][37]. An early systematic study of RFP stabilization by feedback was accomplished in 1989 by Bishop [38]. The idea was to cover the toroidal pinch with a grid of both coils and magnetic sensors. This is the so-called intelligent shell concept and the desired effect would be to freeze the total normal flux through each cell of the mesh. A schematic picture from the original article is reported in Figure 1. More recent research has challenged the aliasing problem in-

Virtual Shell

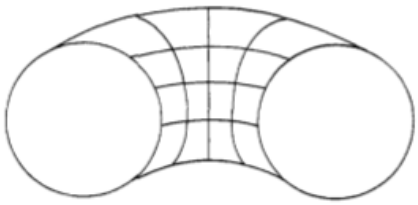

Figure 1: Section of a toroidal pinch showing the intelligent shell mesh [38].

troduced by the discrete nature of both the active coils and sensors in an intelligent shell. On RFX-mod, a particular algorithm

has been developed, the so-called Clean-Mode-Control (CMC) [39] which applies real-time correction of the systematic error affecting the measurements due to the aliasing of the sideband harmonics produced by the discrete saddle sensors. With this algorithm, and with a flexible feedback system that will be described in Section 5.1, both the RWM and tearing modes can be simultaneously controlled [35][34]. In Tokamaks, when operation beyond the no-wall pressure limit is desired and plasma rotation does not provide enough damping, the plasma must be stabilized with magnetic feedback. A large choice of feedback schemes, magnetic signals to be used and active coils configurations is available for the purpose. The advantage of using poloidal sensor signals over radial for feedback has been studied [40] and the usage of a combination of the two has been found preferable by Pustovitov [41]. It is foreseeable that future control techniques for fusion devices will take advantage of both passive and active stabilizing effects, in order to improve plasma performance.

Clean-Mode-Control

2.6 TOKAMAK

The word Tokamak stands for *TOroidalnaya KAmera* and *MAgnitnaya Katushka*, Russian expressions for *toroidal chamber* and *magnetic coil* respectively. Invented in the Soviet Union during the 1950s, its basic component is a toroidal chamber surrounded by coils that produce a toroidal magnetic field. In order to achieve an equilibrium configuration a poloidal field is also needed and in Tokamak devices this latter is produced by a current flowing through the plasma in longitudinal direction. This combination of toroidal and poloidal field produces field lines helically winding about the torus (Figure 2a). These field lines lie on the so-called magnetic surfaces (Figure 2b), the contours of constant pressure, that are found to be nested toroidal surfaces. Tokamak devices are characterized by a toroidal field intensity many times greater than the poloidal field. A time varying current flows in magnetizing windings, along the toroidal direction, giving rise to a variation of the magnetic flux and consequently to the plasma current. A schematic representation of a Tokamak device is given in Figure 3 [42]. The toroidal discharge chamber is mounted on an iron core, this acts as a transformer and is used to induce the toroidal current. A third set of coils is used in Tokamaks to control plasma shape and position, the current in these

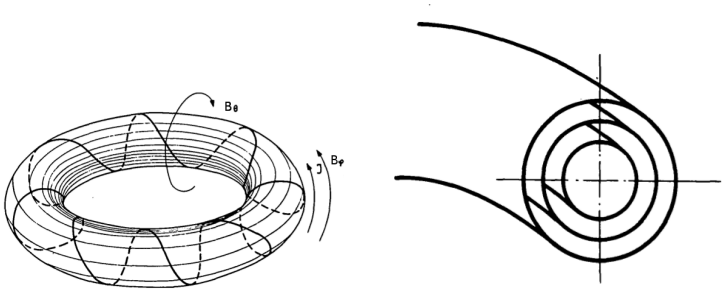

(a) (b)

Figure 2: (a) Representation of the helical magnetic field lines, (b) Nested magnetic surfaces [42].

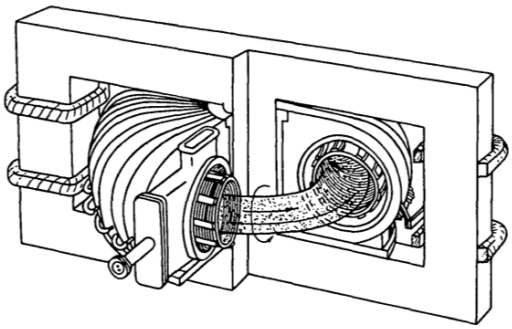

Figure 3: Schematic representation showing the main components of a Tokamak device .

coils flows parallel to the plasma current. The discharge chambers where originally composed of two main casings: a stainless steel inner vessel and a copper outer one. Contact between plasma and inner wall was reduced with the use of limiters [42] while in modern experiments the divertor technology is preferred [3]. In modern Tokamaks a non-circular poloidal section has also been adopted, the elongated *D-shaped* section allows higher current and pressure values for a given magnetic field. This shape of the magnetic surfaces is obtained as one of the possible solutions of the Grad-Shafranov equation, discussed in Sec. 2.2. Kink modes are the strongest ideal MHD instabilities and appear both as pressure driven and current driven in Tokamaks. In the perfectly conducting plasma current model all kink modes are stable if the safety factor $q(r)$ is monotonic and $q(a) \geqslant 1$ [6]. According to more realistic models Tokamak plasmas are considered to be safely stable when $q(a) > 2$ [3], in order to avoid the development of sawtooth instabilities.

The Tokamak configuration has achieved many of the requirements of an actual reactor under a physical point of view. Nevertheless technological issues persist such as the need for superconducting and expensive magnets to generate the large toroidal field. A major problem is also related to the strong toroidal current: the concept previously illustrated in Figure 3 uses a transformer to induce the plasma current and this method works perfectly for experimental pulsed devices. An operative reactor though would clearly be a steady state device and the toroidal current needs to be generated by other means. The discovery of the *bootstrap current*, generated naturally by plasma radial transport [43], has given a viable solution to the problem. The bootstrap current though is found to be proportional to the poloidal beta, high currents would therefore require high pressure, beyond the MHD β limits. Severe MHD instabilities would rise and spoil the discharge. The presence of a resistive wall as plasma boundary would reduce the growth rate of these instabilities and allow feedback stabilization. The Advanced Tokamak (AT) [44][45][46] concept has been developed with the aim of sustaining fully non-inductive discharges with a combination of self-generated and external current drive. Given that the bootstrap current is found to be proportional to the poloidal beta ($\beta_p = 2\mu_0\langle p\rangle/\langle B_p^2\rangle$, with B_p the poloidal magnetic field) and the requirement of operating at high toroidal beta to sustain the fusion reaction, the resulting condition is to

Bootstrap Current

Advanced Tokamak

operate at high normalized beta (β_N). The following relationship holds between these three parameters:

$$\beta_p \beta_T \sim 25 \left[\frac{(1 + E^2)}{2} \right] \left(\frac{\beta_N}{100} \right)^2 \tag{39}$$

where E is the plasma elongation. It is presently thought that an attractive reactor-like scenario should be able to provide at least 75% of the total current through the bootstrap mechanism, leaving about 25% to be fed by external current drive. As a consequence of the above relationship, high-bootstrap-fraction Tokamaks will probably face the RWM issue. AT scenarios can take advantage of the existence of Internal Transport Barriers (ITBs), which bring improved confinement with respect to H-mode operation. Furthermore, it has been seen that ITBs and AT operation give rise to high bootstrap current fractions because of the naturally hollow current profiles.

2.7 REVERSED FIELD PINCH

The basic idea behind the Reversed Field Pinch (RFP) configuration is, as for the Tokamak, plasma confinement with the so-called pinch effect: the passage of an unidirectional current in the plasma creates an azimuthal magnetic field that constricts (pinches) the plasma resulting in magnetic confinement. The toroidal pinch has historically been the first system based on the pinch effect, on which a great deal of research has been accomplished since the 1950s. Early pinches presented serious stability issues due to kinks and other MHD modes. While in the Soviet Union research led to the development of the Tokamak configuration described in the previous section, European and American experiments also explored other directions such as the RFP configuration. Early Z-pinch and RFP devices are for instance: *Zeta-experiment* and *HBTX-I* in the UK, *ZT-I* and *ZR-II* in the US, *Eta-Beta-I* followed by *Eta-Beta-II* in Padova. A description of these experiments is beyond the introductory aims of this chapter and can be found in [47]. An RFP device is an axis-symmetric toroidal system (Figure 4) in which plasma confinement is obtained with a poloidal magnetic field B_θ, mostly produced by a current flowing in the plasma itself, combined with a toroidal field B_ϕ generated by a set of external coils. Like in the Tokamak configuration these two components form a helical total field. In the RFP case the two components are approximately of the same magnitude $B_\theta \sim B_\phi$, while in a Tokamak

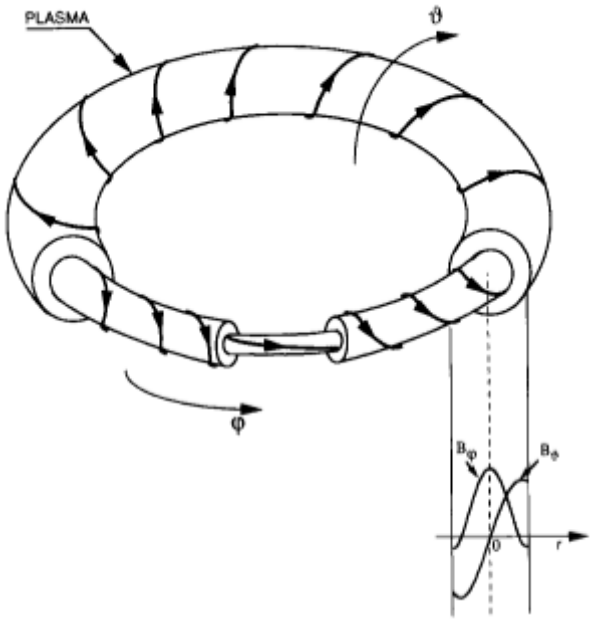

Figure 4: Scheme of a Reversed Field Pinch plasma ring with typical field profiles [48].

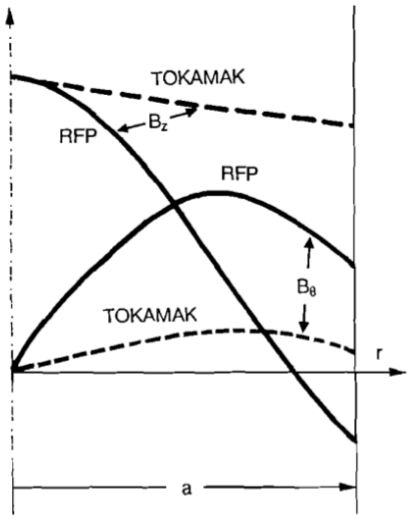

Figure 5: Radial field profiles for toroidal and poloidal components of the magnetic field. Dashed line represents Tokamak and solid line RFP [49].

the profiles would be very different, as can be seen in Figure 5.

Pinch and Reversal Parameters

The RFP configuration can be characterized by two parameters:

$$\Theta = \frac{B_\theta(a)}{\langle B_\phi \rangle} \propto \frac{I_p}{\Phi_t} \qquad F = \frac{B_\phi(a)}{\langle B_\phi \rangle} \tag{40}$$

respectively named *pinch parameter* and *reversal parameter*, where $B_{\phi/\theta}(a)$ are the toroidal and poloidal fields measured at the boundary, $\langle B_\phi \rangle$ is the toroidal field averaged on the poloidal section and Φ_t is the toroidal magnetic flux. Compared to the Tokamak case, $\Theta_{RFP} \gg \Theta_{TOK}$. Therefore the main difference between the two configurations lies in the fact that the same magnetic flux (generated by the central solenoid) gives a much greater current in an RFP with respect to a Tokamak. Furthermore, RFP safety factor profiles are typically monotonically decreasing, and with respect to Tokamaks $q_{RPF} \ll 1 \ll q_{TOK}$ because of the relatively higher plasma current.

$$q(r) = \frac{rB_\phi}{RB_\theta(r)} \propto \frac{B_\phi}{I_p} \tag{41}$$

Another characteristic of RFP configurations is that, as a consequence of the above discussion, the toroidal magnetic field tends to change sign (i. e.reverse) at the plasma boundary, therefore $q(a) < 0$. Such a system operates beyond the Kruskal-Shafranov limit, MHD stability is achieved with a combination of sheared magnetic field (obtained due to the reversing of B_ϕ) and conducting shell at plasma boundary. Similarly to the Tokamak case this external wall would stabilize XK modes if perfectly conducting but a realistic situation involves walls with finite resistivity, thus requiring some sort of feedback stabilization. These operation conditions also lead to the development of m=1 resistive kinks (i. e.a helical deformation of the plasma). These modes evolve non-linearly and give rise to a fluctuation induced electric field $E_f = -\langle \mathbf{v} \times \mathbf{B} \rangle$ which enters the Ohm's law and sustains the RFP configuration by removing parallel current gradients. This is the so-called dynamo. At low current, many of these resistive modes are simultaneously unstable with different toroidal numbers n, this represents the so-called Multiple Helicity regime. One early theoretical model for RFP equilibria has been obtained by Taylor [50]: starting from a perfectly conducting plasma model, assuming the total magnetic helicity and magnetic flux conservation leads to a unique equilibrium state characterized by the aforementioned reversal and

Dynamo

pinch parameters. Taylor's relaxation theory has found quite good agreement with experimental results. The pinch parameter on the magnetic axis Θ_0 is also important in the μ&p model describing RFP equilibrium [51] [49]. This theory however, only captures RFP physics qualitatively and clearer results are given by the MHD model. The presence of Single Helicity states for instance, has been predicted by MHD simulations [52]. Under the experimental point of view, in large RFP devices a transition from Multiple Helicity to the so-called Quasi Single Helicity states has been seen [53] [54] [55], persisting for the whole discharge flat top at high (1 MA) current [56]. Rather recent developments on RFX-mod have seen the experimental verification of the self-organized helical state that develops at high current ($>$ 1.5 MA) and is connected with the presence of an internal transport barrier [57]. Improving optimization of the feedback control system has allowed for high current operation and for the so-called quasi-single-helicity high persistence [58] [39] [59].

RFP fusion experiments have both advantages and disadvantages compared to Tokamak ones. For instance smaller currents are be needed by the external coils to generate the modest toroidal fields involved. On the other hand the achieved τ_E values are low because of transport phenomena. Complex active control systems are installed on modern RFP devices such as RFX-mod, in order to stabilize Resistive Wall Modes and thus improve pulse duration. These control systems must be capable of dealing with multiple instabilities which are simultaneously present in a Reversed Field Pinch, this makes them perfect benchmark environments also for Tokamak stability studies in which more than one mode is unstable.

3

MARS-K FORMULATION: TOROIDAL NON-PERTURBATIVE MHD-KINETIC HYBRID PLASMA DESCRIPTION

"[...] Stars, hide your fires;
let not light see my black and deep desires."

— William Shakespeare, Macbeth

The MAgnetohydrodynamic Resistive Spectrum (MARS) code solves single-fluid linearized MHD equations in full toroidal geometry. MARS-K [32] represents an extension of the MARS-F code [40] which adds drift-kinetic effects to the fluid plasma description with toroidal flow and sound wave damping. The full set of linearized equations, which is solved as an eigenvalue problem with γ being the sought value, reads [60]:

$$(\gamma + \imath n\boldsymbol{\Omega})\,\boldsymbol{\xi} = \mathbf{v} + (\boldsymbol{\xi}\cdot\nabla\boldsymbol{\Omega})\,R^2\nabla\Phi \tag{42}$$

$$\begin{aligned}(\gamma + \imath n\boldsymbol{\Omega})\,\mathbf{v} = &-\nabla\cdot\mathbf{p} + \nabla\times\mathbf{Q}\times\mathbf{B} + \nabla\times\mathbf{B}\times\mathbf{Q} + \\ &- \rho\left[2\boldsymbol{\Omega}\nabla Z\times\mathbf{v} + (\mathbf{v}\cdot\nabla\boldsymbol{\Omega})\,R^2\nabla\Phi\right] + \\ &- \nabla\cdot(\rho\boldsymbol{\xi})\,R^2\boldsymbol{\Omega}^2\nabla Z\times\nabla\Phi\end{aligned} \tag{43}$$

$$(\gamma + \imath n\boldsymbol{\Omega})\,\mathbf{Q} = \nabla\times(\mathbf{v}\times\mathbf{B}) + (\mathbf{Q}\cdot\nabla\boldsymbol{\Omega})\,R^2\nabla\Phi \tag{44}$$

$$\mathbf{p} = p_{\parallel}\hat{\mathbf{b}}\hat{\mathbf{b}} + p_{\perp}\left(\mathbf{I} - \hat{\mathbf{b}}\hat{\mathbf{b}}\right) \tag{45}$$

Where Ω is the fluid rotation frequency along the toroidal angle Φ. It is worth noting that the toroidal flow $\boldsymbol{\Omega}$ represents the bulk ion rotation, which is the sum of the equilibrium $\mathbf{E}\times\mathbf{B}$ flow and the ion diamagnetic flow. These components are not separable in the standard single-fluid description on which this hybrid formulation is based. The perturbed quantities $\xi, \mathbf{v}, \mathbf{p}, \mathbf{Q}$ represent respectively plasma displacement, perturbed velocity, pressure tensor and magnetic field. The assumed form of all perturbations is $A(s,\chi,\Phi,t) = A(s,\chi)e^{-i\omega t - in\Phi}$, in a curvilinear flux coordinate system (s,χ,Φ) where s is the normalized radial coordinate and χ the generalized poloidal angle. $\mathbf{B}$ is the equilibrium magnetic field. ρ is the unperturbed plasma density, $\mathbf{I}$ the unit tensor and $\hat{\mathbf{b}} = \mathbf{B}/|\mathbf{B}|$ is the equilibrium magnetic field unit vector. (R,Φ,Z) is the cylindrical coordinate system for the torus. The MHD-kinetic equations above are solved in

$$s \equiv \sqrt{\frac{(\psi-\psi_{axis})}{(\psi_{edge}-\psi_{axis})}}$$

the just mentioned magnetic flux surface based curvilinear coordinate system, this is not an orthogonal system in general since the radial and poloidal coordinates are not orthogonal to each other. The generalized poloidal angle in particular depends on the choice of the Jacobian (referring to the transformation between contra-variant and covariant basis). In the work presented within the following chapter, an *equal-arc* coordinate system is used, for which $dl/d\chi = \sqrt{g_{\chi\chi}}$ is constant on a flux surface, where $g_{\chi\chi} = \mathbf{e}_\chi \cdot \mathbf{e}_\chi$ is a metric element.

Drift-kinetic effects are included in the Equations 42-45 through the perturbed pressure tensor components $p_\parallel$ and $p_\perp$. These terms, which are calculated with the following integrals over the particle velocity space Γ, replace the standard adiabatic closure $5/3P\nabla\mathbf{v}$ (where P would be the equilibrium pressure):

$$p_\parallel e^{-i\omega t+in\Phi} = \sum_{e,i}\int d\Gamma M v_\parallel^2 f_1^{th} + \int d\Gamma M v_\parallel^2 f_1^h \tag{46}$$

$$p_\perp e^{-i\omega t+in\Phi} = \sum_{e,i}\int d\Gamma M \frac{1}{2} v_\perp^2 f_1^{th} + \int d\Gamma M \frac{1}{2} v_\perp^2 f_1^h \tag{47}$$

Where the summations run over electrons and ions, M is the particle mass, $v_\parallel$ and $v_\perp$ the particle velocity components respectively parallel and perpendicular to the equilibrium magnetic field. The perturbed distribution functions for thermal particles (f_1^{th}) and fast ions (f_1^h) are derived for each specie following the approaches in [61] and [62], with the MARS-K implementation being described in [32].

In the work described in this thesis, Chapter 9 in particular, a slowing down equilibrium distribution is assumed for fast ions in the energy space and isotropic in the pitch angle. Although this is a rough approximation for additional heating hot ions, it has been chosen as a starting point for assessing the effect of fast particles Resistive Wall Mode stability in the considered scenarios. Following [63] and [64], the slowing down equilibrium fast ions distribution can be described as:

$$f_0^h = \begin{cases} \frac{C}{\epsilon_k^{3/2}+\epsilon_c^{3/2}} & 0 < \epsilon_k < \epsilon_{max}, \\ 0 & \epsilon_k > \epsilon_{max}. \end{cases} \tag{48}$$

Where

$$\epsilon_c = \left(\frac{3\sqrt{\pi}}{4}\right)^{2/3}\left(\frac{M_h}{M_i}\right)\left(\frac{M_i}{M_e}\right)^{1/3} T_e \tag{49}$$

While the parameter C can be calculated through the fast particles density profile $N_h = \int f_0^h d\Gamma$ as:

$$C = N_h M_h^{3/2} A, \qquad A = \left(4\sqrt{2}\pi \int_0^1 \frac{\tilde{\epsilon}_k^{1/2} d\tilde{\epsilon}_k}{\tilde{\epsilon}_k^{3/2} + \tilde{\epsilon}_c^{3/2}} \right)^{-1} = \frac{3}{8\sqrt{2}\pi} \frac{1}{\ln\left(1 + \tilde{\epsilon}_c^{-3/2}\right)} \tag{50}$$

Where in the above equations M_i, M_e, M_h are the masses of ions, electrons and fast particles respectively, T_e is the electron temperature, $\tilde{\epsilon}_k \equiv \epsilon_k/\epsilon_{max}$ and $\tilde{\epsilon}_c = \epsilon_c/\epsilon_{max}$. The particle maximum energy ϵ_{max} is generally a function of the minor radius and determined from the fractions P_h/P_{th}, N_h/N_{th} where h stands for hot and th for thermal particles.

$P_{h,th}$ *pressure components for fast ions and thermal particles*

$N_{h,th}$ *density components for fast ions and thermal particles*

The energy analysis module included in MARS-K allows for deeper understanding of RWM physics. Components of the quadratic energy form [7] [4] are calculated for both fluid and kinetic energy perturbations. In the present work we will focus on the analysis of the kinetic part of the perturbed potential energy, which is obtained from the parallel and perpendicular components of the pressure tensor when multiplying Equation 43 by the plasma displacement and integrating over the plasma volume:

$$\delta W_k = \frac{1}{2} \int_{V_p} \left[\frac{1}{B} p_\perp \left(Q_\parallel^* + \nabla B \epsilon_\perp^* \right) + p_\parallel \boldsymbol{\kappa} \cdot \boldsymbol{\epsilon}_\perp^* \right] J ds d\chi d\Phi \tag{51}$$

This is in general a complex quantity and can be written as: $\delta W_k = \delta W_k^{re} + i\delta W_k^{im}$. Substituting this expression in the generalized dispersion relation for Resistive Wall Modes with kinetic effects [28][65]:

$$\gamma \tau_w^* = -\frac{\delta W_\infty + \delta W_k}{\delta W_b + \delta W_k} \tag{52}$$

It is the straightforward to obtain, by taking the real part of Equation 52, the stability condition:

$$\delta W_\infty \delta W_b + \delta W_k^{re} \left(\delta W_\infty + \delta W_b \right) + (\delta W_k^{re})^2 + \left(\delta W_k^{im} \right)^2 > 0 \tag{53}$$

Where $\delta W_\infty = \delta W_F + \delta W_{v,\infty}$ and $\delta W_b = \delta W_F + \delta W_{v,b}$. With $\delta W_{v,\infty}$ and $\delta W_{v,b}$ being the vacuum energy without and with an ideal wall at minor radius b respectively. δW_F is the fluid potential energy. It follows that the imaginary part of the kinetic

potential energy always brings a stabilizing effect, while the real part can be either stabilizing or destabilizing. The global effect has to be evaluated taking into account all the particle populations and resonances included in the applied mode. Using the MARS-K MHD-kinetic hybrid self-consistent formulation, the drift-kinetic potential energy can be written as reported in [32]:

$$\delta W_k = \frac{\nu\sqrt{\pi}}{2B_0} \sum_{e,i} \int d\Psi P_{e,i} \left\{ \int d\hat{\epsilon}_k \hat{\epsilon}_k^{5/2} e^{-\hat{\epsilon}_k} \cdot \right. \\ \left. \cdot \sum_{\sigma} \left[\int d\Lambda \sum_{l} \lambda_l^{\alpha} \hat{\tau}_b |\langle e^{-i(l+\alpha n q)\omega_b t - in\Phi} H_L \rangle_l|^2 \right] \right\} \tag{54}$$

Where B_0 is the on-axis magnetic field, $P_{e,i}$ the equilibrium pressures for electrons and ions, $\hat{\epsilon}_k = \epsilon_k/T$ the normalized particle energy, $\sigma = sign(v_{\|})$, Λ is the pitch-angle and λ_l^{α} the mode-particle resonance operator. Summations run over particle species (e, i), poloidal Fourier harmonics, trapped and passing particles. The last factor, H_L, is the particle perturbed Lagrangian [32]. The parameters ν, α and $\hat{\tau}_b$ depend on the specific population. In general $\alpha = 0$, $\nu = 1/2$ for trapped particles with $\hat{\tau}_b = \tau_b/\sqrt{M/2\epsilon_k}$ being the normalized bounce period and $\alpha = 1$, $\nu = 1$ for passing particles, with $\hat{\tau}_b$ being the normalized transit period.

4

INTRODUCTION TO CONTROL THEORY

"A world is supported by four things ...
... the learning of the wise, the justice of the great,
the prayers of the righteous and the valor of the brave.
But all these things are nothing,
without a ruler who knows the art of ruling."

— Frank Herbert, Dune

The ideas of control theory, and feedback in particular, are nowadays important for many physical applications and experiments. Let us consider a physical system whose output is the studied observable variable, the word *control* identifies the actions aimed at driving its time evolution towards the desired direction. In the feedback approach the output variable is compared with an externally applied reference and driven as to match this reference. In the discussion that follows a theoretical background on the study of linear systems is given. Both the continuous and discrete time situations are considered because many modern control applications make use of a digital computer to generate the control input reference. The digital computer together with a digital-to-analog converter form what is usually called a digital controller.

4.1 STATE VARIABLE REPRESENTATION OF A LINEAR TIME INVARIANT SYSTEM

Let us consider a generic system, with the point of view of control theory, as the mathematical tool that models the dynamics of a given physical process. Three kind of variables are used in the present description: *input* variables (u_i) represent the external forces that influence the dynamics, *output* variables (y_j) are connected to the physical observable and *state* variables (x_q) represent internal characteristics of the system. Knowing x_q at a given time and u_i for that time onward, the output variables y_j and the remaining states are completely determined. Time can be considered both continuous, defining the *continuous* linear system $u_i(t)$, $y_j(t)$, $x_q(t)$, and discrete, thus defining a *discrete* system in which the state variables are sequences depending on

discrete time: $u_i(t_k)$, $y_j(t_k)$, $x_q(t_k)$[66]. Every system can have multiple state variable representations but all of them have the same number of states, i.e. the number of elements (n) in the state vector is fixed for each system and is referred to as the *order* of the system. State variables for a generic system are usually defined by first order differential equations:

$$\dot{x}_q(t) = f_q\left[\vec{x}(t_0), \vec{u}(t_0, t)\right]$$

Output variables on the other hand are determined by the state vector $\vec{x}(t)$ and the input vector $\vec{u}(t)$:

$$y_j(t) = g_j\left[\vec{x}(t), \vec{u}(t)\right]$$

These equations can be put into vector form to give the most generic representation of a continuous system:

$$\begin{aligned} \dot{\vec{x}}(t) &= \mathbf{f}\left[\vec{x}(t), \vec{u}(t)\right] \\ \vec{y}(t) &= \mathbf{g}\left[\vec{x}(t), \vec{u}(t)\right] \end{aligned} \tag{55}$$

A block representation of this system is given in Figure 6. In the case of a generic discrete system with evenly spaced time steps ($t_k - t_{k-1} = T$) Equation 55 becomes:

$$\begin{aligned} \vec{x}(k+1) &= \mathbf{f}\left[\vec{x}(k), \vec{u}(k)\right] \\ \vec{y}(k) &= \mathbf{g}\left[\vec{x}(k), \vec{u}(k)\right] \end{aligned} \tag{56}$$

This discrete system is not given for the the sake of curiosity, in

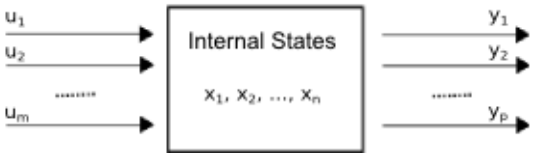

Figure 6: State variable representation of a generic system

many modern applications digital controllers are involved such is the case on RFX-mod. Computer based simulations are another example, every routine used in the present work is based on discrete blocks that appear similar to Equation 56. To be more precise, systems in the aforementioned routines are considered to be linear, hence Equations 55 and 56 can be respectively put into the simple form:

$$\begin{aligned} \dot{\vec{x}}(t) &= \mathbf{F}\vec{x}(t) + \mathbf{G}\vec{u}(t) \\ \vec{y}(t) &= \mathbf{C}\vec{x}(t) + \mathbf{D}\vec{u}(t) \end{aligned} \tag{57}$$

$$\begin{aligned}\vec{x}(k+1) &= \mathbf{A}\vec{x}(k) + \mathbf{B}\vec{u}(k)\\ \vec{y}(k) &= \mathbf{C}\vec{x}(k) + \mathbf{D}\vec{u}(k)\end{aligned} \tag{58}$$

where in the latter **A** is called the $n \times n$ state matrix, **B** is the $n \times m$ input matrix, **C** the $p \times n$ output matrix and **D** the $p \times m$ input-output matrix. This is a useful representation for the RFX-mod control system, in this case the input vector contains 192 signals that are fed to the power supplies and the output vector the 192 signals sampled by the saddle coil sensors covering the internal surface of the shell. Such a system is also called a Multiple-Input-Multiple-Output (MIMO) system to remark the difference with the Single-Input-Single-Output case. A simplified version of this MIMO system is obtained by dropping the **D** matrix, since the input vector hardly has any direct effect on the output.

Multiple-Input-Multiple-Output (MIMO)

$$\begin{aligned}\dot{\vec{x}} &= \mathbf{A}\vec{x} + \mathbf{B}\vec{u}\\ \vec{y} &= \mathbf{C}\vec{x}\end{aligned}$$

A convenient method for studying n^{th} order linear systems is analysis in the frequency domain by means of the Laplace transform, defined by the following operator [67]:

Laplace Transform

$$\mathcal{L}[x(t)] = x(s) = \int_0^\infty x(t)e^{-st}dt \tag{59}$$

The Laplace transform can be related to the Fourier transform by imposing $s = i\omega$, it gives nevertheless a better approach to the linear system under study because of the evolution time starting from $t = 0$ instead of $t = -\infty$ and also because of the capability of reducing an n^{th} order differential equation in the time domain to an n^{th} order algebraic equation in the s domain. This characteristic of the Laplace transform is given by the following properties:

$$\begin{aligned}\mathcal{L}\left[\frac{d^n x}{dt^n}\right] &= s^n x(s)\\ \mathcal{L}\left[\int x(t)dt\right] &= \frac{1}{s}x(s)\end{aligned}$$

these allow to write the input and output of a linear system as polynomials in s, in particular the *transfer function* of the system can be defined:

$$G(s) = \frac{y(s)}{u(s)} = \mathbf{C}\left(s\mathbb{I} - \mathbf{A}\right)^{-1}\mathbf{B} \tag{60}$$

Transfer functions are extremely useful objects to study linear systems, describing the input-output relationship and also yielding information on stability. This description of linear time-invariant systems has some important advantages: as previously stated it allows to substitute differential equations with algebraic equations, the output of the system is easily obtained by multiplication while time evolution is calculated through inverse Laplace transform, furthermore complex system can be represented with simple block diagrams.

4.2 FEEDBACK CONTROL

A block diagram of a hypothetical closed-loop system is given in Figure 7. The controlled output $y(t)$ is required to follow the input reference $r(t)$, thus the controller is fed with the so-called *error signal* $e(t) = r(t) - y(t)$, that is multiplied by the transfer function K which applies the desired control law. Using the Laplace transform the global transfer function is obtained:

$$y(s) = K(s)M(s)G(s)e(s)$$
$$e(s) = r(s) - H(s)y(s)$$

therefore:

$$y(s) = \frac{K(s)M(s)G(s)}{1 + K(s)M(s)H(s)G(s)}r(s) = \frac{K(s)M(s)G(s)}{1 + L(s)}r(s)$$

where $L(s) = K(s)M(s)H(s)G(s)$ is called *loop gain* and determines the dynamics of the whole system. An equivalent block diagram for the open-loop case is given in Figure 8.

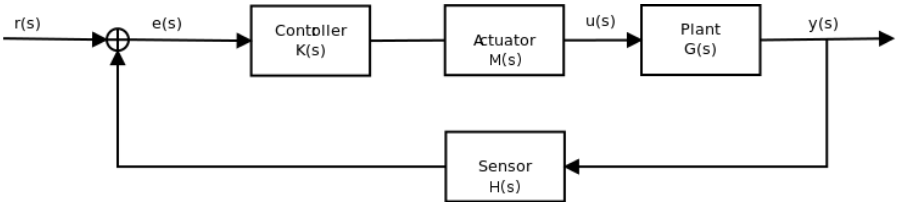

Figure 7: Block diagram representing feedback control of a system with transfer function $G(s)$. The controller has its own transfer function $K(s)$ that describes its dynamics. $M(s)$ and $H(s)$ are the transfer functions of the actuators and sensors respectively.

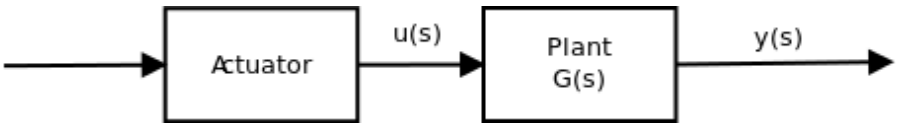

Figure 8: Block diagram representing the signal flow from the input $u(s)$ to the output $y(s)$ obtained with the transfer function $G(s)$.

The regulator applied by $K(s)$ can follow three different approaches: *proportional* (K_p), *integral* (K_i), *differential* (K_d) or a combination of these. On RFX-mod all three the techniques are combined in a Proportional-Integral-Derivative (PID) controller, its transfer function in the s domain appears as the following:

$$K(s) = K_p + \frac{K_i}{s} + K_d s \tag{61}$$

where K_p, K_i and K_d are in general complex numbers externally applied by the user. Varying these parameters will modify the system's eigenvalues thus affecting stability. For the sake of simplicity the RWM control simulations carried out in this work, as well as the analyzed experiments, make use of a purely proportional gain in most of the cases. Just a few examples will be given of mode control with both proportional and integral regulators.

5

MAGNETIC CONFINEMENT FUSION EXPERIMENTS

"We have no need of other worlds. We need mirrors.
We don't know what to do with other worlds.
A single world, our own, suffices us;
but we can't accept it for what it is."

— Stanisław Lem, Solaris

Aim of this Chapter is to give an overview of the experimental devices on which the studies in the present thesis have been carried out. The first to be described in Section 5.1 if the RFX-mod experiment, operating in Padova up to 2015 and now being upgraded. The second part, Section 5.2 is dedicated to the description of JT-60SA, which is being built in Naka (Japan) within the framework of the Broader Approach agreement between Japan and the European Union.

5.1 REVERSED FIELD EXPERIMENT

The Reversed Field eXperiment (RFX-mod) is a medium size (R = 2 m, a = 0.459 m) toroidal device that has been operating in Padova since 2004. Originally designed as an RFP experiment [68], it is capable of confining plasmas also in the Tokamak configuration [3]. It is equipped with a state-of-the-art system for active control of MHD instabilities [69]. Such a system, operating with a cycle frequency from 2.5 to 5 kHz, is composed of 192 independently fed actuators (saddle coils arranged into a 4×48 grid), located on the outer surface of a stainless steel support structure at r=0.6 m, and a considerable set of magnetic sensors counting 192 bi-axial pick-up probes (measuring toroidal and poloidal B components) and 192 saddle sensors for the radial component[70] . Each active coil can be fed a maximum current of 400 A, providing a DC radial field of 46 mT at the vacuum vessel surface. The radial component of the magnetic field in particular, is measured by 192 saddle probes whose positions correspond to the projection of the actuators on the outer surface of the vacuum vessel, at minor radius r=0.505 m. The high degree of flexibility of the control system, working in

a bi-dimensional Fourier space characterized by the poloidal (m) and toroidal (n) mode numbers, allows to switch on or off each single coil. Many control schemes can thus be easily implemented[36] and the controller has the capacity to independently act on selected modes with different sets of coils. A representation of RFX-mod with its most important active and passive structures is given in Figure 9. The device is currently undergoing a major upgrade which will involve both the vacuum vessel [71] and the active system. The main technical specifications of the latest operating machine are reported in Table 1. The copper shell which can be seen in Figure 9 is 3 mm

Minor radius (a)	0.427 m
Major radius (R)	2 m
Plasma current	$\leqslant$ 2 MA
β	10%
T_e	1 keV
Applied toroidal field	$<$ 0.55 T
Magnetic circuit flux	15 Wb

Table 1: RFX-mod technical specifications.

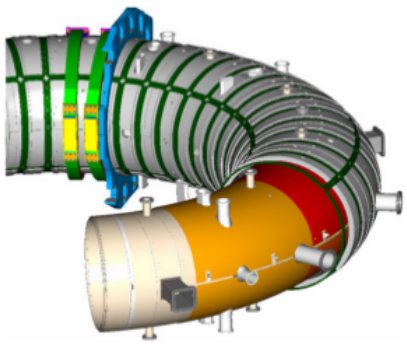

Figure 9: Graphical representation of RFX-mod active coils (green), passive support structures (grey), copper shell (orange) and vacuum vessel (yellow).

thick and has a vertical field penetration time of $\tau_{shell} = 50$ ms that allows feedback stabilization of MHD modes, given that the discharge duration time scale is one order of magnitude longer. The shell has two gaps respectively along the poloidal and toroidal directions, an exploded view is given in Figure 10. These gaps in the shell are technically necessary but are also

a source of error fields produced by eddy currents. The torus is entirely covered with the 192 active saddle coils, Figure 12a, arranged in 4 toroidal arrays and 48 poloidal sections. The saddle coils are located outside the copper shell and mounted on a stainless steel toroidal support structure. Each coil is independently fed, carries a maximum current of 400 A producing a local maximum radial field of ~ 50 mT. The magnetic measure-

Figure 10: Exploded view of the copper shell.

ments used for mode control are supplied by dedicated probes, for each component of the magnetic field (poloidal, toroidal, radial) an array of 192 sensors is present. The poloidal and toroidal components are measured by pick-up probes while the radial field is obtained with saddle coil probes located under each of the previously described active control coils. These saddle probes have therefore the same periodicity of the active ones and span the same poloidal and toroidal angles, measuring the average radial field over the probe area. The whole system is controlled by a PID controller that works both in the real space, applying gains to field signals, and in the (m, n) Fourier space where gains are applied to Fourier harmonics ranging between $n = [-23; +24]$ and $m = [-1, 0, +1, +2]$. This actuator system proves to be very flexible to experimental needs, allowing both the usage of a reduced set of coils and of the so-called supercoils, i. e.a set of neighboring coils fed in a way so that they resemble a single bigger coil (Figure 11). Three more sets of

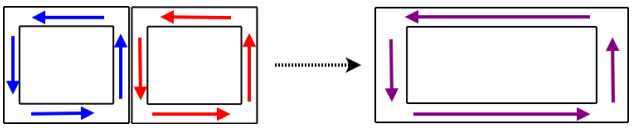

Figure 11: Graphical representation of two neighbouring coils used as a single one.

Toroidal Field Coils

Ohmic Heating Windings

Field Shaping Coils

coils contribute to generate the magnetic configuration. The 48 toroidal field coils (Figure 12c) wrap the whole torus and generate a maximum 0.55 T toroidal magnetic field. These coils are grouped in 12 blocks of 4 coils each independently fed. The magnetizing coils (Figure 12d) provide the time varying magnetic flux that gives rise to the plasma current. A maximum of 50 kA flowing in these coils produce a 15 Wb flux. A second poloidal field is generated by the so-called primary winding and it controls plasma position during the discharge (Figure 12b).

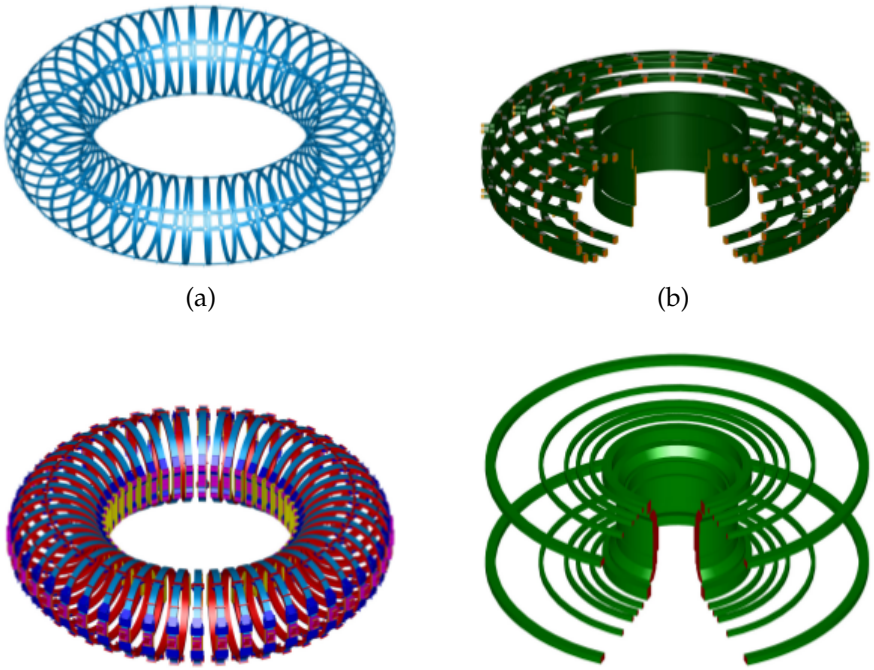

(a) (b) (c) (d)

Figure 12: (a) 192 actuators of the active control system, (b) field shaping winding, (c) 48 toroidal field coils, (d) Ohmic heating winding.

5.1.1 *RWM control with a reduced set of coils*

The number, shape and positioning of control coils has a direct impact on stability properties of RWMs. In principle varying the active coil configuration can trigger different plasma responses, since the externally applied field influences both the feedback control chain and plasma behavior. Amplification of otherwise stable modes is in fact possible through the side-bands of the external field and depending on the target plasma this effect

might have important consequences on stability. A hypothetical large and dense coil array covering the whole torus would intuitively be more powerful that a few sparse coils in term of control capabilities and side-band effect reduction. Very big arrays though might be difficult to obtain because of realization and maintenance costs, this is just one of the reasons why testing different control schemes is crucial in sight of the commercial exploitation of fusion energy. Changing active coils configuration is a very difficult task if working on the hardware, RFX-mod on the other hand allows software downgrading the control scheme thanks to the real time controller. This flexible system is also capable of applying different control sequences to selected harmonics, for example in a hypothetical RFP configuration experiment the unstable $m = 1$ $n = -6$ harmonic can be controlled with the desired set of coils and gains while the full array still works on other harmonics. Extensive studies have been carried out in dedicated experimental sessions to comprehend the effect of control downgrading on plasma stability[36]. As previously mentioned, an interesting feature of the real time control system is the possibility of averaging the currents in two or more neighboring coils to make them act as single larger super-coil, thus opening many other possible configurations. A set of modeling tools have been developed to test different coil geometries, good agreement has been obtained with experimental data, as reported in Figure 14, which allows for predictive simulations. The same tools will be extended and used in the following parts of this thesis.

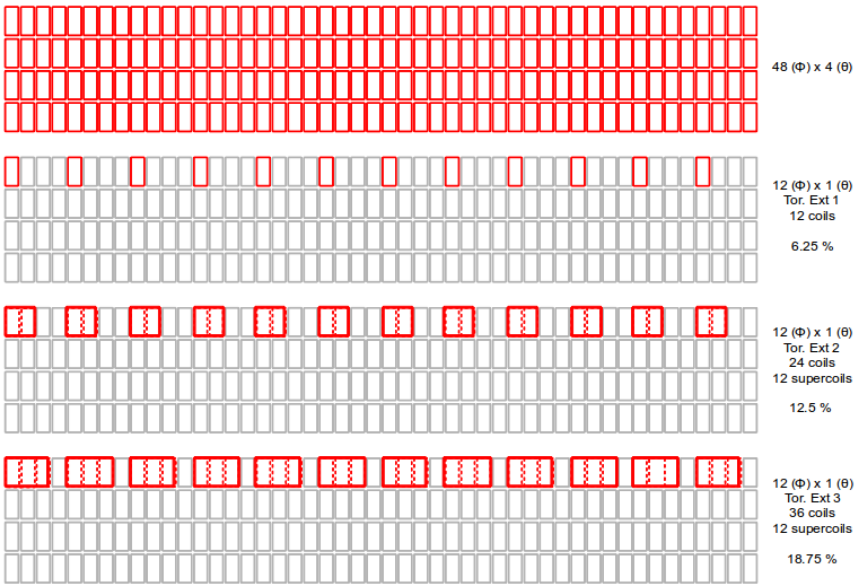

Figure 13: Rectified representation of some sample control configurations, on the right side the number of active coils along the toroidal (ϕ) and poloidal (θ) directions, the total number of active coils, the number of supercoils and the area coverage expressed as percentage.

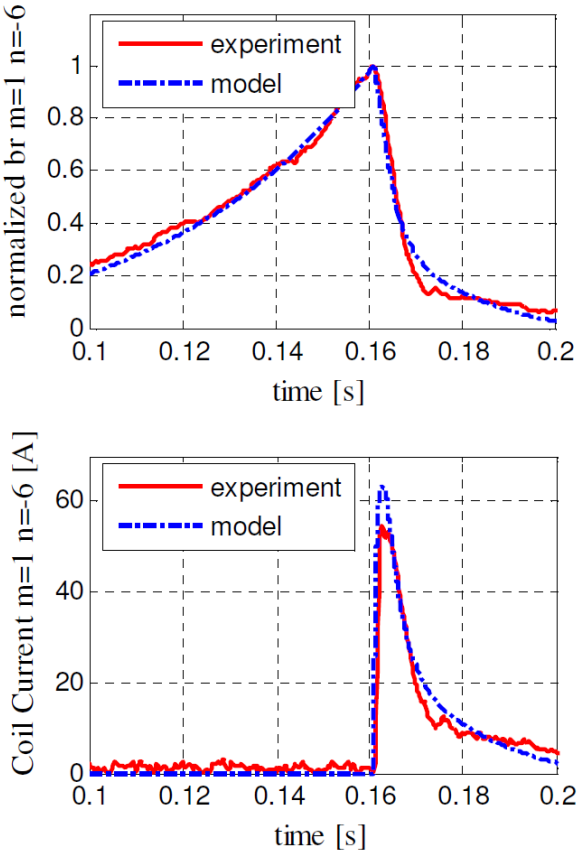

Figure 14: 1×16 configuration is made of 16 super-coils along the outer toroidal array. Model results (blue) are compared to experimental data (shot 33977, red). Amplitude of (1,-6) RWM (top) and coil currents for the same harmonics (bottom) are shown. Feedback starts at 0.16s.

5.2 JT-60SA

The superconducting device Japan Torus Super Advanced (JT-60SA) [72][73] is being built in Naka (Japan) and has an important supporting mission for the development of fusion energy: designed to achieve long pulses (100 s) and break-even equivalent plasmas, using superconducting poloidal and toroidal field coils. It will help in both the exploitation of ITER and in solving key issues for the future DEMO devices [74]. JT-60SA will be able to explore plasma configurations with shape factor up to $S = q_{95} I_p / (a B_\phi) \sim 7$ (where B_ϕ is the toroidal field, I_p the plasma current in MA, a is the minor radius, q_{95} the safety factor at 95% of the toroidal flux) and aspect ratio down to A 2.5. The maximum plasma currents are 5.5 MA in a low aspect ratio, inductive, configuration and 4.6 MA in the ITER-shaped configuration. The device will also pursue fully non-inductive steady-state operation with high β plasmas exceeding the no-wall ideal MHD stability limits. Additional heating and current drive systems will provide up to 41 MW for 100s, divided between 34 MW neutral beam injection (10 MW of 500 keV N-NBI and 24 MW of 85 keV P-NBI)[1] and 7 MW of ECRF[2]. The off-axis N-NBI at 0.5 MeV beam energy in particular, allows current profile tailoring for Advanced Tokamak scenarios with fully non-inductive current drive. Figure 15 shows a cutaway of the JT-60SA device with the main external heating and current drive systems. The most important goal of JT-60SA in view of a DEMOnstration Power Station (DEMO) reactor concept is to demonstrate the sustainability of steady-state operation with integrated maximization of energy confinement factor, normalized beta β_N, bootstrap current fraction, plasma density normalized to the Greenwald density, fuel purity and radiation power. JT-60SA will in principle allow steady-state operation with the full exploitation of 10 MW/500 keV tangential N-NBI current drive and 7 MW of Electron Cyclotron Current Drive (ECCD). In the most ambitious Advanced Tokamak scenario the 2.3 MA of plasma current will be fully non-inductively driven, with a normalized beta $\beta_N = 4.3$.

JT-60SA will play a very important role in MHD stability and control studies. It will explore the kinetic stabilization effect of

1 Negative Neutral Beam Injector (N-NBI), Positive Neutral Beam Injector (P-NBI)

2 Electron Cyclotron Radio-Frequency (ECRF)

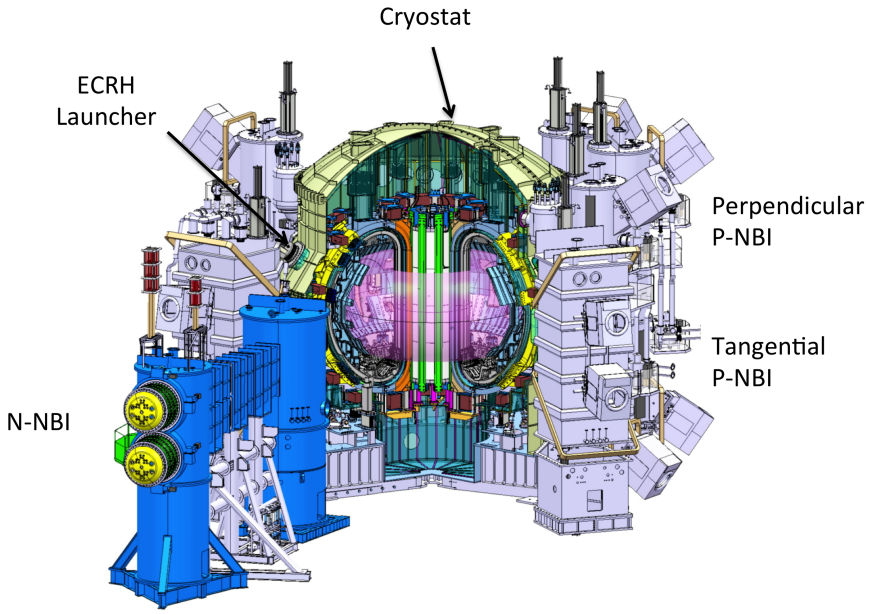

Figure 15: Cutaway view of the JT-60SA machine with external heating and current drive systems

energetic particles from 500 keV N-NBIs, investigating RWM stability for both ITER and DEMO relevant high β_N plasmas. ECCD will allow the validation of sawtooth control strategies for ITER hybrid scenarios, as well as real-time stabilization schemes of $m/n = 2/1$ and $3/2$ Neoclassical Tearing Modes (NTMs). Furthermore, JT-60SA will determine MHD stability boundaries by exploring RWM stabilization with active coils, sustaining long pulse high-β_N plasmas. The feasibility of this kind of operation depends on the controllability if disruptive instabilities such as RWMs and NTMs. JT-60SA is equipped with an in-vessel Stabilizing Plate (SP), made of SS316L and composed of two plates (1 cm thick) connected by ribs, for a total thickness of 9 cm. On the SP, Resistive Wall Mode Control Coils (RWMCC: 3 poloidal $\times$ 6 toroidal) are located, as well as Fast Plasma Position control Coils (FPPC) and Error Field Correction Coils (EFCC: 3 poloidal $\times$ 6 toroidal). All these components are shown in Figure 16. As far as RWMs are concerned, one the main goals is to develop effective feedback control strategies, along with investigating the combined effect of plasma rotation. Flexibility in tailoring rotation profiles is provided by various combinations of NBIs. In addition, high energy N-NBIs will allow to simulate burning plasmas where MHD instabilities are predicted to interact with high energy particles. A significant degree of flexibility in RWM studies is given by the feedback

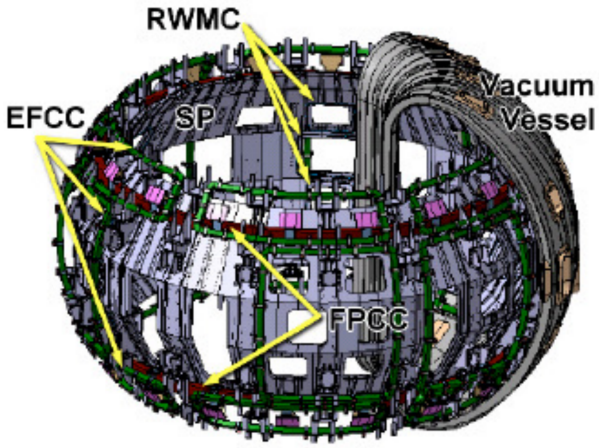

Figure 16: 3D view of the SP, Fast Plasma Position control Coils (FPPC), Resistive Wall Mode control Coils (RWMC: 3 poloidal × 6 toroidal) and Error Field Correction Coils (EFCC: 3 poloidal × 6 toroidal)

control system, particularly the RWMCC power supply which will have a very fast dynamic performance. Furthermore each coil will be fed by an independent inverter [75]. The main relevant features of this system, for the subject of the following Chapters, are given in Table 2. The RWMCCs, carrying a maximum current of 2.2 kAT each[3], will be installed on the plasma side of the SP. This will allow to minimize the shielding effect of the plate on the high frequency magnetic field modulation required by RWM control. With the mode control concept, stabilization studies on n=1,2 and 3 simultaneously will be possible.

Number of coils	3 poloidal × 6 toroidal
Number of turns per coil	8 turns
Max. peak current (sinusoidal)[a]	300 A
Bandwidth of the current at -3 dB	3 kHz
Maximum latency[b]	50 µs

[a] Maximum peak current per coil turn.

[b] Between the rise of a step reference and the change in output voltage.

Table 2: Main requirements of the JT-60SA RWM control system

3 kilo-Ampere-Turn

Part II

RFX-MOD CONTROL SYSTEM OPTIMIZATION

6

ACTUATOR-SENSOR DECOUPLING ON RFX-MOD

"The wise man will be as happy as circumstances permit, and if he finds the contemplation of the universe painful beyond a point, he will contemplate something else instead."

— Bertrand Russell, The Conquest of Happiness

[1]A series of techniques are presented that have been developed to optimize the output magnetic field of the feedback control system on the RFX-mod reversed field pinch device. With the aim of minimizing the harmonic distortion and correcting localized error fields, these methods should be lightweight for real-time application and effective in improving the performance of a system that is routinely used for active control of magneto-hydrodynamic plasma instabilities. The implementation of simple, linear algebra based, real-time optimization methods will be described along with proof of the sought beneficial effects. Focus of the work is set on a spurious harmonics reduction technique based on the decoupling of sensors and actuators, a description of its derivation will be given together with the implementation in the control loop. A similar procedure for the compensation of faulted actuators will also be mentioned.

6.1 THE COUPLING PROBLEM

In a control system such as the one described in Section 5.1, each of the 192 actuators will be coupled with the directly underlying saddle sensor and its neighbors. The magnetic field produced by single active coils will therefore influence the surrounding measurements, leading to a source of error fields once the feedback loop is closed. Performance improvements can be sought by making use of the coupling terms (i. e.mutual inductances) between actuators and sensors. Given the presence of passive structures in between, these coupling terms depend

1 The content of this Chapter is: *Pigatto, L., et al. "Control System Optimization Techniques for Real-Time Applications in Fusion Plasmas: the RFX-mod Experience" submitted for publication to IEEE-Transactions on Nuclear Science* and *Pigatto, L., et al. 41St EPS Conference on Plasma Physics, Berlin. P5.080*

on frequency and on the local characteristics of the passives (e. g.cuts, gaps etc.). In the following, the term *decoupling* will be used to define a family of techniques devoted to making each actuator aware of the existence of the neighboring sensors. Decoupling based optimization techniques have been developed with different concepts, such as the so-called dynamic decoupler [76] which relies on off-line pre-computed current distributions. In the present work we will concentrate on a different, lightweight method that can be applied real-time taking action on all the modes of the Fourier spectrum for a fixed frequency. Dedicated measuring campaigns have been carried out on RFX-mod, leading to the development of a full electromagnetic model of the MHD modes active control system[77]. Mutual coupling matrices between active coils can be derived for a given set of frequencies from the ratio between coil voltage ($\bar{V}_i$) and coil current ($\bar{I}_k$) phasors. The resulting complex number can account for the effects of passive structures on the magnetic flux:

$$\frac{\bar{V}_i(\omega)}{\bar{I}_k(\omega)} = \dot{Z}_{ik}(\omega) = Z_{ik}(\omega)e^{j\phi_{ik}(\omega)} = R_{ik} + j\omega\dot{L}_{ik}(\omega) \quad (62)$$

where the dot is used to represent complex matrices. The same procedure can be followed to measure the coupling terms between actuators and sensors, only changing the voltage phasor with the flux measured by each saddle sensor.

$$\frac{\bar{\Phi}_i(\omega)}{\bar{I}_k(\omega)} = \dot{M}_{ik}(\omega) \quad (63)$$

Once the response of the saddle sensors has been measured for the desired frequencies, full information on mutual couplings can be used to build a full state-space electromagnetic model. This *black-box* model derived from experimental data can be used to develop simplified strategies for improving the quality of harmonic content in output magnetic fields, taking into account the effect of toroidal geometry and coil-sensor couplings. Another way to proceed in challenging the decoupling problem, is making use of existing three-dimensional electromagnetic codes to obtain a first-principles description of the coils and passive structures. This has been done for the RFX-mod device with the CARIDDI code. From this second model, which will be described in Section 6.2, another state-space representa-

tion of the system is obtained from which the following transfer function can be calculated:

$$K(\omega) = \left[C(Ij\omega - A)^{-1}B + D \right] \tag{64}$$

where standard state-space notation is considered with the matrices A, B, C, D. By inverting the transfer function $K(\omega)$ for a given frequency, a matrix is obtained that can be used to account for the couplings and reduce the magnetic field harmonic distortion. Various matrices have been obtained with both the aforementioned methods and applied in simulations (details on the simulation tools are given is Section 6.2) and experiments. Some examples of these matrices are reported in Figure 17, from which the different magnitude of coupling can be appreciated with varying frequency and between experimental or model based calculations. Figure 17a and 17b represent the decoupling matrices obtained from experimental data for $\omega = 0, 10$ Hz, while Figure 17c is the inverse of the CarMa transfer function in the infinite frequency limit. This latter particular case is also called *D-matrix*, since it is calculated from the only surviving part of Eq.64 after the $\omega \to \infty$ limit. All these matrices are normalized to their maximum value and they will be used, as specified in Section 6.2, to recombine the current reference pattern fed to active coils.

6.2 THE MODEL

Modeling tools have been fundamental for developing and testing decoupling strategies. The dynamic simulator will be here introduced along with the vacuum validation for one particular case.

6.2.1 *Dynamic Simulation Tool-Set*

A dynamic simulator has been developed as a Matlab®Simulink application to allow the simulation of a full control loop and the test of the optimization techniques described in the present paper. The core of this flight simulator is a state-space representation of the system (Plant) given by the CarMa code, which is integrated with a complete representation of the digital control system. This allows for a realistic description of the passive and active structures with the effects of 3D geometry on plasma dynamics. The active system can be simulated at its full potential

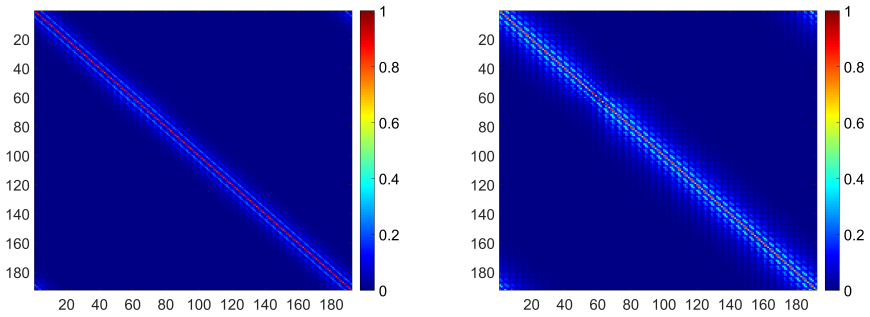

(a)

(b)

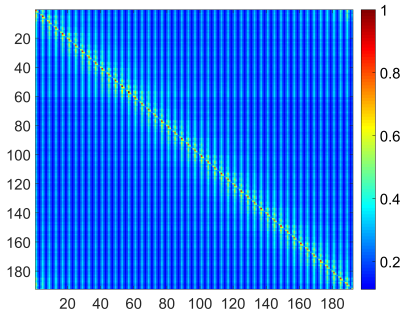

(c)

Figure 17: (a) Experimental decoupling matrix calculated for $\omega = 0$, i.e. step-like request. (b) Experimental decoupling matrix calculated for $\omega = 10$Hz. (c) CarMa derived decoupling matrix representing the infinite frequency limit. The color scales represent the actuator-sensor couplings, all matrices are normalized to their maximum value. Saddle sensor and active coil numbers are given on the y-axis and x-axis respectively.

or downgraded to a reduced number of coils with virtually any geometry. The CarMa code itself is the result of coupling a 3D eddy current problem integral solution (given by the CARIDDI code) with a 2D linearized MHD solution, which results from the MARS-F code[40]. Instantaneous plasma response to a given perturbation is calculated on a coupling surface (S) and used to evaluate the effect of the 3D structures on the plasma. The currents induced by the plasma in these structures are computed using an equivalent surface current distribution on S, such that it generates the same magnetic field as the plasma just outside S. The model used for the dynamic simulator in particular, includes a fully 3D description of the resistive copper shell surrounding the vacuum vessel (3 mm thick with $\tau_V = 50$ ms vertical field penetration time) as well as including the active system components. The copper shell itself is the fundamental component in plasma stability applications, since it slows down to its characteristic penetration time some of the fastest growing MHD instabilities (i.e. ideal kinks),thus allowing the possibility of feedback control[34]. The flexibility of the RFX-mod digital controller allows to apply different control strategies, the most common one being the CMC outlined in Section 2.5. This method allows independent action each harmonic component of the discrete Fourier transform of the radial magnetic field. A real-time algorithm is therefore applied to remove the aliasing error from the magnetic field harmonic component measurement, caused by high order sidebands produced by the 4×48 discrete grid of saddle sensors. A block scheme of the system described above is given in Figure 18, both for the open-loop case (Figure 18a, in which the sidebands cleaning is not applied) and closed-loop (Figure 18b). An exploded diagram of the control system block can be seen in Figure 18c, in which the application of the decoupling based on static matrices is represented, as described in Section 6.1. The main part of the Plant block is the state-space representation of the CarMa model, which is implicitly preceded by the saddle coil current controller. Finally a state-space filter has been added to the Plant block, also in series with the main model, in order to mimic the effect of the stainless steel vacuum vessel, with a 5 ms time constant.

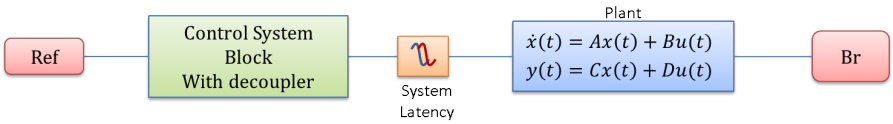

(a)

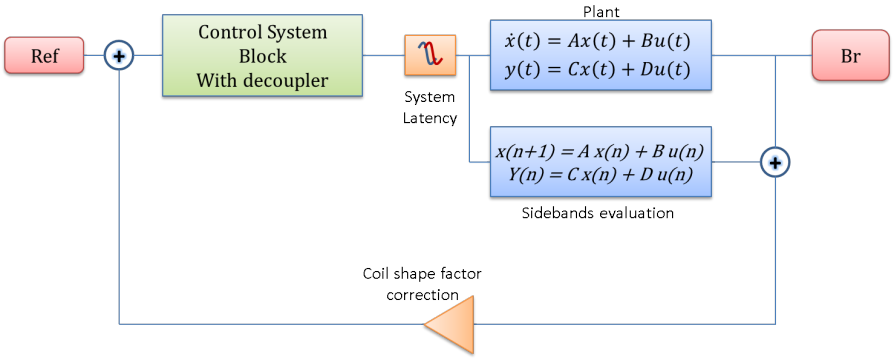

(b)

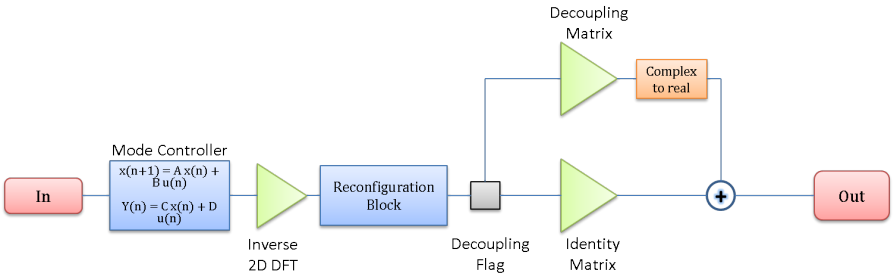

(c)

Figure 18: (a) Open loop diagram. (b) Closed loop diagram with clean-mode-control. (c) Exploded control system block with decoupler.

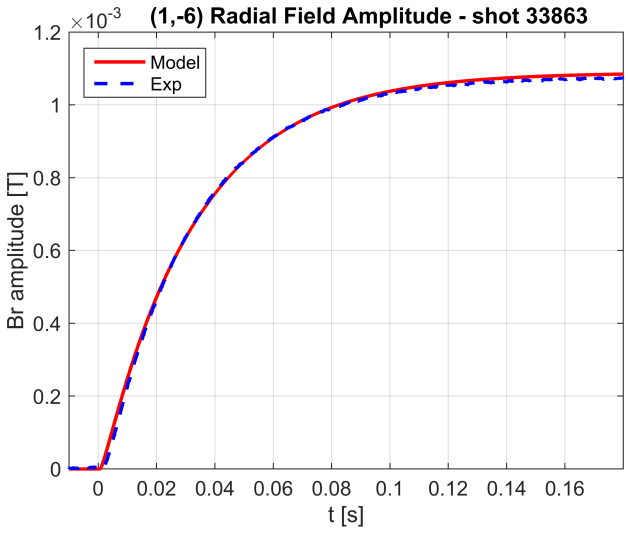

(a)

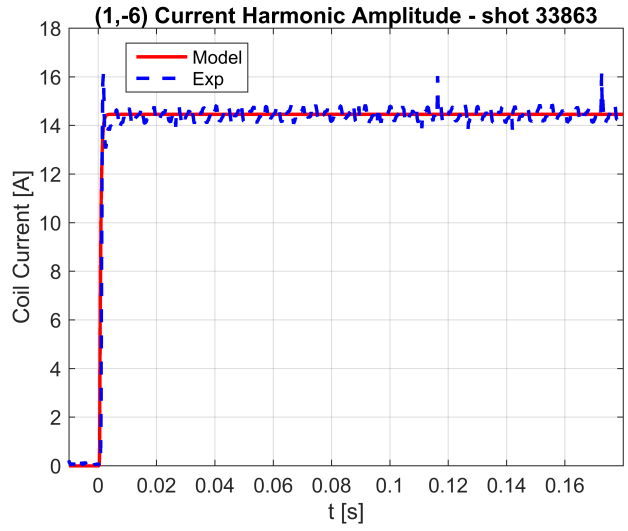

(b)

Figure 19: Experimental and model time evolution of m=1, n=-6 harmonic component of the radial field (raw) (a) and saddle coil currents (b). Simulation and data from shot 33863.

6.2.2 *Validation of the Vacuum Model*

The main goal to be achieved with the optimization procedures described here is the correct assessment of the system external action on a given plasma. In order to do so, all the experimental sessions dedicated to the evaluation of mutual couplings have been carried out in vacuum. The same has been done for the modeling activity, a vacuum version of the CarMa model has been used and benchmarked against experimental data in terms of harmonic content of the output magnetic field. The very good agreement of simulated B field amplitude and current with experimental data can be seen in Figure 19. During this open-loop vacuum shot the active system has been requested a particular perturbation with m=1 and n=-6 mode numbers. The same shot can be reproduced as a dynamic simulation. The amplitude of the $(1,-6)$ component of the output field is shown for both cases in Figure 19a, where the *raw* data is used, indicating that the sideband cleaning procedure has not been applied for the particular case. Figure 19b shows the current $(1,-6)$ harmonic component, confirming that the developed simulation tools can successfully represent the real vacuum experimental setup. Figure 19 is not only showing the general agreement between simulation and measurements but also the capability of the software tools of reproducing a very peculiar configuration. Specifically, during shot 33863 a reduced coil array has been implemented, with the $(1,-6)$ magnetic perturbation generated by only 12 non-equispaced active coils along the outermost toroidal array. This leaves a characteristic pattern in the produced sidebands which can be appreciated in Figure 20. The amplitude of each harmonic is given in the bar-plot, normalized to the desired $(1,-6)$, at a given time instant of the flat-top phase. It is worth mentioning that the harmonic pattern is given by the peculiar periodicity of the active array and it is correctly reproduced by the open-loop simulation. With an evenly distributed set of coils the expected toroidal sidebands would have followed the relationship: $n' = n_0 \pm kN$. Where n_0 is the desired harmonic (here $n_0 = -6$), N the number of coils (here $N = 12$) and k an arbitrary integer. It follows that for twelve equispaced coils the pattern would be $n' = +6, \pm 18$. The coil geometry in Figure 20 however, has a characteristic pattern that resembles that of two groups of six coils each. These are equispaced intra-group but not inter-group. The effect of this

superposition is that the sidebands of an N = 6 configuration are produced (i. e.as if six coils where used).

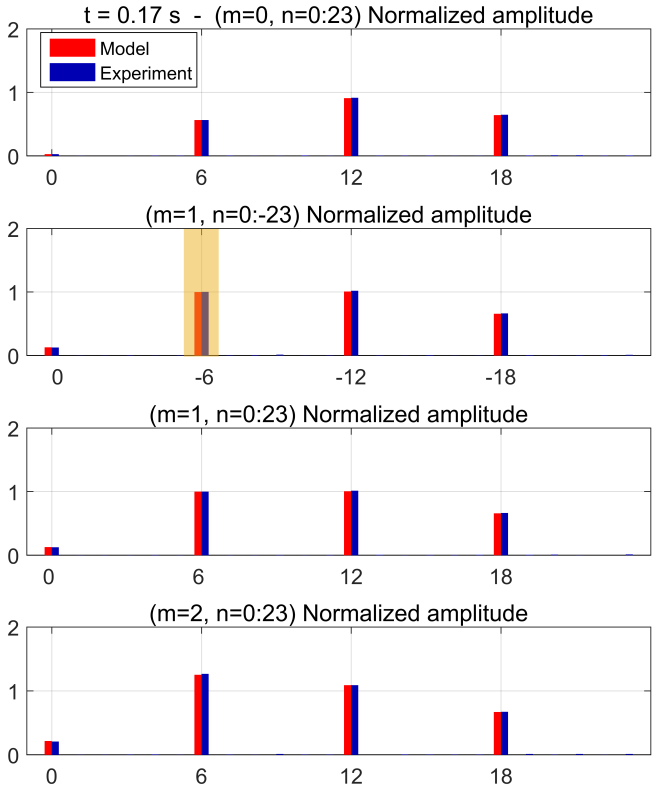

Figure 20: Comparison between model and experiment relative harmonic content of the radial magnetic field (raw) in shot 33863. Amplitudes taken in steady phase at t=0.17 s

6.3 OPEN LOOP OPERATION WITH DECOUPLING MATRICES

The first set of matrices generated from both experimental measurements (as described in Section 6.1) and the CarMa code (Section 6.2) has been applied for the open-loop generation of magnetic field perturbations of varying amplitude and phase. The Total Harmonic Distortion (THD) of the output fields has been used in order to evaluate the effectiveness in spurious harmonics reduction.

Total Harmonic Distortion

$$\mathrm{THD} = \frac{\sum_i B_i^2 - B_{target}^2}{B_{target}^2} \tag{65}$$

where the index i runs on all the harmonic components of the field signal. An example of this total harmonic distortion analyses is reported in Figure 21, in which two different decoupling strategies have been used for the generation of a step-like perturbation. The red dashed line shows the reduction of spurious harmonic content when the specific model-derived matrix is used, with respect to the blue solid line (identity matrix, i.e. no decoupling applied). The green dotted line shows a degradation of the harmonic content instead, this is due to the peculiar applied matrix, obtained through an infinite frequency limit from Eq.64. Because of this limit, the so-called *D matrix* does not work well for a step-like request during the steady phase. On the other hand its effect can be appreciated during the fast transient phase, as in Figure 21b, when the B field is increasing rapidly and the infinite frequency limit holds, during the first 30 ms in particular. The smaller harmonic distortion obtained

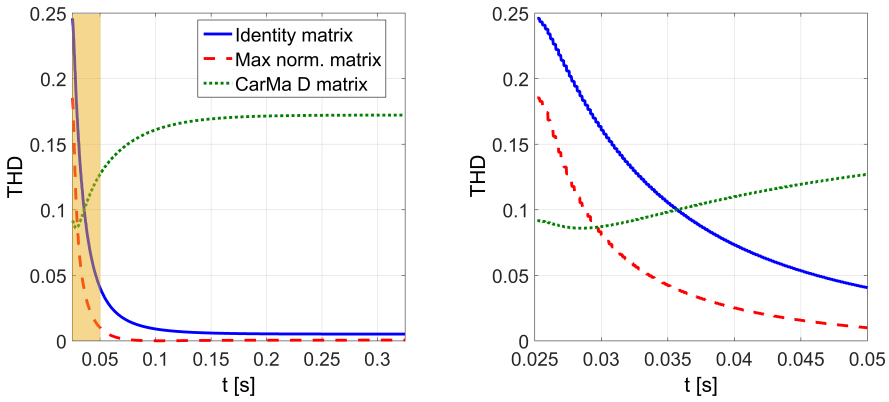

(a) (b)

Figure 21: (a) Total harmonic distortion from simulations with D matrix, $\omega = 0$ Hz matrix and identity matrix. (b) Zoom of the first 50 ms of the transient phase in which the effect of the D matrix, i.e. infinite frequency limit, can be appreciated. Amplitudes are normalized to the $(1, -6)$ component.

with a given decoupling matrix is reflected in the amplitude of the B field spurious harmonics, this can be appreciated for two different cases in Figure 22. For the step-like magnetic perturbation (Figure 22a) a simple decoupling matrix helps in reducing the amplitude of the $(m = 0, n = 6)$ component, the very same result has been obtained in dedicated vacuum experiments[78]. Another matrix has been used with the dynamic simulator for a 10 Hz perturbation, resulting in a reduced spuri-

ous harmonics relative content (Figure 22b). It should be noted that the matrices applied in the aforementioned reference cases (represented respectively in Figure 17a and 17b) are providing the best correction during the steady phase of the perturbation, while during the fast transients the infinite frequency limit holds as previously discussed. It is also worth noting that Figure 17b shows the amplitude oscillating around its mean value at approximately 20 Hz. A complete explanation of this behavior is beyond the subject of the present Chapter, it is ultimately caused by the spatial variance of the system (e.g. toroidal geometry, gaps, local features etc.) and can be explained with the Unified Signal Theory[79] formalism.

6.4 CLOSED LOOP DECOUPLING APPLICATION AND MISSING COIL COMPENSATION

Once the exact behavior of the active system has been assessed by generating open-loop perturbations, the same can be done within the feedback loop. While the results to be expected are still related to reducing the harmonic pollution during steady phases, attention should also be paid to the possible gain changes introduced by recombining the reference current distribution. The static matrix shown in Figure 17a has been included in the feedback loop during dedicated experiments, allowing the verification of expected effects and validation of the modeling results. Figure 23 shows the amplitude of a $(m = 1, n = -6)$ perturbation together with its poloidal sidebands. A reduction of the $m = 0$ component is found with the non-diagonal decoupling matrix. Furthermore, since the amplitude of the requested $n = -6$ component is the same in both cases, the gain substantial invariance with application of this particular decoupling matrix can be acknowledged. The importance of this last matter lies in the fact that no change in the gain matrix has to be made if decoupling has to be switched on or off during experimental campaigns. The idea of using a static matrix to recombine the active system input current distribution has also been applied to a set of problems not strictly related to decoupling sensors and actuators. Given the possibility of implementing various active coil geometries, as mentioned in Section 6.2.2, a systematic study has been carried out to investigate the effect of one or more faulted actuators on the produced magnetic fields. This has led to the development of a set of matrices that while still aiming at the improvement

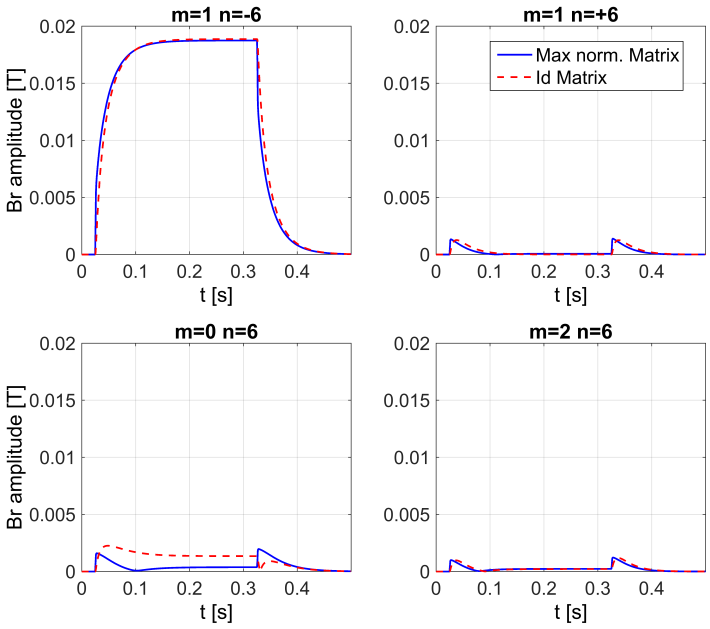

(a)

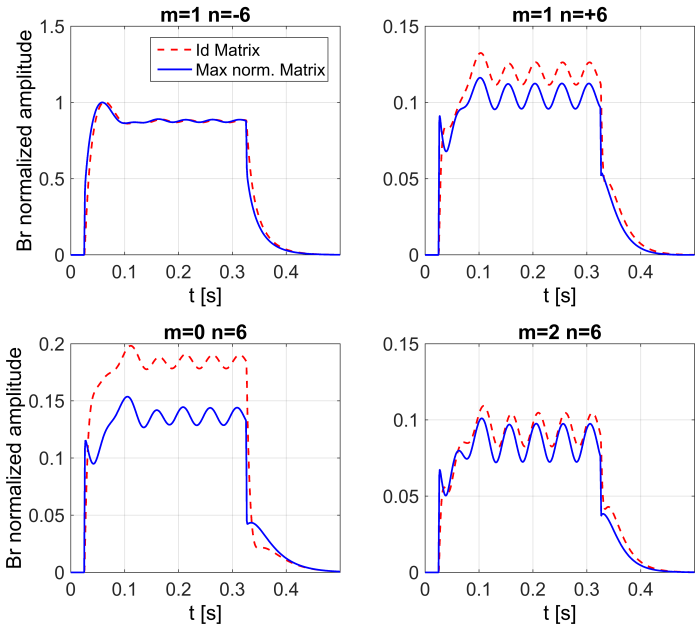

(b)

Figure 22: Poloidal harmonics produced for $(1, -6)$ reference. (a) Step-like perturbation with no decoupling (dashed red) and with CarMa $\omega = 0$ Hz matrix applied (solid blue). (b) For a 10 Hz perturbation the dedicated decoupler is compared with the identity matrix case. As expected the decoupling effect can be appreciated in the reduction of the $(0, 6)$ and $(1, +6)$ amplitudes, in this case a normalization to the maximum of the requested harmonic has been applied to highlight the effect.

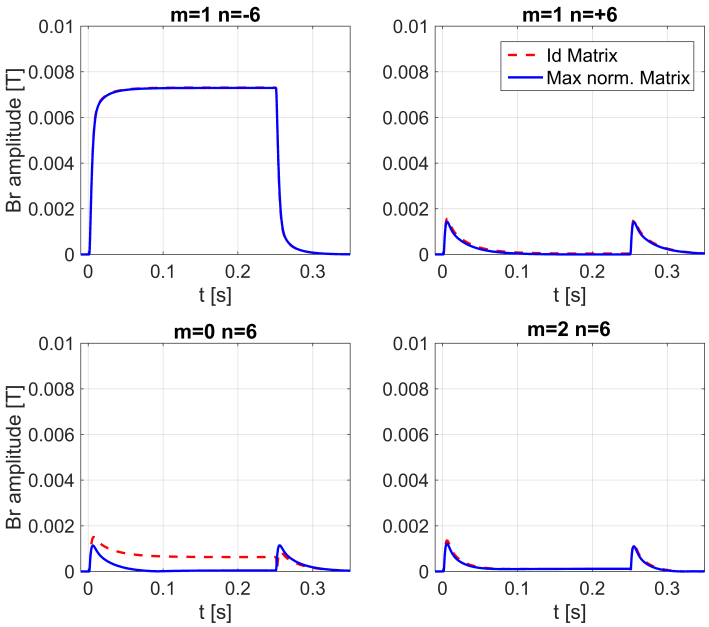

Figure 23: Step-like $(m = 1, n = -6)$ perturbation generated in a closed-loop with purely proportional gain on the requested harmonic only. Comparison between shots 27294 and 27295.

of the harmonic content, are specifically designed for a system with sparse missing coils. The procedure, that can be found in [80] and in Chapter 7 of the present thesis, has been proven as a simple and fast option for faulted coil compensation that allows a local reconstruction of the magnetic field and reduction of spurious harmonics.

6.5 CONCLUSIONS

This part of the work has summarized many efforts made for the complete characterization of the RFX-mod active system in terms of output magnetic field, in particular the actuator-sensor decoupling problem has been considered. Starting from the first experimental measurements the development of simple, real-time applicable strategies to obtain almost monochromatic fields has been described. While the $(m = 1, n = -6)$ perturbation has been mainly shown in the previous sections, the same can be done for any desired B harmonic. The importance of a fast, reliable and extensively benchmarked modeling tool has to be highlighted. Each of the proposed decoupling matrices, as well as the whole missing coil compensation strategy,

has been developed with full dynamic simulations before testing in dedicated experiments or implemented in plasma shots. The effects of actuator-sensor decoupling has thus been investigated and represented mainly by the reduction of spurious harmonics when a particular one is requested. With the introduction of the total harmonic distortion the two limiting cases, $\omega = 0$ and $\omega \to \infty$, have been identified. The high frequency behavior during transient phases has been assessed with the implementation of the so-called $D - matrix$ while two examples have been reported to show the $m = 0$ amplitude reduction when a specific decoupler is used. Finally, the closed-loop application has been reported with proof of the expected effect on the B components and of the negligible influence of the current modification on the applied gains. The concept of sparse missing coils compensation using a static matrix has been briefly mentioned.

7

MISSING COIL COMPENSATION ON RFX-MOD

"All human knowledge begins with intuitions, proceeds from thence to concepts, and ends with ideas."

— Immanuel Kant, Critique of Pure Reason

[1]In many devices aiming at magnetic confinement of fusion relevant plasmas, feedback control of MHD instabilities by means of active coils is nowadays mandatory to ensure the robustness of high performance operational scenarios. As described in Section 5.1, actuators in this system are 192 active saddle coils entirely covering the plasma outer surface, while more than 600 magnetic sensors are included in the control loop, providing the operator with a challenging coupling situation. The RFX-mod active saddle coils are mounted on a stainless steel support structure to cover the whole surface of the torus and organized into a 4×48 (poloidal $\times$ toroidal) array. The same geometry of these coils, which gives the uniform magnetic boundary, is reproduced on the outer side of the vacuum vessel where 192 saddle sensors measure the radial component of the magnetic field. Saddle coils will be numbered with two indices (i, j), the former for poloidal and the latter for toroidal positions. This hardware configuration allows the implementation of highly flexible real time control strategies, action is carried out in the bi-dimensional Fourier space characterized by the poloidal (m) and toroidal (n) mode numbers. The coupling of the actuator-sensor system is a frequency dependent problem, intrinsically 3D when considering the effect of non-uniformities of the active RFX-mod magnetic boundary such as the implementation of reconfigured arrays [36] or the fault of one or more active coils. A decoupler should be in principle frequency dependent and thus realized as a convolution integral of the input signal and a time dependent function, the system impulse response. Given the difficulty of implementing a frequency and time dependent decoupler in real-time operation, the choice of using a static matrix is by far more feasible. These matrices are cal-

1 Part of the content of this Chapter has been published in: *Pigatto, L., et al. "Optimal strategies for real-time sparse actuator compensation in RFX-mod MHD control operations." Fusion Engineering and Design 96 (2015): 690-693.*

culated from actuator-sensor mutual inductances at a given frequency and have been successfully applied in both experiments and simulations [77], as also reported in Chapter 6. The aim of the this part of the work is to study the local effect of a non-uniform boundary on the magnetic field produced by the active coils, introducing possible compensation methods which take the actuator-sensor coupling as a starting point.

A numerical plant model obtained from the CarMa code [81] is used for dynamic simulations in which different experimental setups and decoupling strategies can be tested[82][63]. This model is described in Section 7.1. The baseline situation in RFX-mod is documented, where the Identity matrix is chosen to represent the simplest case of mutual coupling matrix. The problem of missing or broken actuators is introduced and tackled with dedicated compensation strategies. A detailed description is given for a possible compensation concept which can be applied in real-time operation thanks to its implementation strategy, yielding very promising results in terms of local field reconstruction, as reported in Section 7.2. As it will become clear in the following, the problem of current request from actuators is not negligible with compensation strategies that will be tested. A study of these requests has been carried out and is reported in Section 7.3 along with modeling and experimental data as documentation of the local effect of missing actuators on magnetic field geometry and localized first wall heating. A statistical study is presented in order to evaluate how coil compensation affects this latter issue.

7.1 MODEL

The same dynamic simulator introduced in Section 6.2 has been used for the development and testing of the actuator compensation, given the strong relationship with the technique here described with the one outlined in Chapter 6. The open-loop system is represented as a block diagram in Figure 24. The compensation block represents the matrix multiplication that is used to redistribute the 192 current references on the saddle coils in order to take into account all the actuator-sensor couplings and geometrical characteristics. Such a matrix can be obtained by inversion of either an experimentally measured mutual inductance matrix or the plant transfer function. The

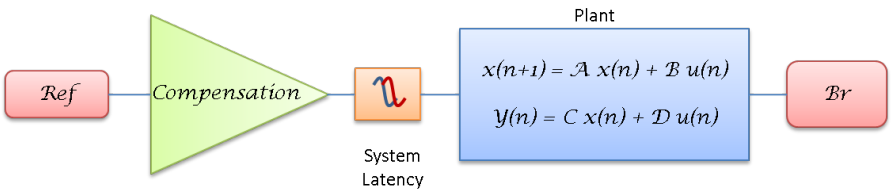

Figure 24: Block diagram of open-loop dynamic simulator

latter can be obtained from the state-space representation matrices A, B, C, D:

$$K = C(i\omega\mathbb{I} - A)^{-1}B + D \tag{66}$$

where ω is the frequency and $\mathbb{I}$ the identity matrix. The application of these matrices has already been seen useful for the reduction of vacuum field harmonic distortion [77][78]. The two limiting cases of zero and infinite frequency in particular can be taken as a starting point for the application of a similar strategy to a situation in which one or more actuators are either broken or disabled. The basic idea is to generate, from the initial reference currents I_r, a new current distribution $\hat{I}_r$ that allows the reconstruction of the desired field pattern B_r

$$B_r = S^{-1}KI_r = S^{-1}\hat{K}\hat{I}_r \tag{67}$$

where S represents the area of saddle sensors, K is calculated from Eq. 66 and $\hat{K}$ is a new matrix in which the missing actuators are accounted for. The new current distribution must satisfy:

$$\hat{I}_r = \hat{K}^{-1}KI_r \tag{68}$$

The product $\hat{K}^{-1}K$ is used as *compensation* block in the diagram representation in Figure 24. The new matrix $\hat{K}$ can be calculated starting from either experimentally measured actuator-sensor couplings [78] or by taking the model transfer function K. The elements corresponding to missing actuators are then removed so to obtain a matrix with $N - j$ non-zero columns, where N is the total number of actuators and j are the missing ones. A *pseudo-inverse* is finally applied to obtain $\hat{K}^{-1}$. An example of the resulting matrix is given in Figure 25, where the $\omega = 0$ case is represented in particular. The non-zero columns corresponding to missing actuators should be noted together with their null value on the diagonal, this means that the coil itself does not contribute to the locally measured field. Instead, because of the non-zero non-diagonal elements, the field initially

requested to missing coils will be compensated by the working ones with the matrix product in Eq. 68.

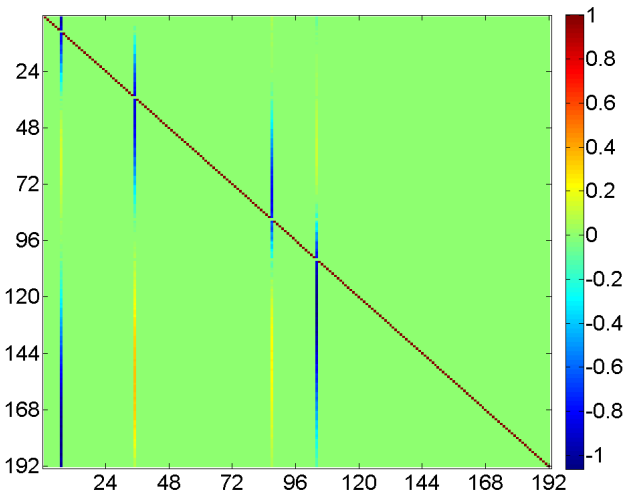

Figure 25: $\hat{K}^{-1}K$ matrix for the case in which actuators (3,02)(3,09)(3,22) and (4,26) have been disabled. Rows represent actuators and columns saddle sensors, each point in the matrix is a coefficient for current redistribution.

7.2 MAGNETIC FIELD RECONSTRUCTION RESULTS

The full open-loop model of the system has been validated by comparison with experimental values. Various poloidal positions have been considered for comparison, an example is given for the $i = 16$ array in Figure 26. Ad-hoc calibration of the specific shot has been introduced, consisting in a rescaling of the simulated current reference to match the average of the measured one. The resulting agreement with experimental values can be considered adequate for the purpose of evaluating the effect of a missing coil on local fields. The effect of a missing coil in the control system can be appreciated in Figure 27 (dashed line). The sensor corresponding to position (3,09) measures the field produced by the neighboring coils only, while the left and right first neighbors see an increased radial field. This local error field can be corrected with the introduction of the strategy described above, leading to very good mitigation of the missing coil effect. As can be noted from the graphical representation of the implemented matrix in Figure 25, all the other active coils are involved in compensating the missing ones, making the problem of assigning proper weights non-

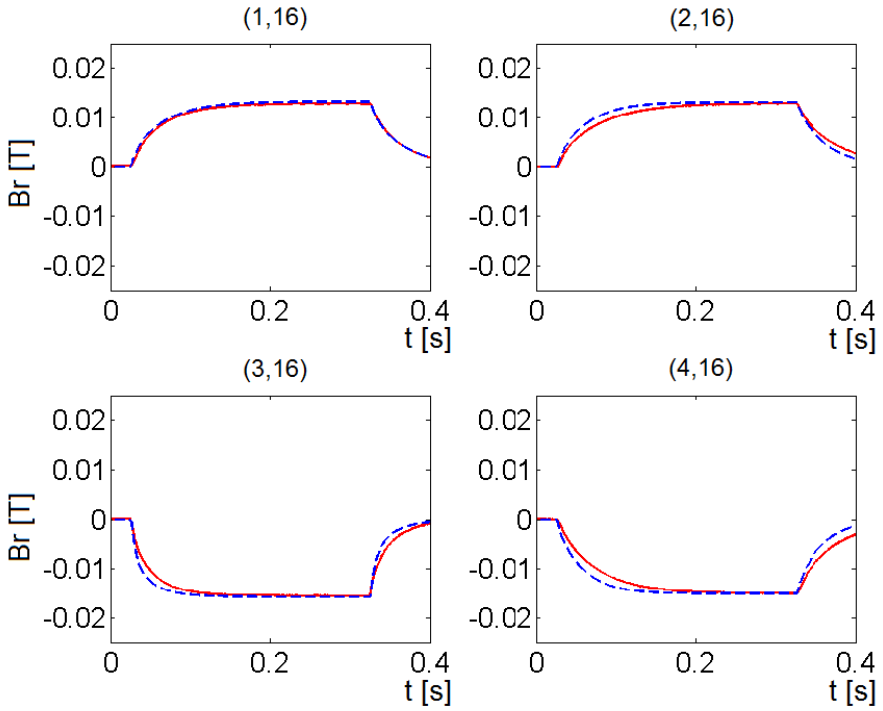

Figure 26: Comparison between measured radial field (solid line) and calculated radial field (dashed line) from input current model for the 16th poloidal array.

negligible. The pseudo-inverse method described in Section 7.1 allows for the coils closer to the missing one to have a major role in the task, thus avoiding non-realistic demands to further distant and weakly coupled actuators. Interestingly enough, the applied actuator compensation strategy does not drastically affect the final Fourier spectrum of the produced magnetic field. The effect of compensation on the harmonic content can be appreciated in Figure 28 where a comparison is given in terms of Fourier harmonic amplitudes normalized to the ideal all-active-actuators case. The most important information that can be extracted from Figure 28 is that the compensation method does not dramatically alter the desired harmonic content with respect to the ideal situation, it can instead deliver a slight improvement in terms of sideband amplitude reduction with respect to the not-compensated corresponding case. The price to pay for the missing actuators though lies in the current redistribution that the strategy necessarily implies. Rescaling coil current references could, according to the case, lead to reaching machine hardware and software operational limits. It must thus be taken into account that the rescaled currents should still be compatible with such limits. In order to quantify the effect

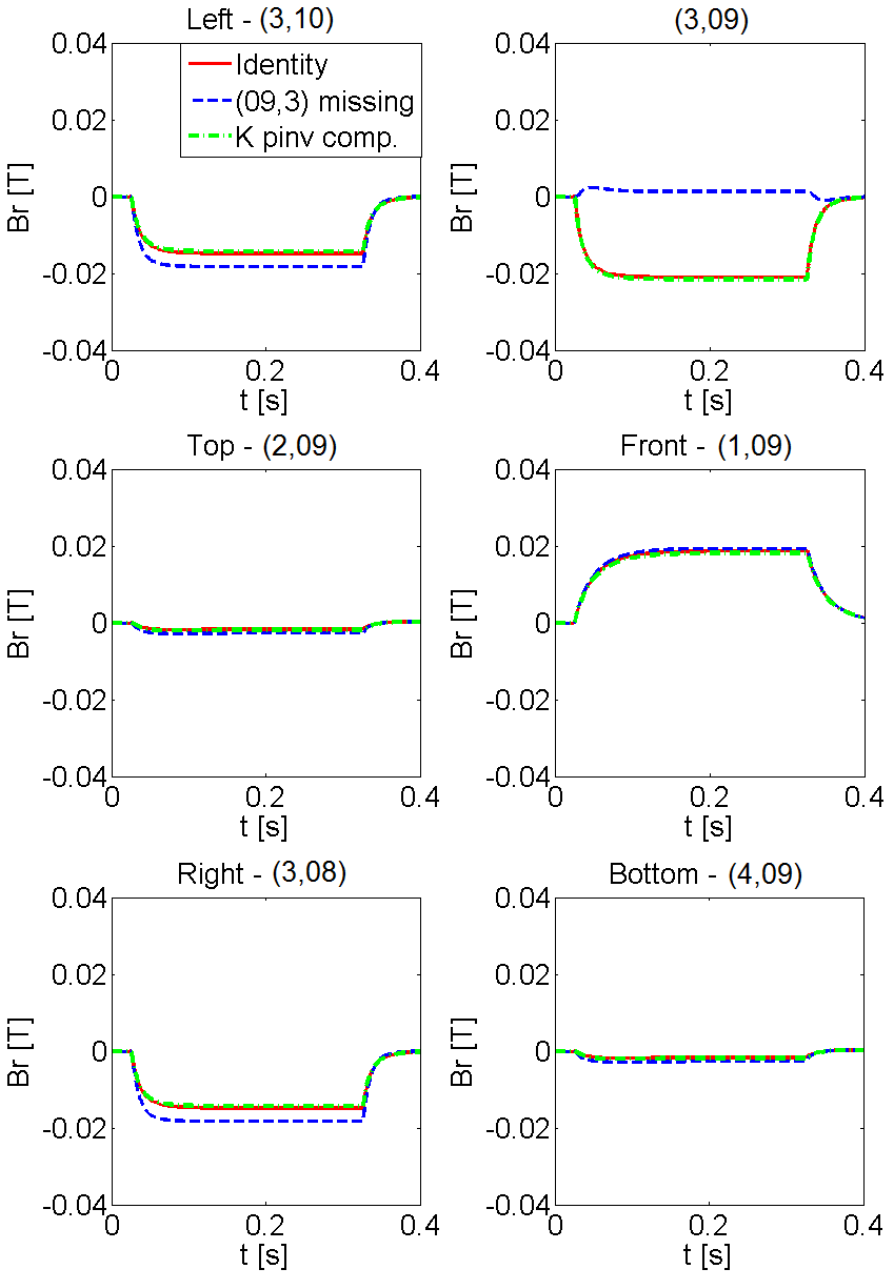

Figure 27: Effect of (3,09) missing coil compensation strategy during the generation of a (1,-6) step-like vacuum perturbation. Simulated radial fields from surrounding sensors are represented for three situations: all coils working (red solid), one inactive coil without compensation (blue dashes), local pseudo-inverse compensation (green dashes).

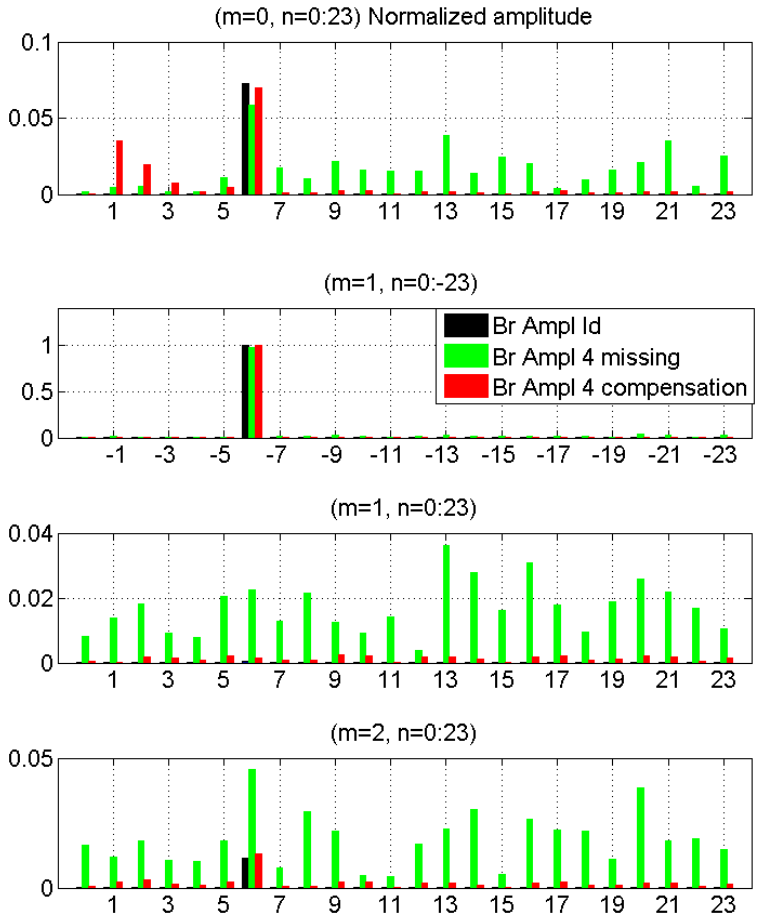

Figure 28: Fourier harmonic amplitudes, at t=0.2s, compared between the applied compensation strategies and normalized to the desired n=-6 amplitude in the ideal case without missing coils. Different scales on the Y-axis are used to enhance the visual effect of the comparison.

of the compensation method on the current fed to each coil the following quantity has been evaluated:

$$\frac{|\,\hat{I}_r - I_r\,|}{I_{max}} \cdot 100 \tag{69}$$

where $\hat{I}_r$ is the new current distribution, I_r the original one and I_{max} the maximum regime current. The result of this operation has shown that the current required in each coil in order to compensate for a missing one is about 100% of the original current. This can be explained given the linearity of the system: if the absence of a current of magnitude I is to be compensated, other coils will see their reference increase of approximately $-I$. The compensation strategy described in Section 7.1 and represented by the matrix in Figure 25 has been recently applied to dedicated experiments. Figure 29, which represents the most significant result from the techniques illustrated so far, shows the compensation results for coils (3,02) (3,09) (3,22) and (4,26) compared to a simulation with all coils active and to the case in which they are simply disabled. It is worth noting that the local magnetic field under each missing coil (dashed blue line) has opposite sign if compared to what a working coil should have produced (solid red line). This behavior is being corrected by the applied compensation strategy, thus recovering the correct sign and reducing the localized error field (dotted green line). Given the applicability of the required current distribution, this technique allows to reach a satisfying compensation of the missing coils both in terms of harmonic content and local radial field.

7.3 FIRST WALL TEMPERATURES IN COMPENSTED SHOTS

As we have seen so far, the flexibility of the RFX-mod control system can be exploited to model the fault of one or more coils. Evaluating the effects on localized error fields and the importance of a compensation strategy for the case in which one or more coils are actually broken. One missing saddle coil in any position along the torus can be thought, if no current flows in it, as a hole in the plasma magnetic boundary and the corresponding saddle sensor would only measure the effect of the surrounding working coils. For the purpose of visualizing this concept, one of the coils has been disabled for a single vacuum discharge with an $n = -6, m = 1$ external perturbation requested with $f = 0$Hz. The result can be seen in Fig.30. When

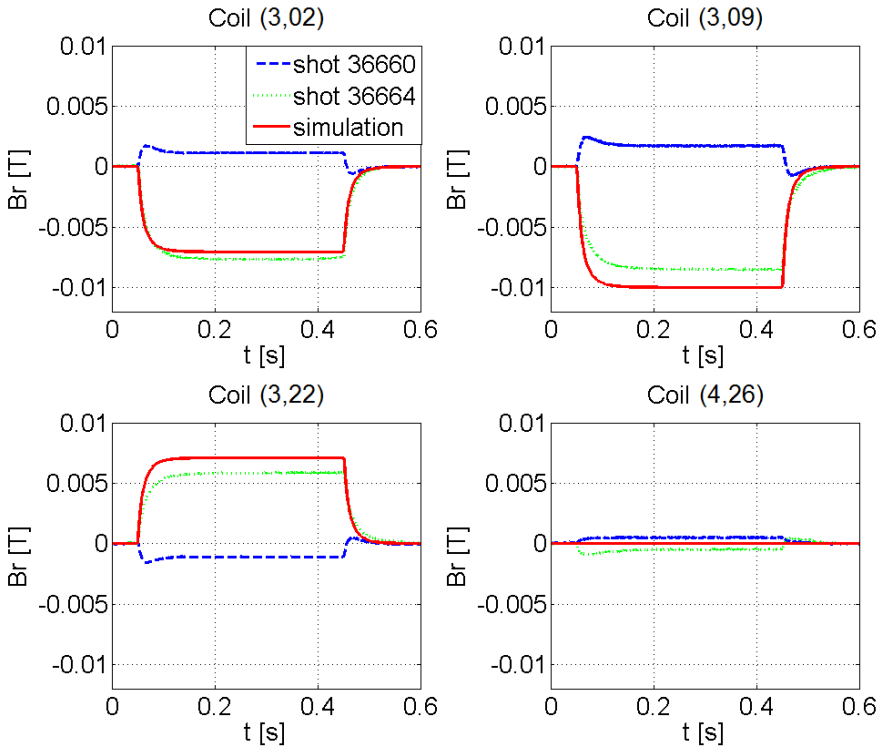

Figure 29: Shot 36660 (dashed blue) with coils (3,02) (3,09) (3,22) and (4,26) disabled compared to shot 36664 (green dots) in which the compensation strategy is applied. The solid line (red) represents a reference simulation in which all coils are correctly working. In each case the system produces an m=1, n=-6 perturbation.

any actuator is for some reason disabled, the local magnetic field given by the surrounding coils will be significantly different from the target one. With the main contribution provided by the opposite saddle coils, the local field will not only be smaller than the desired one but it will also change sign. This behavior becomes a phase difference in case of an oscillating request, as shown in Fig.31 the field underlying coil $(2, 38)$ has opposite phase with respect to the target. The presence of these

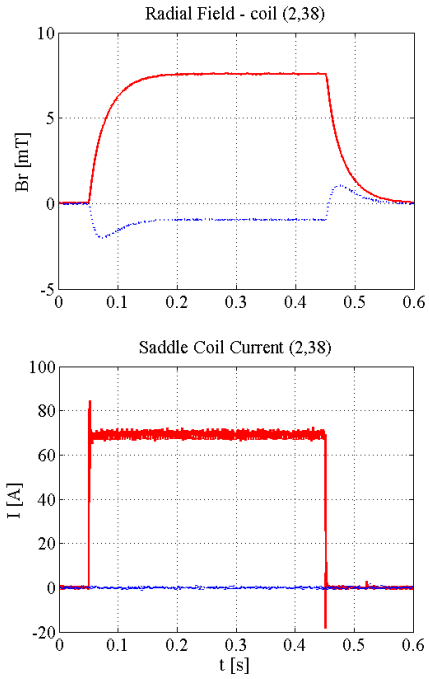

Figure 30: Disabled coil example, radial field (upper) and current (bottom) are shown for the case of a correctly working saddle coil (solid red) and for a disabled coil (dotted blue). The coil in toroidal position 38 along the outboard array has been manually disabled for this example.

defects in the magnetic field is reflected during operation in a degradation of plasma performance, mostly due to mode locking and first wall heating issues. The hypothesis behind this work in particular, is that if it were possible to mitigate the effects of missing saddle coils, this would leave a trace in the first wall heating pattern. The flexibility of the RFX-mod control system is helpful for the idea of compensation, allowing maneuvering space for each single coil to be tuned according to the designed task: reproducing the magnetic field that was created by the complete system and thus compensating for missing coils. Three experimental runs have been carried out with the specific

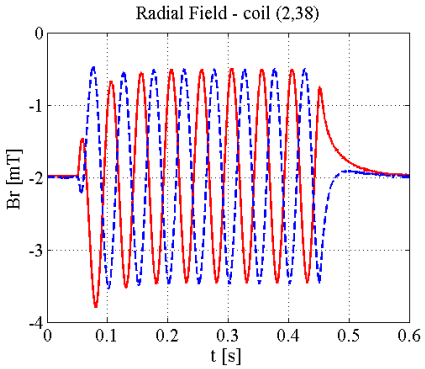

Figure 31: Radial field measured under disabled coil (2,38) for a 20 Hz perturbation requested. The target field is represented in solid red, the measured field by the dashed blue line.

target of evaluating the effect of coil compensation on the localized wall heating pattern. On the side of diagnostics, four sets of thermal sensors can be used [83] [84]. Thermocouples however are not uniformly covering the toroidal surface, the most numerous set has therefore been chosen for the future analyses. This set gives a good coverage of the first 150° while yielding a sparser but nevertheless sufficient sampling of the rest of the torus. Experiments have been performed with plasma current (I_p) ranging from 0.9 MA to 1.65 MA. First objective of the campaign has been the creation of a shot database large enough to evaluate the effects of compensation at different I_p values. A good database has been prepared, in order to evaluate first wall heating, by alternating standard RFP shots with varying I_p and shots in which the compensation strategy was introduced.

7.3.1 *Currents with Actuator Compensation*

While the effect of the compensation strategy on localized error fields has already been verified in both simulations and dedicated experiments, the problems of localized wall heating and operational limits are still open. As a first step the operational limit issue has been tackled. Since the compensation strategy implies current reference recombination, the risk of feeding one or more coils with currents above the allowed limits has been foreseen, with the possibility of running into saturations. Fortunately these saturations were seen to be comparable both with and without the compensation matrix. In order to fully assess the effect of compensation on the current distribution, the $I^2(t)$ signals have been considered (proportional to the total power)

for each active coil with/without compensation. All the available shots have been sorted into two populations depending on whether the compensation matrix was applied or not. For each active coil the maximum $I^2(t)$ is considered and normalized to the sum of maximums over all the coils, these values are then summed over the shots for each population. The following quantity has been implemented:

$$\Sigma_I = \sum_{\text{shots}} \left(\frac{I^2(t)_{max,n}}{I^2(t)_{tot,n}} \right) \tag{70}$$

Where the n index stands for each coil along the four toroidal arrays. Even though the data manipulation is complex, it allows to see whether or not the introduction of compensation significantly modifies the power required by each coil with respect to the total power in each shot. The result shown in Fig.32 is enough to conclude that the compensation strategy, although changing the current distribution, has no dramatic effect on the power requirements. It is instead improving the situation in some areas such as the first 12 poloidal rings. Compensation can thus be safely implemented with plasma current up to 1.5 MA.

7.3.2 *Temperature Analysis*

Main objective of the experimental campaign is assessing the capabilities and testing the effects of the compensation strategy developed for four broken actuators in the RFX-mod saddle coil array. This strategy, described in the previous section, is based on a recombination of the current reference that takes into account the missing coils. Working actuators are asked to do part of the job of the broken ones, thus reducing localized error fields and possibly improving the uniformity of the magnetic boundary. To identify the possible relationship between missing coil compensation and plasma-wall interaction, the available thermocouple sets have been used. With these sensors being located on the external surface of the vacuum vessel, a statistical approach has been chosen to overcome the thermal inertial effects in the evaluation of the localized wall heating. During the experimental campaign the compensation strategy, developed for the four missing coils in positions (3,02) (3,09) (3,22) and (4,26), has been applied alternately to the standard *identity matrix*. A database of 57 useful shots is now available for data analysis, with plasma current ranging from 0.9 MA

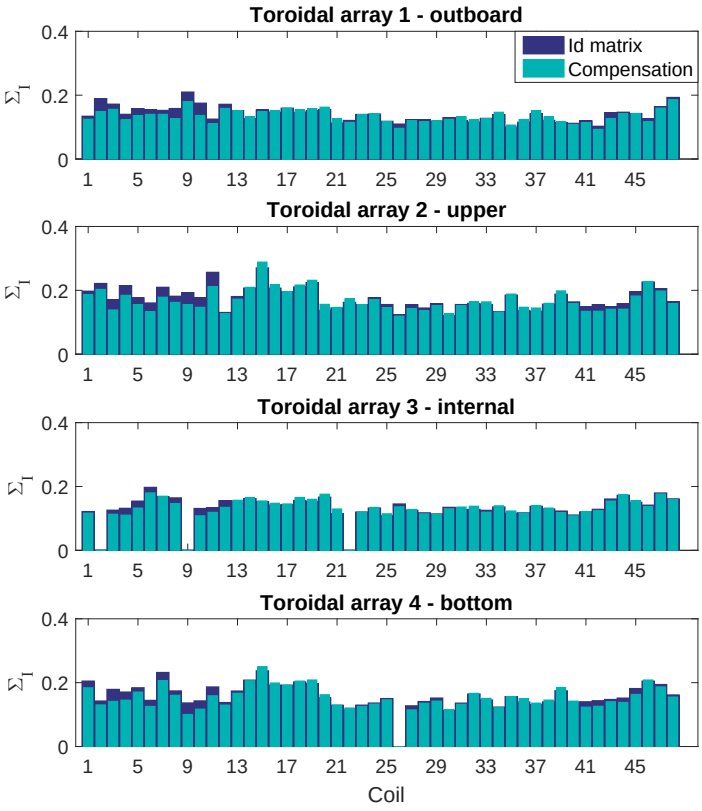

Figure 32: Normalized $I^2(t)$ for each saddle coil. Along the four toroidal arrays, for each coil (index n) the maximum value is calculated and normalized to the total $I^2(t)$ fo the same coil. The four broken coils are visible as no current is flowing through them.

up to 1.65 MA. Both Matlab®and Python environments have been used for the purpose. Python routines in particular have been developed to run most of the analyses, allowing for fast data-loading and database cross-checking.

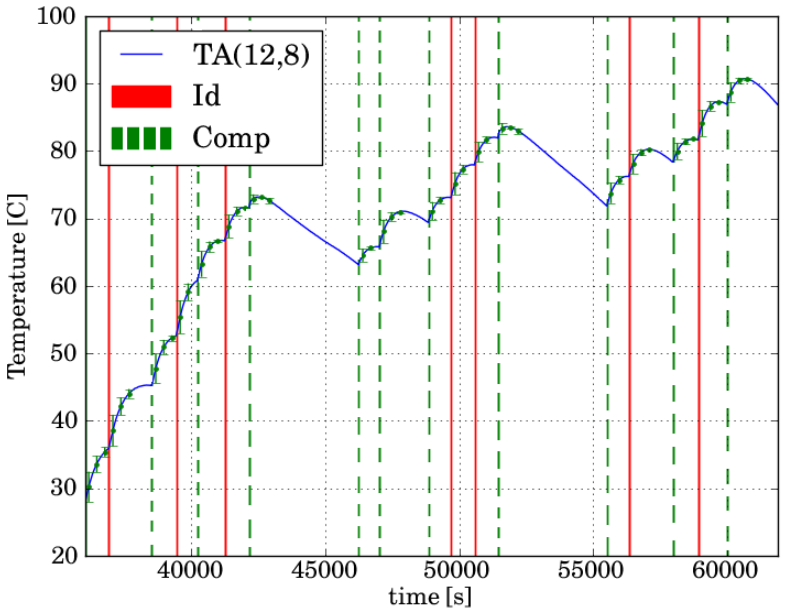

Figure 33: Figure corresponding to run 2280 in which each shot is marked on the sensor signal. Compensated and not-compensated can be distinguished. Time is in seconds from midnight.

All the available shots have been analyzed with a set of dedicated tools to extrapolate statistically useful information. Two samples have been considered, containing compensated and non-compensated shots, the identification of which has been used to split thermocouples' signal as reported in Fig.33. Each shot has been completely characterized in terms of starting and ending time of each phase from initialization. A three dimensional temperature map (poloidal, toroidal directions and time) is therefore obtained for the chosen thermocouple set from which the general wall heating pattern during a high current RFX-mod run can be appreciated. Fig.34 shows part of the information contained in the aforementioned map, the poloidal angle has been compressed by selecting maximum values and the toroidal heating distribution is shown. Once the single shots had been isolated and characterized within the thermal signals, a way was sought to obtain information on when and how

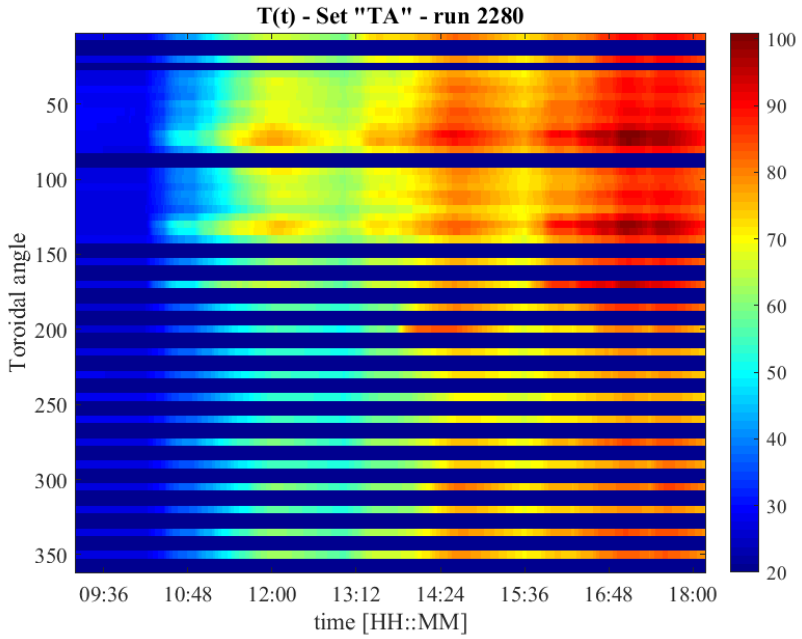

Figure 34: Temperature map along the toroidal angle for run 2280. For each available toroidal position the maximum poloidal measurement is given. Temperature is given with the color scale in Celsius degrees.

much temperature was increasing. For each shot a given number of temporally equispaced ΔT values has been calculated. Two minutes is the chosen time difference between temperature steps, allowing for the heating of the wall tiles but small enough to give a satisfying resolution and number of samples for statistical analysis. These ΔTs are graphically represented as *error bars* in Fig.33, three values are given for most of the shots. By a simple histogram of the two ΔT populations obtained as previously described, the first effect of missing coil compensation on the heating pattern can be appreciated: the shifting of the mean ΔT towards lower values than can be seen in Fig.35 where both compensated and not-compensated histograms are shown, the mean values and standard deviation are ($\mu_{Id} = 1.42°$; $\sigma_{Id} = 0.89°$) and ($\mu_{comp} = 1.23°$; $\sigma_{comp} = 0.88°$) respectively.

To obtain a better picture of the compensation influence on the heating pattern, as well as of the structure itself of this pattern, a geometrical element is very useful. This kind of information can be extracted from the available data thanks to the distribution of thermocouples that gives a good coverage of the

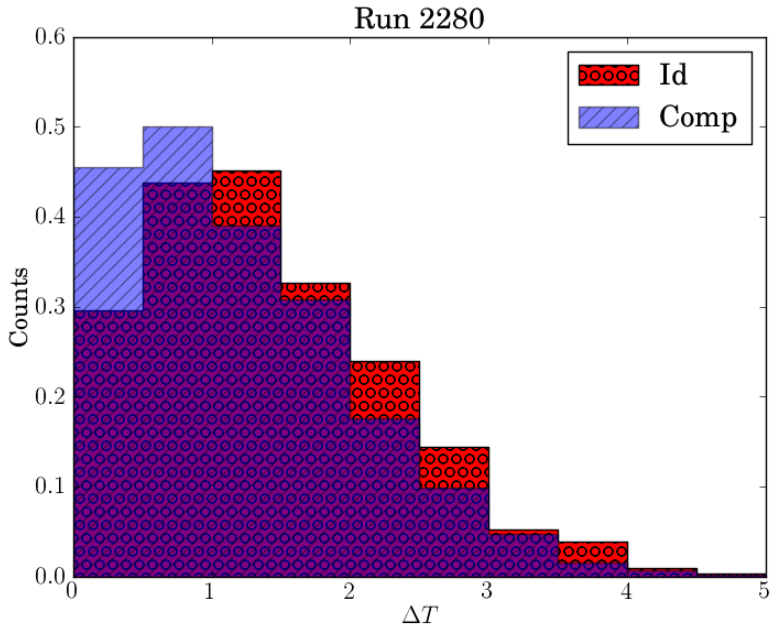

Figure 35: ΔT histograms for the two populations of compensated and not-compensated shots. Each histogram has 10 bins 0.5° wide and is normalized to 1 because of the different number of shots in the two populations.

toroidal angle, within the first 100 degrees in particular, as it has already been stressed with Fig.34. The ΔT data obtained from the above analysis has been filtered to keep the highest values only, the threshold of 2°C has been chosen. After normalizing to the number of elements for each sample, in order to give significant information on the occurrence of high temperature steps, the resulting value can be plotted against the toroidal angle. The result can be appreciated in Fig.36, showing how the percentage of $\Delta T > 2°C$ is reduced in most toroidal positions by implementing the compensation matrix. This effect is particularly clear within the first 100 degrees and can only arise from missing coil compensation since no other significant difference between the shots had been introduced during the experimental campaign. The assessment of missing coil compensation effects can be considered satisfying with this latter result, which a clear demonstration of the benefits introduced by the method described in this paper as far as localized wall heating is concerned.

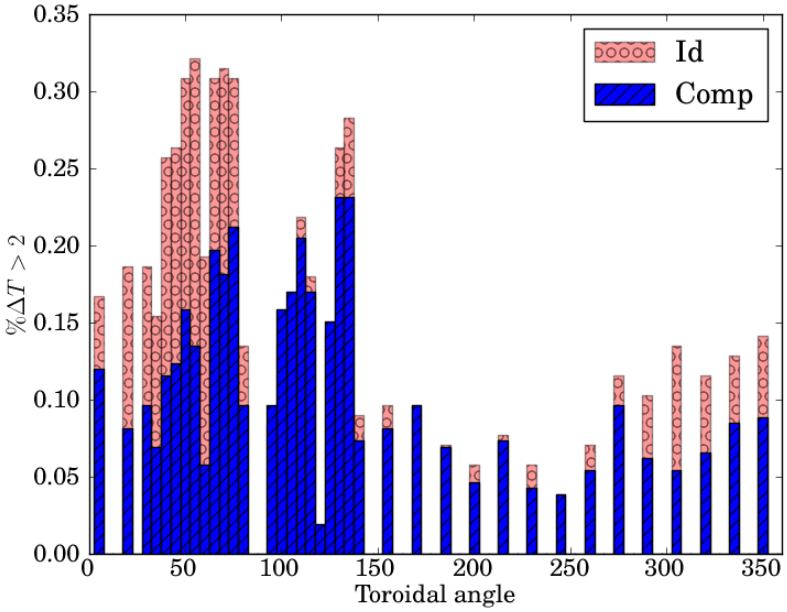

Figure 36: Percentage of ΔT above 2° normalized to the total number of calculated ΔT and plotted for each available toroidal position.

7.4 CONCLUSIONS

The missing coil compensation matrix had been developed [80] to answer the specific need of mitigating local error fields caused by the fault of one or more active coils. These non-uniformities of the magnetic boundary affect plasma performance as preferable spots for mode locking and intense plasma-wall interaction. The compensation matrix has been tested during standard plasma operation, with a wide range of currents, up to 1.65 MA. This testing has been successful and allows to state that the proposed strategy can be safely implemented with weak effects on the total power consumption, as explained with the use of $I^2(t)$ data. The main objective of the campaign though, has been achieved by statistical analysis of the thermal signals. During the highest current run in particular, localized wall heating has been found to be slightly less intense when compensation was used. A stronger effect could be seen in the geometrical distribution of the highest temperature steps, which was positively affected by compensation over most of the toroidal span. This work allowed to assess in an innovative way what the fault of active saddle coils could imply. Since machine repairs are often expensive and time consuming,

simple strategies such as the one tested here could be helpful in mitigating possible damages.

8

MULTI-MODAL RWM ACTIVE CONTROL ON RFX-MOD

"In the consciousness of the infinite, the conscious subject has for his object the infinity of his own nature."

— Ludwig Feuerbach, The Essence of Christianity

[1]The destabilization of a single RWM and its control have been extensively studied in existing tokamaks, but the same is not true for situations where more than one RWM are simultaneously unstable. A spectrum of multiple unstable RWMs in fact is expected in tokamak plasmas operating at β_N values much larger than the no-wall limit, as is in the case of scenarios being developed in view of steady state DEMO reactors. A different situation can be found in RFP plasmas, described in Section 2.7. The RFP configuration is always characterized by the simultaneous instability of multiple tearing mode (sustaining the so-called dynamo mechanism) and RWM spectra. For this reason RFPs provides an ideal playground for the study of 3D RWM passive and active stability. Physics and control of this unstable system are made even more challenging by the intrinsic 3D nature of the problem that involves both the role of the passive structures details and of the 3D fields produced by dedicated coil systems that might act as actuators in a feedback control loop. In the following we will report on recent experiments and modeling activities on RFP plasmas that have been explicitly tailored to study the effect of a realistic (i.e. composed by a reduced number of coils) RWM active control system and to suggest some of the main issues future tokamaks operating at very high β_N values could face when feedback controlling multiple RWMs.

To properly model this complex physical system, quantitative comparison between numerical tools and experimental

1 The content of this Chapter has been published in: *Bolzonella, T., et al. "Physics and Control of External Kink Instabilities with Realistic 3D Boundaries: a Challenge for Modern Experiments and Modeling." Plasma and Fusion Research, Vol. 9* and *Bolzonella, T., et al. 41st EPS Conference on Plasma Physics, Berlin. O4.132*

data involves dynamic representation of toroidal plasma equilibrium and stability, 3D passive boundary, 3D active external field distribution and feedback control software algorithms. This task has been recently successfully accomplished by appropriate upgrading and tuning the CarMa code [81][32], that was first adapted to RFX-mod to reproduce the measured RWM passive growth rates [85] and then coupled to a realistic representation of the RFX-mod control system. The new CarMa version can now incorporate information on the stability of more toroidal harmonics. In this way the model can account for possible toroidal couplings induced on the plasma by passive or active currents flowing outside the plasma. The upgraded multi-modal CarMa version has been then integrated in the full dynamic simulator of RWM control already implemented for RFX-mod experiments and presented in [82]. The model has been extensively validated against experimental data including the plasma response of the most unstable mode, which in the RFX-mod case, for a standard RFP equilibrium, is the internally non resonant $m = 1$, $n = -6$, where m and n stand for poloidal and toroidal mode number respectively.

8.1 REDUCED SETS OF ACTIVE COILS

Reconfigured Arrays

Different configurations of active coils have been tested to investigate the minimum set of coils capable of stabilizing the whole group of RWMs. As introduced in Section 5.1 a wide range of these configurations are possible, the so-called super-coils in particular allow to mimic the effect of a single bigger coil. We can understand the difference of multi-modal RWM control experiments (and modeling) with a reduced set of coils by comparing the vacuum spectrum generated by the full system of 192 coils and one example reduced configuration when trying to produce one single harmonic. This comparison is done in Figure 37, where the target harmonic for both systems is the (1,-6) and all amplitudes are normalized to the amplitude of that of the (1,-6). While the field generated by the full system is basically monochromatic, the reduced array produces many other spurious sidebands, both in poloidal and toroidal directions. To further quantify this effect and easily compare different configurations, we can use the Total Harmonic Distortion (THD) already introduced in Equation 65. This quantity is used in Figure 38 to quantify the difference, in terms of harmonic content (i. e.amount of spurious harmonics), between the full 4×48 con-

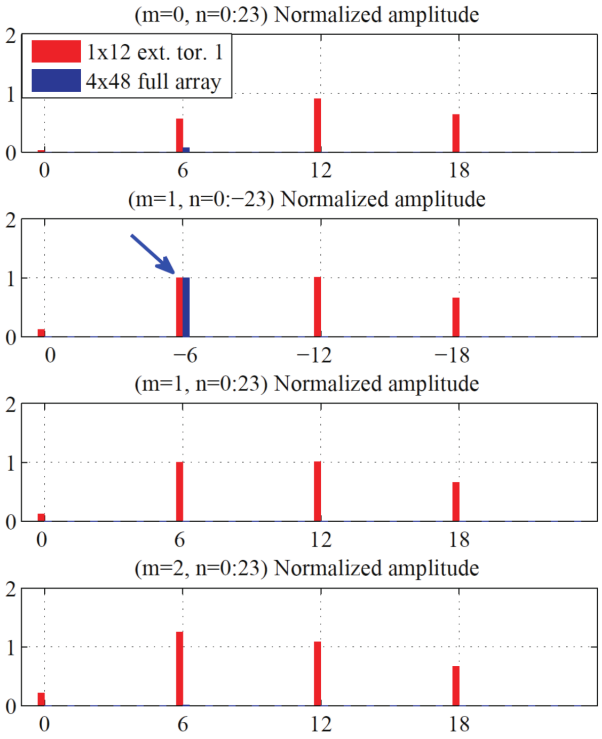

Figure 37: Br spectrum for the (1,-6) target harmonic generated by the full 4×48 array (blue) and by the 1×12 reduced configuration with single toroidal extension.

figuration with respect with two reduced ones: 1×12 with single toroidal extension and 1×12 with triple toroidal extension (i. e.twelve groups of thee coils to form super-coils along the toroidal direction). The dynamical characteristics of the model

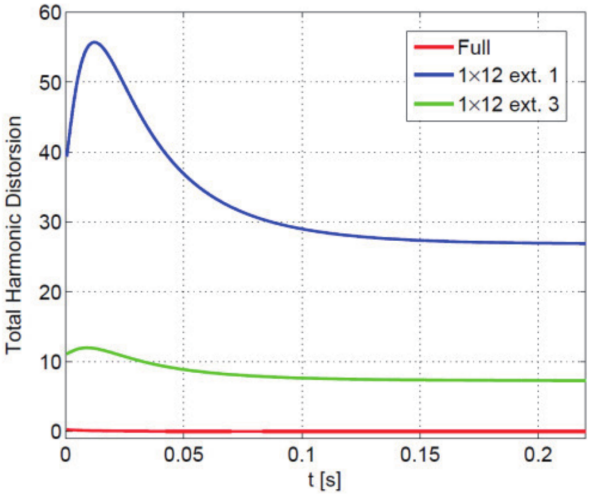

Figure 38: Total Harmonic Distortion for three active coil configurations: 4×48 (red), 1×12 triple (green) and 1×12 single (blue).

allow the estimation also of THD during transients, that for the RFX-mod typical timescales can be of the order of 50-100 ms. The time analysis highlights the importance of shape, showing that the case with larger coils in the toroidal direction (1×12 triple) produces a smaller amount of sidebands during the transient phase than the case with the same number of coils, but narrower (1×12 single).

To fully exploit the new multi-modal capabilities of the model, open loop growth rates were evaluated and compared with experimental ones, when no feedback control is applied. From a control point of view, the open loop model is a dynamic system whose inputs are the saddle coil currents and whose outputs are the radial component of the magnetic field as measured by the saddle probes mounted on the vacuum vessel outer surface. To identify the most unstable modes present in the model, the Fourier transform of the outputs associated to the main eigenvectors (i. e.the eigenvectors associated to the largest unstable eigenvalues) has been evaluated. The eigenfunction exhibiting the higher relative content in the selected (m, n) harmonic has been then selected. Under this assumption it is possible to correlate harmonic components and eigenval-

ues and to perform a direct comparison with the results of 2D Fourier analyses on the experimental saddle sensors measuring the radial component of the magnetic field.

8.2 MULTI-MODAL CONTROL: EIGENVALUE STUDIES

Multi-Modal RWM Control

Different configurations of active coils have been tested to investigate the minimum set of coils capable of stabilizing the whole group of RWMs, in particular trying to improve our knowledge on the rigidity of the plasma response. We use this term to define the possibility of controlling a single mode even by a reduced set of coils without triggering the growth of other modes originally stable. On the contrary, the mode rigidity can be defined as the possibility of controlling that single global mode by applying a local control action.

As an application of the aforementioned model, a particular configuration has been implemented, composed of 3 full poloidal arrays of 4 coils evenly spaced along the toroidal direction (4×3). This has been used on the unstable harmonics m = 1, n = -6, -5, -4, -3 and compared to the less sparse configuration with 6 full poloidal arrays (4×6). In Figure 39 the open-loop RWM eigenvalues are compared to the closed-loop result for the two coil geometries. This eigenvalue analysis points out that the 4×3 configuration cannot stabilize all the four harmonics simultaneously, in particular the coupling of the $m = 1$, $n = |3|$ with the $m = 1$, $n = |6|$ ones makes the system unstable. This coupling cannot be avoided with the sparse 4×3 configuration and it might as well be triggered by the produced sidebands. On the other hand, the 4×6 configuration, which doubles the number of coils, allows for the complete stabilization of the system. A better picture of what a reconfigured coil array is doing, can be grasped by comparing the output magnetic field with the full 4×48 configuration. This can be seen in Figure 40, where the field pattern of a (1,-3) perturbation produced by the full system is compared with the (1,-3) component of the field used to control the four aforementioned harmonics. The same kind of analysis has been done for a different configuration, with eight single coils along the outer toroidal array (1×8), applied to two different sets of unstable harmonics. The results are reported in Figure 41, it is clear that while this control system is able to control the two most unstable modes, the same is not true when also (1,-4) and (1,-3) harmonics are included in closed-loop. Not

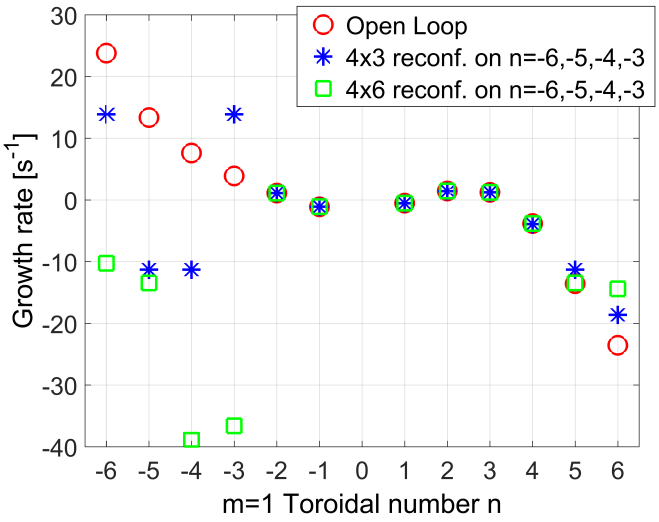

Figure 39: Open-loop (red) growth rates compared to the application of two coil configurations: 4×3 (blue) and 4×6 (green).

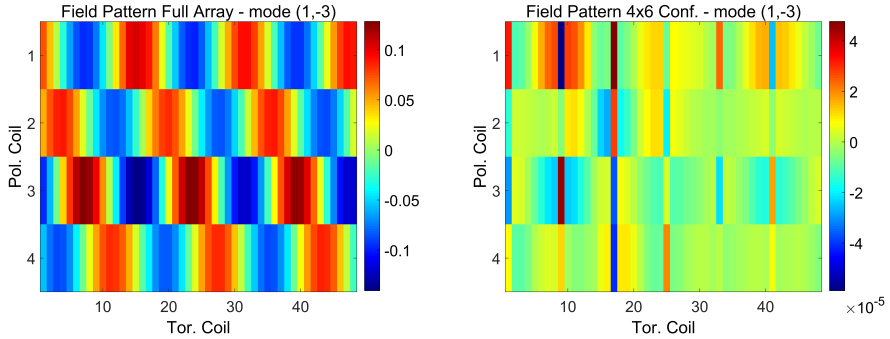

(a) (b)

Figure 40: Magnetic field pattern, as measured by the 192 saddle sensors, of a (1,-3) perturbation generated by the complete system (a) and by the reduced configuration 4×6 when acting on n = -6, -5, -4, -3(b)

only in the latter case one of the modes, the (1,-4), is not controlled because of the periodicity of the active coil system, but also the control of the (1,-5) is lost due to the coupling of the mode to other control fields. It has to be finally noted that also the (1,-3) is destabilized by the closed loop action of the control system in the last case.

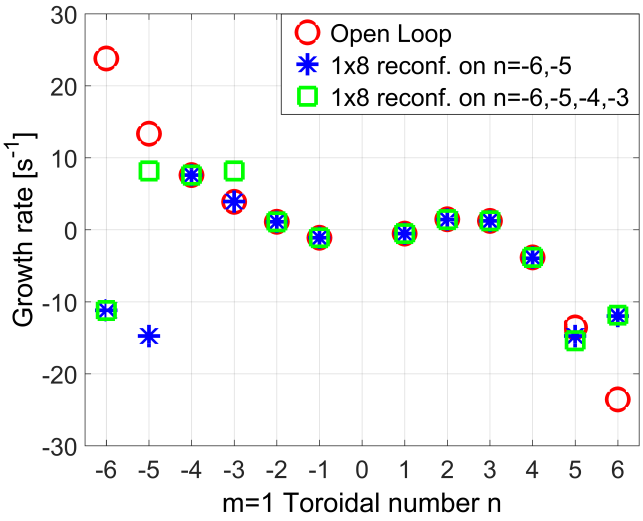

Figure 41: Open loop (red) growth rates are compared to two different control schemes using 1×8 reconfigured coil system.

8.3 CONCLUSIONS

The multi-modal version of the dynamic model for the study of RWM stability on RFX-mod has been implemented and extensively validated. Results are encouraging the possibility of its use as a predictive tool to assist the experimental investigations on the control of RWMs by means of a limited number of active coils. This case can be representative of some control issues typical of multi-modal control in the presence of reduced number/size of actuators. In particular, it is worth noting the fact that unwanted sidebands generated during fast transients by reduced actuator configurations can couple the control external field with other, non-controlled, harmonics. This coupling can be virtuous, in such a way that the spurious harmonics of the external field interact destructively with the plasma and provide stabilization. On the other hand this interaction can be constructive and lead to the destabilization of otherwise (marginally) stable modes by the Resonant Field Amplification

mechanism. We suggest that this might also be the case of future tokamak devices operating at high values of normalized beta, where more than one pressure driven RWM might approach the stability threshold.

Part III

MODELING OF HIGH β PLASMAS AND RESISTIVE WALL MODE STABILITY

9

RESISTIVE WALL MODES IN HIGH BETA FULLY NON-INDUCTIVE SCENARIOS

"Instead of wanting to be like this or that, make yourself into a silent, immovable giant. That's what the mountain [Mount Fuji] is."

— Eiji Yoshikawa, Musashi

[1]As already introduced in Section 2.5, RWM stabilization is one of the crucial tasks for future fusion devices, particularly when aiming at steady state operation and high plasma pressure. For this reason the problem of understanding the physical mechanisms lying underneath these modes, including the possible damping channels, has been challenged in theory and experiments. Dealing with Resistive Wall Modes, which although slowed down by passive structures are still strong ideal instabilities, can be a complex task and has been done in different ways, mainly using passive and active techniques. Passive stabilization is usually sought with a combination of plasma flow and different damping mechanisms such as viscosity or the so-called kinetic resonance with particle drift motions. Plasma rotation has been experimentally seen to have a stabilizing effect on the RWM in tokamak plasmas and many studies are being carried out on the interaction with particle drift motions. The effect of precession drift resonance for trapped particles has been seen important in particular and it will therefore be the first one to be considered here. Other contributions, as bounce resonance from trapped particles or transit resonance from passing ones, should be included in the future for a complete kinetic description and to assess the relative magnitude in reactor-relevant scenarios.

A series of stability studies has been carried out in the present work with the 2D MHD codes MARS-F/K [40][32], which have been describe in Chapter 3, focusing on the most unstable n=1 RWM. A plasma representative of reference Scenario 5.1 (high β_N, fully non-inductive current drive, Single Null) is considered. The specific equilibrium will be described in Section

1 The content of this Chapter has been presented in: *Pigatto, L., et al. "Resistive Wall Mode stability in JT-60SA high β_N Scenarios", 43rd EPS Conference on Plasma Physics, 4–8 July 2016, Leuven, Belgium.*

9.1. As a first step for the assessment of the stability properties of this scenario the ideal kink operational limits have been computed and compared to previously available data (Section 9.2). The Resistive Wall Mode instability is then considered from both the fluid and kinetic [86] point of view. A simple rotation profile is introduced in Section 9.3, then the effect of drift kinetic contributions on the mode eigenvalue is assessed and combined with the aforementioned plasma flow (Section 9.4). Conclusions and possible future developments are drawn in Section 9.5.

9.1 SCENARIO 5.1 EQUILIBRIUM

The reversed magnetic shear Scenario ♯5 belongs to those that should establish the base for high β_N, fully non-inductive current drive operation on JT-60SA. In particular it has been developed to study the MHD limits brought on by Resistive Wall Modes and Neoclassical Tearing Modes. In this part of the thesis we challenge the task of understanding RWM physics in one of the possible Scenario ♯5 equilibria. The implemented equilibrium in particular has been obtained from an integrated modeling simulation performed with the CRONOS suite of codes [87] which used the transport model CDBM [88] for simulating heat transport whereas the density profile has been prescribed. The goodness of this transport model and in general of CRONOS for performing JT-60SA extrapolations was verified with JET and JT-60U data [89]. The boundary parameters, and in particular the pedestal top pressure, have been obtained from the reference Scenario ♯5.1 [90]. The resulting scenario represents a version with lower input power developed using 17 MW of NBI and 7 MW of ECRH, therefore leaving sufficient power management flexibility for mode and profile control purposes. The normalized β value is 3.6, with $q_{95} \sim 6.5$. The original equilibrium has been smoothed in its internal profiles ($\frac{dp}{d\psi}$ and $f\frac{df}{d\psi}$ where p is the pressure and f the poloidal current flux function, as defined in Eq. 16-17) and plasma boundary, in order to avoid numerical issues and increase the resolution close to the x-point. This latter point itself has been effectively removed, since it cannot be treated by the used codes, in a way such that the safety factor profile is left almost unaffected. The resulting plasma boundary and q-profiles are shown in Figure 43, it is worth noting that the smoothing procedure gives negligible

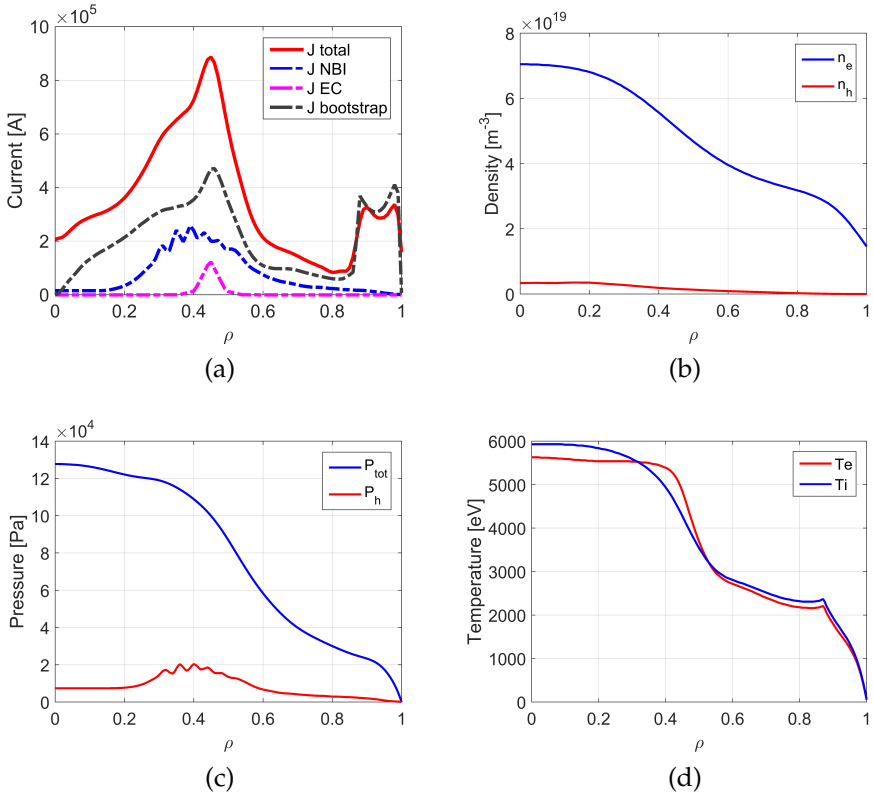

Figure 42: Relevant radial profiles for the implemented equilibrium. Plasma current components (a), electron and hot ions density (b), total and supra-thermal pressure components (c), ion and electron temperature (d).

changes, from the MHD point of view, in the original equilibrium.

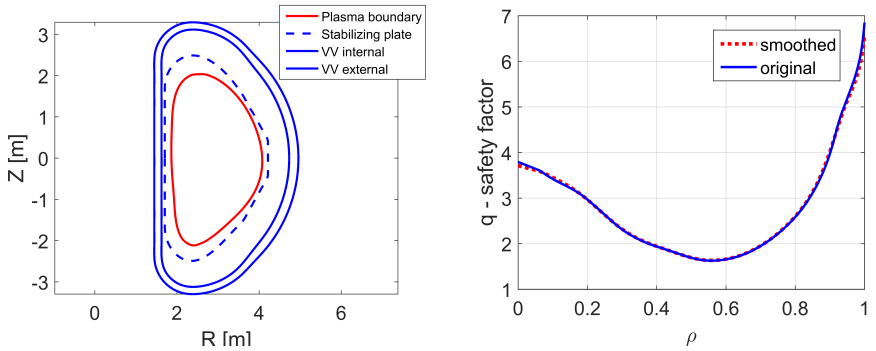

(a) (b)

Figure 43: (a) Plasma boundary, first wall (i. e.stabilizing plate) and vacuum vessel contours. (b) Safety factor profile before (blue) and after (red dashed) smoothing of plasma boundary and internal profiles.

9.2 NO-WALL AND IDEAL-WALL STABILITY LIMITS

Identification of no-wall and ideal-wall limits is important for the assessment of the operational space in which Resistive Wall Mode stability is relevant, and the whole setting of this work consequently. As a first step in understanding the stability properties of the aforementioned equilibrium the no-wall and ideal-wall β limits have been assessed with a pressure scan. The results predicting $\beta_{nw} = 1.96$ and $\beta_{iw} = 5.40$ (Figure 44) are consistent with those obtained for similar equilibria [91]. It should be stressed that only one wall has been implemented in this study (dashed in Figure 43b), as a continuous 2D contour that does not take into account the real geometrical characteristics of the stabilizing plate such as gaps or non-uniformities. The plasma-ideal-wall distance has been scanned and set as to allow consistency with previous results. This however leads to an optimistic ideal wall limit; comparison with fully 3D simulations is foreseen in order to establish an equivalent effective wall position and obtain more realistic β_{iw} estimation. With a $\beta_N = 3.6$ the reference equilibrium is in between the calculated limits, in the so-called wall stabilized region, where the ideal wall stabilizes the external kink. Since any realistic wall has a finite resistivity this mode is not fully stabilized but slowed down from Alfvénic time scale to the wall penetration characteristic time.

In this case the computed Alfvén time is $\tau_A \approx 9.66 \times 10^{-7}$ s. In the following work a 2D thin wall has been implemented which does not take into account the real three-dimensional characteristics of the stabilizing plate. The time constant of this simplified boundary has been calculated with a vacuum MARS-F run to be $\tau_W \approx 10$ ms. All the results related to RWMs are presented with a normalization to τ_w, but can be rescaled to any calculated wall time for comparison with other codes and data. Since the Resistive Wall Mode instability can be influenced by both plasma flow and kinetic properties of the plasma, these relationships and their effect on mode dynamics are investigated in the following sections.

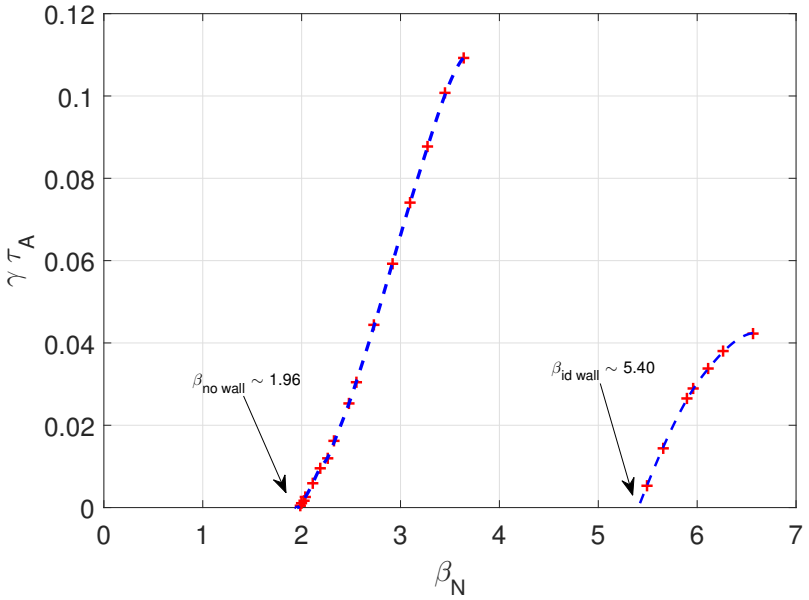

Figure 44: No-wall and Ideal-wall stability limits calculated with constant plasma current and ideal wall position b/a = 1.119

9.3 STABILITY OF FLUID RWM: EFFECTS OF PLASMA FLOW AND FLOW PROFILE

Stabilization of the most unstable n=1 RWM is explored with plasma rotation, an ion acoustic Landau damping term is included in the momentum equation, in particular as a viscous term. The perturbed viscous force can be expressed as:

$$-\nabla\overrightarrow{\Pi} = \rho\kappa_{\|}|k_{\|}v_{th,i}|\overrightarrow{v}_{\|} \tag{71}$$

This term is scaled with the strength parameter $\kappa_{\|}$ which has been set here to 1.5 in order to achieve a significant damping.

While the NBI systems on JT-60SA allow great flexibility in the design of plasma flow, efforts are ongoing to obtain self-consistent rotation profiles [92]. In order to make the discussion as general as possible, two simplified cases have been implemented here. A parabolic rotation profile has been assumed and compared with the uniform rotation case. The effect of viscous damping on the RWM can be seen in Figure 45 where the rotation at the innermost q=2 magnetic surface is scaled. Normalization to the τ_w factor is applied to the eigenvalues, while the flow is normalized to the Alfvén frequency (ω_A) is applied. A strong damping of the growth rate ($\gamma\tau_w$) is given by the uniform rotation profile in particular. Even though the normalized rotation frequency at the q=2 surface is used in the Figure 45 plots, a very different behavior is found for the two considered situations. This probably indicates that the whole global rotation profile has an effect of the fluid RWM stability, thus opening to the possibility of profiles tailored on the control requirements. The presence of two

$$\omega_A = \frac{B_0}{R_0\sqrt{\mu_0 m_i Z n}} = 1.06 \times 10^6 s^{-1}$$

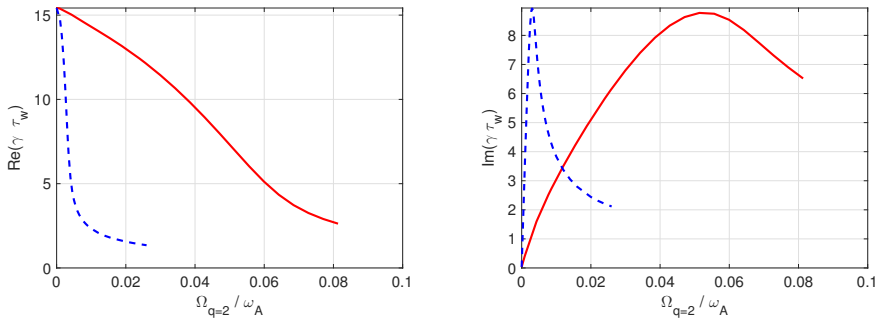

(a) (b)

Figure 45: Eigenvalue scaling with toroidal plasma flow for uniform (dashed blue) and parabolic (red) rotation profiles. (a) Real part, (b) imaginary part.

q=2 rational surfaces in the plasma, due to the reversed safety factor profile, as well as the complex nature of the n=1 mode, can be responsible for the importance of the flow profile along the whole minor radius. As a result of this purely fluid rotation scan we can confidently say that mode stabilization is not achieved, although the growth rate can be significantly reduced. It is worth noting that reasonable plasma flow velocity should be used for mode stabilization, which has been estimated being of the order of $0.03v_A$ for a fast rotating case [93]. It is therefore mandatory to investigate further damping mechanisms which can be both active and passive. In the following sections some

of the most relevant effects in terms of passive stabilization are introduced in the model, while the subject of active stabilization will be addressed in future work.

9.4 KINETIC CONTRIBUTION TO RWM STABILITY

As already remarked in the introductory sections the behavior of RWMs will be influenced by drift kinetic effects [33] from both thermal and energetic particle populations from NBIs, these contributions have been included in the stability analysis. Thermal ions and electrons have been introduced as a first step, assuming a simple Maxwellian distribution and focusing on the resonance between the mode and the precession motion of trapped particles banana orbits. This will be named *2-species* in the following. Energetic Particles (EPs) from normal NBI injection have been then introduced, i. e.the *3-species* case. For EPs a slowing-down distribution is assumed in particle energy space and isotropic distribution in particle pitch-angle [63]. For both cases the kinetic contribution to the pressure tensor is scaled though the α_D parameter, as shown in Figure 46. The dependence of the eigenvalue on the kinetic contribution is reported for both the two particle species and three particle species (including EPs) case, without plasma flow. Figure 46 shows how the n=1 eigenvalue is slightly modified, in its real part, by the kinetic contribution of thermal particles. A more significant modification is seen when the energetic population is included, this is due to the further non-adiabatic contribution to the perturbed kinetic potential energy. It should be mentioned that the small effect that is found in Figure 46 is probably given by the large growth rate and frequency of this particular RWM. The base equilibrium which have been considered here is quite far from the no-wall limit, giving rise to a strong instability that reduces the effect of kinetic damping. All the components of the potential energy can be evaluated at various levels of detail, here we choose to focus on the drift kinetic contributions and their relationship with plasma rotation. The effect of rotation is being assessed in presence of kinetic effects with the same procedure followed in the purely fluid case, using a smaller parallel viscosity coefficient this time ($\kappa_{\|} = 0.1$). This means that in the following kinetic simulations rotation is to be considered mainly given by $E \times B$ flow. The uniform rotation profile has been assumed for this proof-of-principle study, rotation amplitude has been scanned up to the stability threshold for

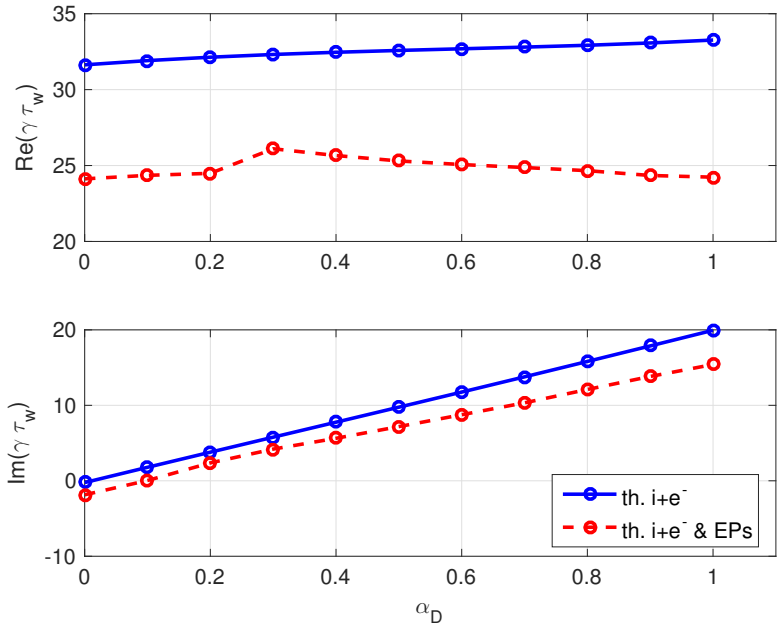

Figure 46: Dependence of the eigenvalue on the drift-kinetic contribution with two populations (thermal ions and electrons, blue solid line) and three populations of particles (thermal ions and electrons + energetic particles, red dashed line). The parameter α_D represents scaling from fluid description ($\alpha_D = 0$) to full kinetic contribution to the pressure tensor ($\alpha_D = 1$). No plasma flow is applied.

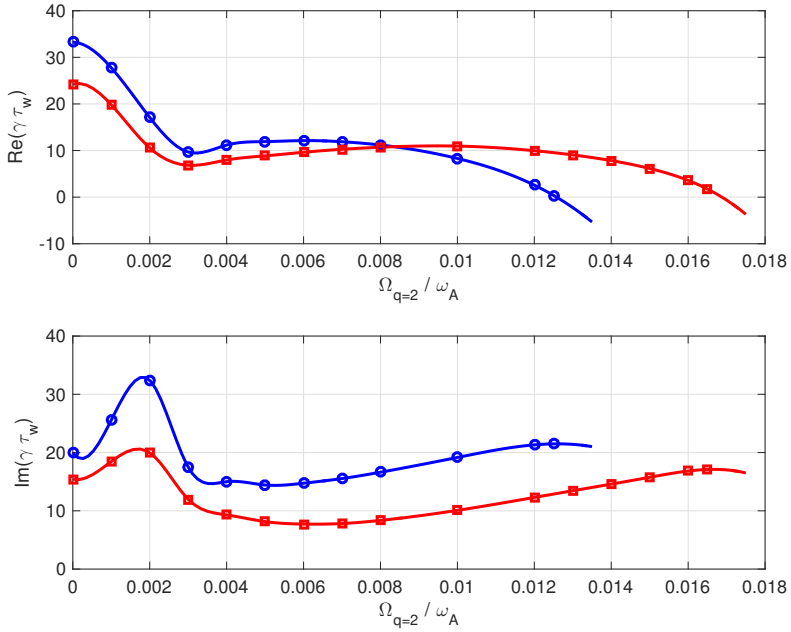

Figure 47: Toroidal rotation scan for the kinetic RWM in the 2 species (blue-circles, thermal ions and electrons) and 3 species (red-squares, thermal + EPs) cases. A uniform rotation profile is assumed.

both the 2-species and 3-species case. As Figure 47 reports, a strong damping is obtained for both cases, interestingly enough a slightly higher critical frequency is found for the 3-species. These two frequencies are found to be $\omega_{2spec} \approx 0.0126\omega_A$ and $\omega_{3spec} \approx 0.0169\omega_A$ for 2-species and 3-species respectively. In order to characterize the effect of rotation and kinetic particles on the mode structure, the perturbed plasma displacement along the radial coordinate has been reported for the purely fluid simulation compared to the 3-species case with rotation ($\Omega = 0.012\omega_A$). Figure 48 shows this comparison, highlighting a smaller displacement, with respect to the fluid case, within the plasma as well as the increased effect of rational surfaces. In Figure 49 we report the parallel and perpendicular components of the pressure tensor in Eq. 45, which reflect modal structure with all its components. Detailed analysis of the potential energy contributions has been done to characterize mode stability while varying rotation, all the calculated components of δW_k are normalized by the plasma inertia associated with radial displacement. If the electron contribution to δW_k can be neglected, the population of thermal ions is found to be much

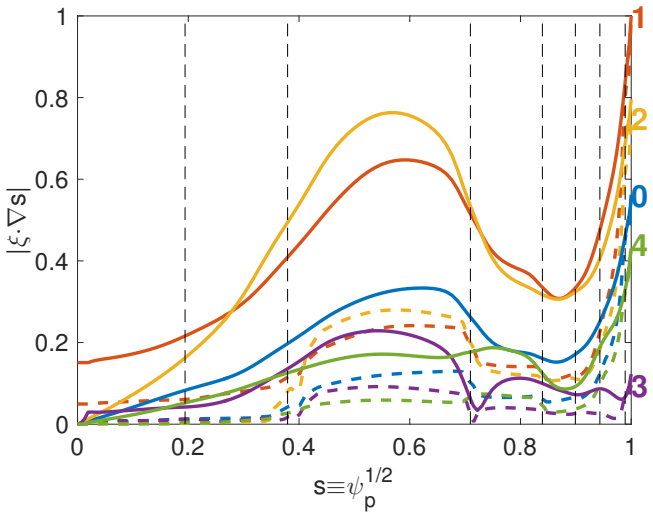

Figure 48: Comparison of RWM eigenfunctions between fluid (solid) and kinetic theory (dashed) including thermal and energetic particles. Example with $\Omega = 0.012\omega_A$, the q=m/n surfaces are marked with dashed black lines. Fourier harmonics of the perturbed radial displacement are given in the equal-arc coordinate system introduced in Chapter 3.

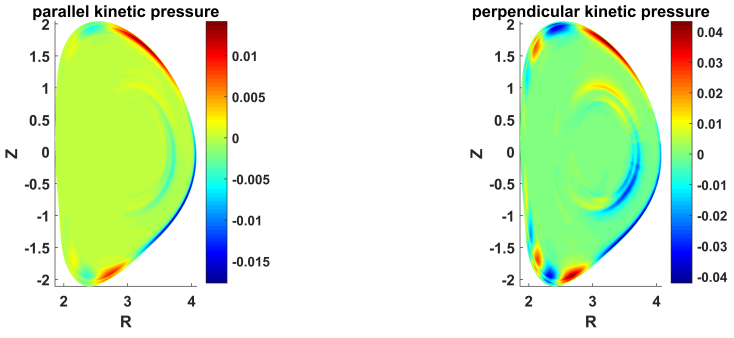

(a) (b)

Figure 49: Example of parallel (a) and perpendicular (b) kinetic pressure components for 2 species case with toroidal rotation $\Omega = 0.01\omega_A$

more relevant, as we can appreciate from the bottom plots in Figure 50. It is worth noting that the thermal ions contribution

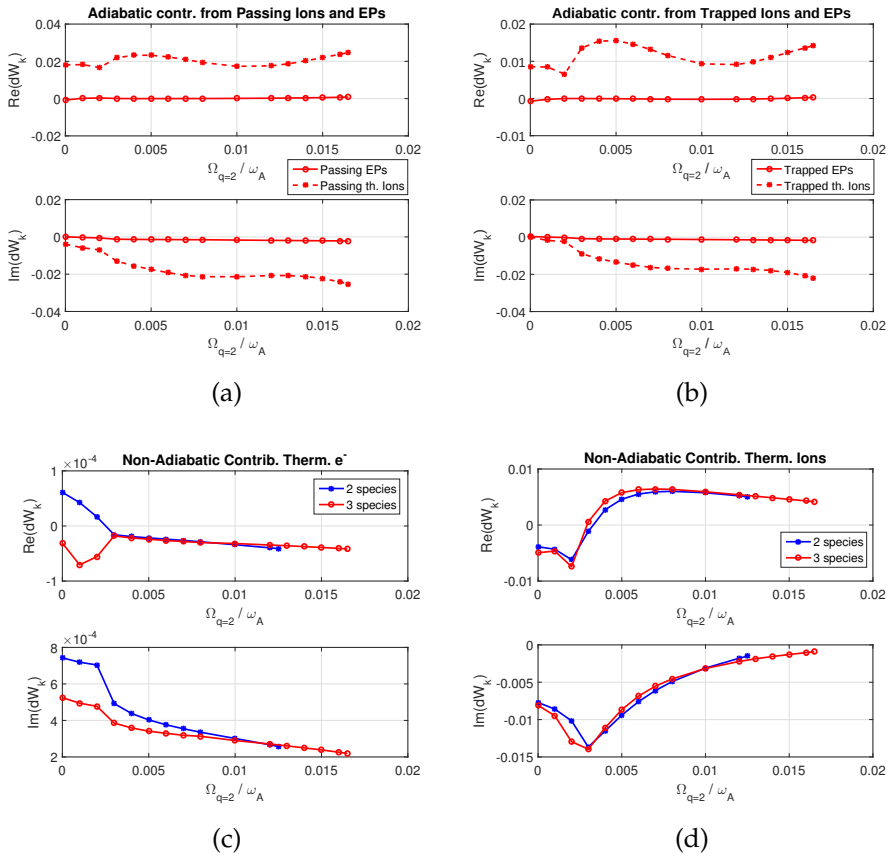

Figure 50: Real and imaginary parts of drift kinetic energy components: for the 3-species case adiabatic contributions from passing (a) and trapped (b) particles. Non-adiabatic parts from thermal electrons (c) and ions (d) are compared for both cases. Energy components normalized to plasma inertial associated with radial displacement.

has the same evolution in the rotation scan for both 2-species and 3-species. For the latter case the EPs component of δW_k is separately shown in Figure 51a. An increasing stabilizing effect is seen at $\Omega \sim 0.002\omega_A$, explaining the damping in Figure 45 around the same frequency. This in particular is the value corresponding to the ion diamagnetic drift frequency. Figure 51b shows all the components of δW_k added together for both the 2-species and 3-species case, highlighting a stronger damping effect introduced by EPs in the imaginary part of δW_k. As previously mentioned, this effect shows a peak close to the ion diamagnetic drift frequency, but then decreases with scaling rotation.

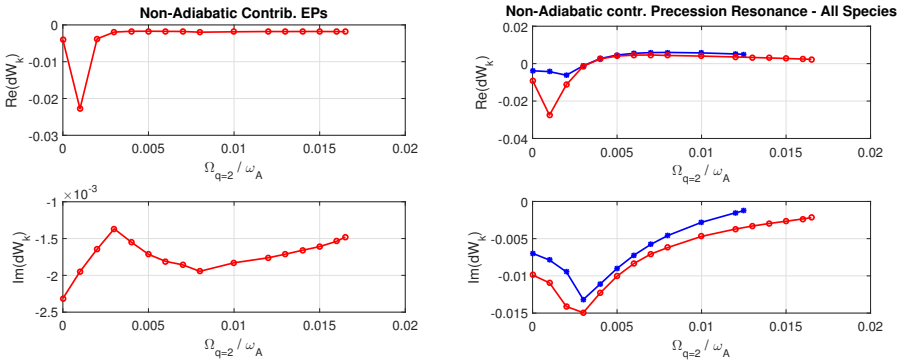

(a) (b)

Figure 51: (a) Real and imaginary part of non-adiabatic contribution from EPs to the perturbed potential energy. (b) Real and imaginary part of the total perturbed kinetic energy, contributions from all populations are added together for the 2-species and 3-species case.

9.5 CONCLUSIONS

The ideal and no-wall β limits have been calculated for the n=1 ideal kink in the fully non-inductive scenario 5.1, future comparison with 3D calculations will allow a more detailed description and the effective 2D wall will be positioned. The n=1 RWM will be unstable in the scenario under investigation with a close-fitting resistive wall. Stability studies with fluid rotation have been carried out by implementing two simple profiles, none of which provides full mode stabilization. This means that the RWM cannot be stabilized by fluid effects only, kinetic contributions must be taken into account. The uniform rotation case in particular is found to give a stronger damping, suggesting that the global rotation profile should be taken into account over the single q=2 surface. An extended fluid analysis of the problem is possible with different, detailed rotation profiles and a 3D description of passive structures which would allow including new energy terms. Further physics is being implemented in the description step by step, starting with the kinetic contribution of thermal and EPs. Future work will consider more advanced distribution models for the latter. Mode evolution in both these cases is still under investigation but giving promising results when energetic particles are included in particular. A further important future step will be the study of RWMs with different toroidal numbers, which can be simultaneously unstable in the considered scenarios. Active stabilization studies,

which could prove to be necessary, are currently ongoing with a simplified physical model not including kinetic effects. The present work represents a summary of some of the first efforts in characterizing RWM stability in JT-60SA high β plasmas. The results achieved so far are encouraging the possibility of stable operation though improvement is necessary and foreseen, with reference to the kinetic profiles and energetic particles distributions in particular.

10

ACTIVE CONTROL OF RESISTIVE WALL MODES ON JT-60SA

"True heroism is minutes, hours, weeks, year upon year of the quiet, precise, judicious exercise of probity and care, with no one there to see or cheer. This is the world."

— David Foster Wallace, The Pale King

[1]As illustrated in Chapter 2, it is well known that in the case of Advanced Tokamak (AT) plasmas, the so-called no-wall stability threshold of ideal external kink modes can be reached at β_N values that strongly limit the operational space of such scenarios. For this reason stabilizing effects are studied, both passive (e. g.as in Chapter 9) and active (e. g.external coils). This latter method is the topic of the present Chapter, in which a dedicated CarMa model [94] is applied to RWM feedback control in a JT-60SA AT scenario.

10.1 CARMA MODEL AND OPEN-LOOP ANALYSIS

A simplified plasma description, given by the MARS-F code, has been coupled to a detailed representation of the stabilizing plate and active coils. A 3D view of these structures is given in Figure 52. In the following, the error field correction coils will not be used and have been therefore excluded from the model. The results that will be described in the present work refer to the equilibrium configuration reported in Chapter 9, scaled to $\beta_N \sim 2.7$. In the model the most unstable eigenvalues can be selected and identified as RWMs from their growth rates and from the comparison with the 2D problem solved by MARS-F. Synthetic magnetic probes have been added to the 3D model to document e. g.how the most unstable RWM would appear. From a total of 108 magnetic probes available in JT-60SA for real time measurements, 39 will be placed on the stabilizing plate close to the plasma on the low field side. A view the sensors positions is given in Figure 53. It is worth noting that the magnetic

1 Part of this Chapter has been presented in: *Bolzonella, T., et al. "Securing High β_N JT-60SA Operational Space by MHD Stability and Active Control Modelling", 26th IAEA Fusion Energy Conference, 17–22 October 2016, Kyoto, Japan.*

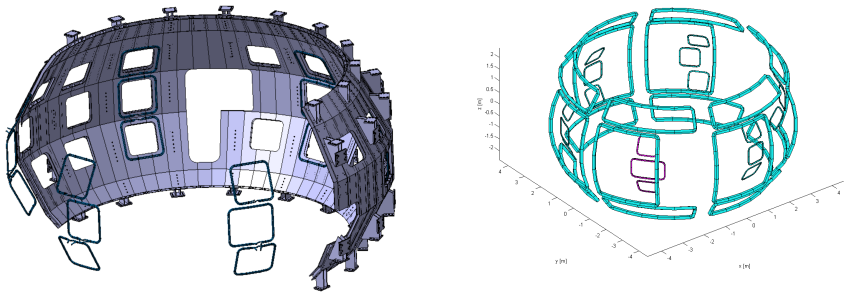

(a) (b)

Figure 52: 3D representation of the Stabilizing Plate (a) and of the active coils (b), both Error Field Correction Coils and Resistive Wall Mode control Coils.

probes are shifted with respect to the center of the active coils of 30°, since they are placed underneath the toroidal field magnets. In Figure 54 the 3D current density pattern corresponding

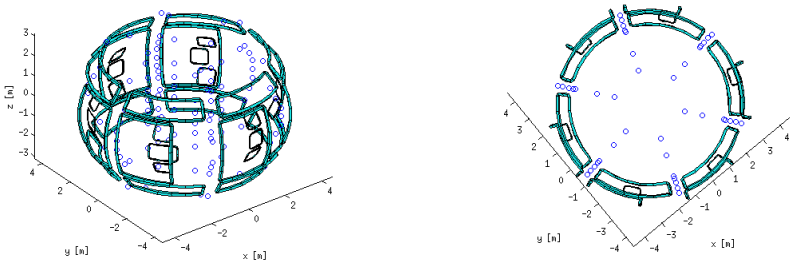

(a) (b)

Figure 53: 3D view of the active coils and sensors, side (a) and top (b).

to the unstable n=1 eigenfunction is shown, as computed by the CarMa code. A more detailed description of the coupling procedure and of the features of 3D structures together with some preliminary results can be found in [94]. A coil current input model has been built with the CarMa code output. This allows for straightforward implementation of the desired control schemes with the implicit assumption that the current control loop is capable of meeting the requests. A more detailed discussion concerning the current requirements will be given in the following sections. An open-loop version (i. e.without any active external action) of the model has been used to evaluate

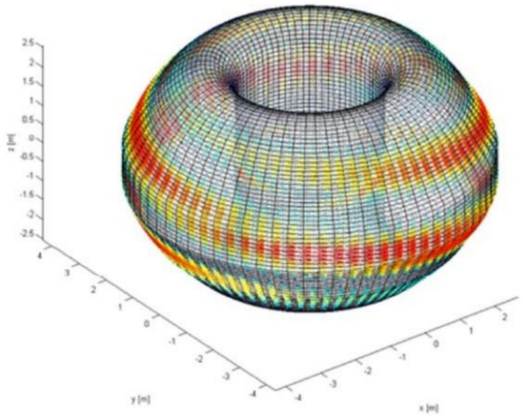

Figure 54: 3D view of the current density pattern corresponding to the unstable n=1 eigenfunction, computed by the CarMa code [94].

free-mode evolution, spatial distribution and harmonic content. Interestingly enough, due to the 3D features of the stabilizing plate, which exhibits holes with no periodical symmetry, the expected unstable RWM is actually split in two modes, with different imaginary part (phase) and slightly different growth rates. These latter are found to be $\gamma_1 = 551 s^{-1}$ and $\gamma_2 = 402 s^{-1}$. When moving to a possible active control strategy, as a first attempt a modal control scheme has been chosen, focusing on the n=1 harmonic of the tangential component of the magnetic field. The poloidal harmonic content of such a mode has in general many components, with an internal kink structure (m=1) in the core and higher mode numbers towards the plasma boundary. One of the most significant however, is the m=2 harmonic that characterizes the RWM component of the mode, located between the two q=2 surfaces and close to the edge. This is shown in Figure 55 with the m=2 harmonic of the perturbed plasma displacement as calculated by MARS-F. As a first step, only the uppermost and lowermost active coil arrays (along the toroidal direction) have been implemented. This choice has been made for practical reasons that will be explained in the following section. Figure 56 shows the spatial distributions of the magnetic field tangential component in the poloidal plane as measured by the uppermost and lowermost toroidal arrays of sensors, located onto the stabilizing plates (6 probes each in toroidal direction); please note that the tangential component is to be understood as the field component tangential in a poloidal section to the plane where the sensor is installed (i.e. mainly, but not exactly, poloidal in a physical reference frame). The splitting of

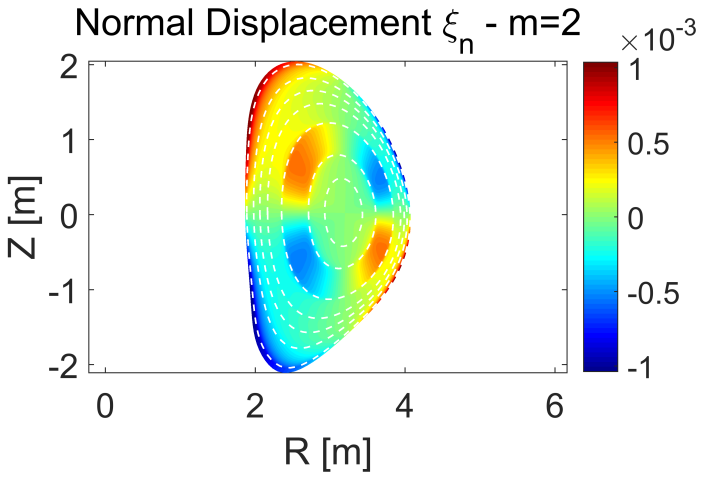

Figure 55: Normal component of the perturbed plasma displacement, m=2 harmonic, calculated by MARS-F.

the most unstable mode into two different parts is clearly visible from both the implemented sensor arrays. A largely prevailing n=1 harmonic content can be appreciated in both eigenfunctions by a DFT analysis of the same measurements, as shown in Figure 57.

10.2 CLOSED-LOOP PROOF-OF-PRINCIPLE

As previously mentioned, in order to begin the closed-loop analysis of the problem, the model has been reduced to arrays of equispaced sensors and coils. In particular the upper and lowermost sensor arrays have been used, coupled to the top and bottom sets of actuators. This has been done in order to apply a modal control scheme with a straightforward Discrete Fourier Transform (DFT) of the magnetic field. Further complications to take into account more sensors and all the active coils will be introduced later. Another preliminary step has been done in verifying the vacuum field produced by the coils with a known sinusoidal reference input. This is shown in Figure 58, where a cosine-like signal is fed to the actuators, which produce a magnetic field shifted in phase of about $\pi/2$. This shift will be taken into account in the following eigenvalue analyses of the closed-loop system. As already stated, a modal control scheme has been chosen, focusing on the n=1 harmonic of the tangential component of the magnetic field. This is proposed in agreement with experimental results obtained by the same ap-

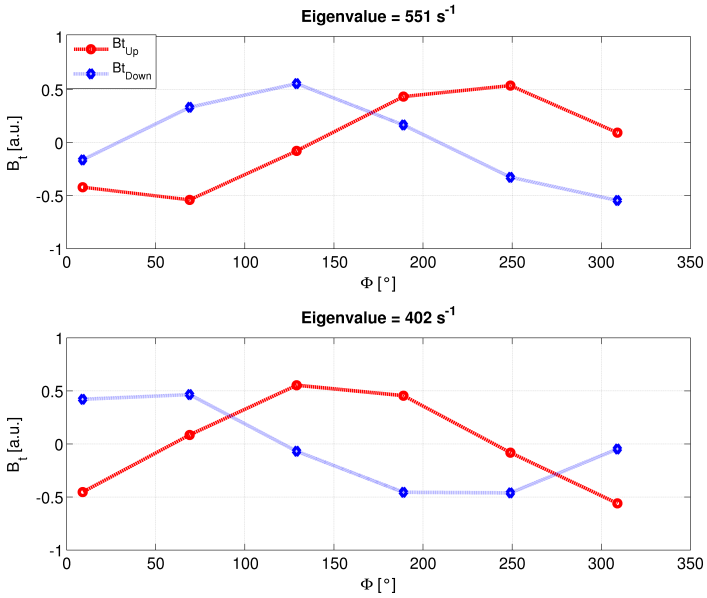

Figure 56: Spatial pattern of the two most unstable eigenvalues obtained from the open loop model. The tangential component of the field (here in arbitrary units) is shown against the toroidal angle corresponding to each sensor. The n=1 dominant harmonic component is clearly visible .

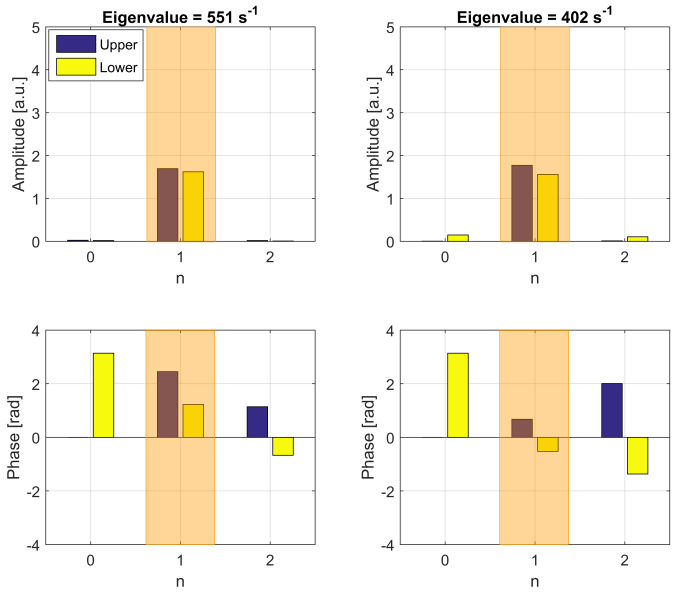

Figure 57: The spatial Fourier transform along the toroidal direction shows the dominant n=1 component in both unstable eigenvectors, both seen by the upper (blue) and lower (yellow) sensor arrays. The dominant n=1 components are highlighted by orange boxes.

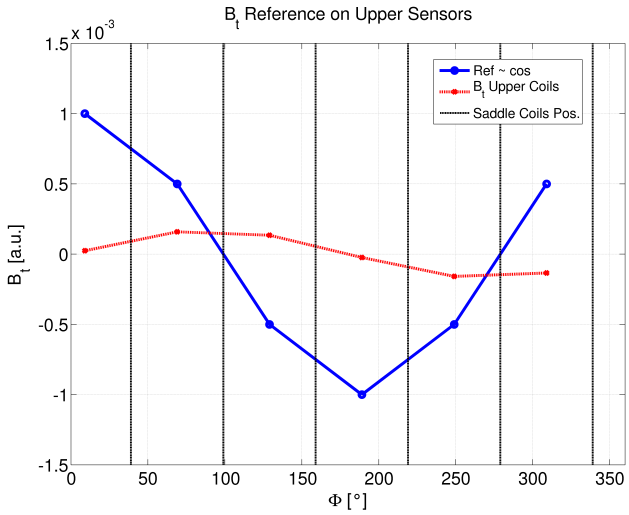

Figure 58: Cosine input signal (blue) and vacuum magnetic field produced by the upper active coils (red) as measured by 6 probes of the uppermost toroidal array. The position of the coils is marked by the black dotted lines.

proach in different experimental devices [95] that showed how this choice guarantees to reduce the coupling between the actuators and the feedback signal. Following the feedback control implementation strategy sketched in Chapter 6, the DFT of the signals from the upper and lower sensor arrays is calculated and the control relevant harmonics selected. A corresponding harmonic signal is obtained at the controller output, whose inverse transform is then evaluated along the toroidal coordinate, taking into account the coil periodicity (in this case equal to that of the sensors) and the angular shift with respect to the sensors. The choice of selecting only the upper and lower coil arrays allows for a one-to-one sensor-actuator correspondence with constant angular shift. A set of references for the upper and lower coil currents is generated, assuming an ideal current control scheme. The result of a first gain scan using only the uppermost coils is reported in Figure 59. It is interesting to note that stability of both unstable modes is achieved, even with a reduced configuration and ideal proportional controller. Further studies are then necessary to include the other actuators and assess the feasibility in terms of current of the control strategies made possible by the independent coils.

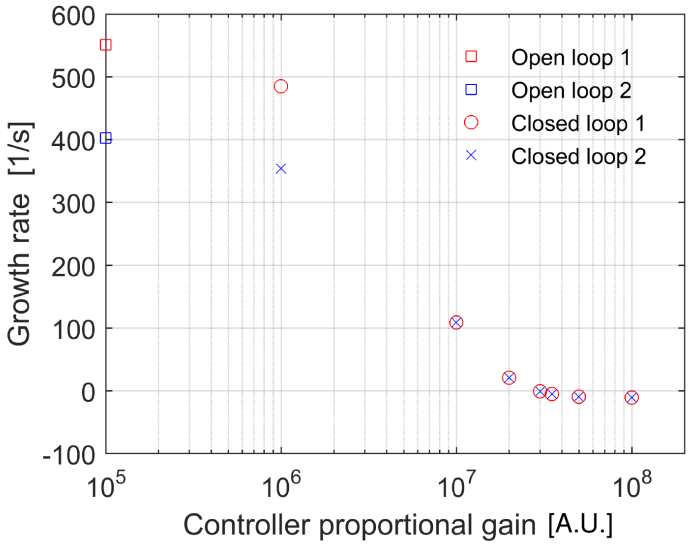

Figure 59: Gain scan on the two unstable eigenmodes using the upper coil array.

10.3 FULL ACTIVE SYSTEM IMPLEMENTATION

In order to fully exploit the capabilities of the active system, the equatorial coil array has been implemented, coupled to a set of magnetic sensors located on the Stabilizing Plate along the equatorial length. This latter however is found to be composed of 5 magnetic sensors only, compared to the 6 constituting the upper and lower arrays. In order to recover a one-to-one actuator-sensor relationship and perform DFT analyses, an interpolation has been implemented. The necessity for this interpolation can be understood from Figure 60 where the open-loop spatial pattern is shown for both unstable modes and the three arrays. It clearly appears that the equatorial array is lacking the measurement at $\Phi = 205°$. In order to interpolate the missing measurement two more sensors have been used, located just above and below the desired position. It should be noted that these new sensors do not belong to the so-called uppermost and lowermost arrays, but they are different probes located on the Stabilizing Plate closest to the missing one position. Preliminary analyses of the open-loop system have allowed to identify the interpolation over the poloidal angle as the best choice, in terms of the capability of the system to measure a given reference field from each of the active coils. In particular, for the position corresponding to $\Phi = 250°$, the equatorial magnetic field has been reconstructed by using the first upper and lower

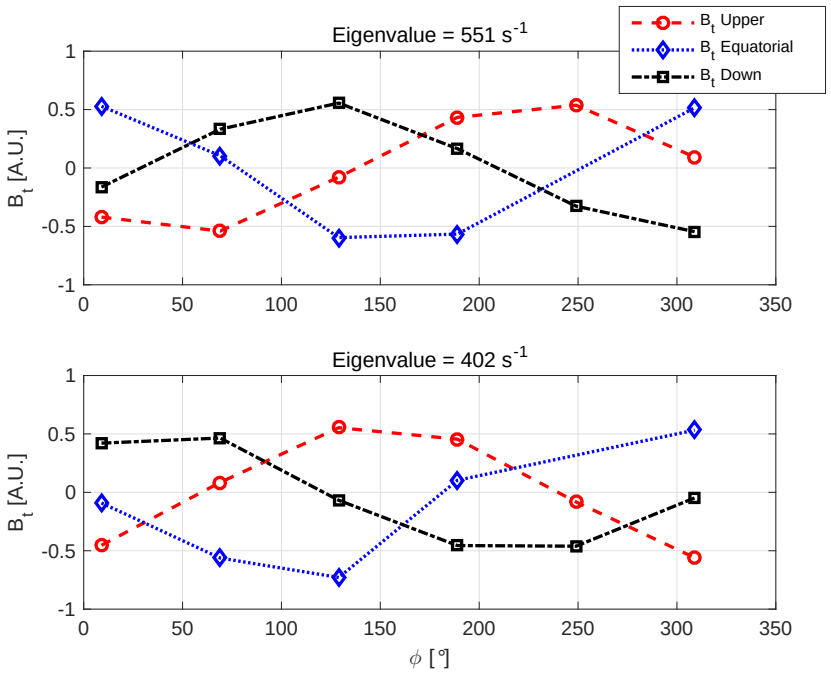

Figure 60: Spatial pattern of the two most unstable eigenvalues obtained from the open loop model with upper (red dashed), equatorial (blue dotted) and lower (black dot-dash) arrays. The tangential component of the field (here in arbitrary units) is shown against the toroidal angle corresponding to each sensor.

available measurements. This procedure is shown in Figure 61, where the measured patterns are given in dashed red line and the interpolated field in blue dotted line for both eigenmodes.

10.3.1 *Eigenvalue Analysis of the Full System*

A set of preliminary analyses with a dedicated vacuum model have been carried out in the same way outlined in the previous section. This vacuum version allows a full spatial and dynamic characterization of the magnetic field produced by the actuators in the presence of non-axisymmetric passive structures. Also following the same track, an eigenvalue study of the system has been performed to evaluate the critical gain required for mode stabilization. A constant phase shift has been applied to the action of each coil in order to maximize its effect. These phases have been calculated during the open-loop preliminary analyses with a helical reference signal. The gain scan reported in Figure 62 shows that the unstable modes are fully stabilized with a proportional gain of 7×10^6 A/T. The applicability of such a gain cannot be assessed with instruments such as eigenvalue analyses and requires challenging the problem from the point of view of time simulations.

10.3.2 *Time Domain Simulation*

The closed-loop system represented has been implemented as a Matlab®Simulink model to obtain a dynamic simulator for RWM control studies. This allowed the development of simulation tools similar to those shown in Chapters 6 and 7. A gain scan similar to that shown in the eigenvalue study has been performed around the supposed critical value. The time simulations are confirming the previously calculated stabilizing gain, as it can be appreciated in Figure 63 where the amplitude of the n=1 harmonic is plotted for the three sensor arrays. As for the previous eigenvalue analyses, the tangential magnetic field is used as feedback variable for the time simulations. An initial free evolution phase, lasting 10 ms, has been set to allow the desired mode to develop from the random initial condition (generated $t = 0$ s). The feedback loop is then closed with three different gains: 4×10^6 A/T, 6×10^6 A/T and 8×10^6 A/T. The stabilizing threshold is found in between the last two values. It is worth noting that two different dynamics are found in the closed-loop part of the simulation. The mode undergoes a

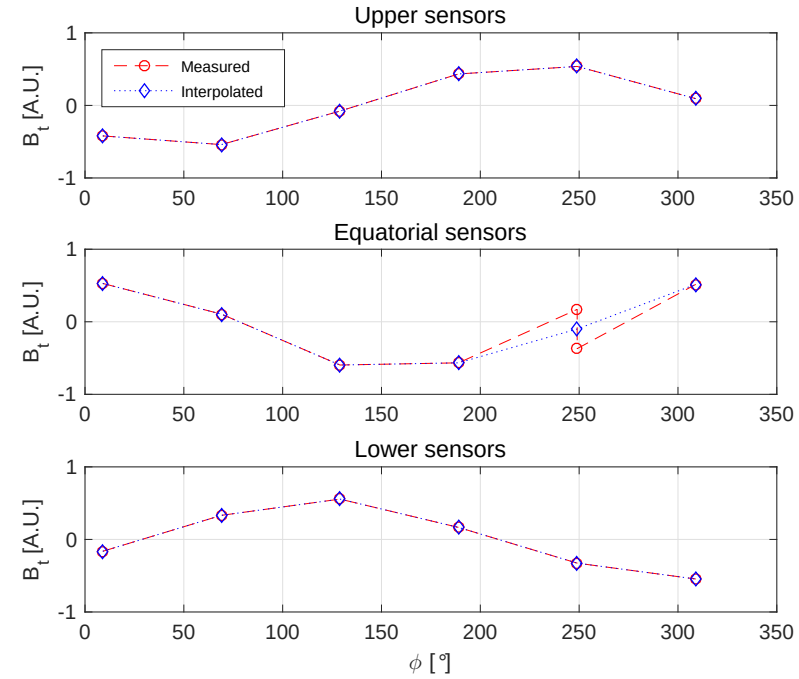

(a)

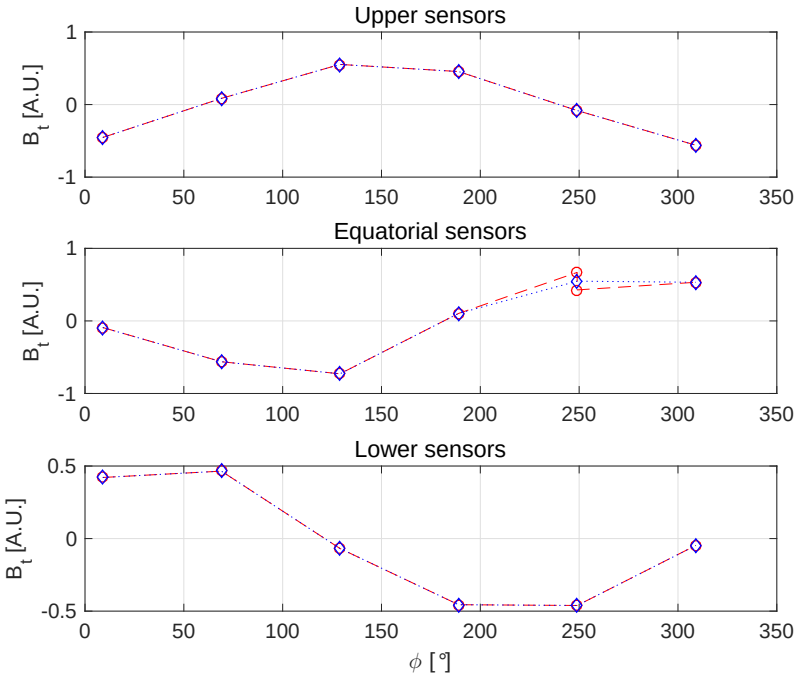

(b)

Figure 61: Image of the two unstable eigenmodes on the three sensor arrays: $\gamma_1 = 551s^{-1}$ (a) and $\gamma_2 = 402s^{-1}$ (b). The actual available measurements are given by red circles and the interpolated field by blue diamonds.

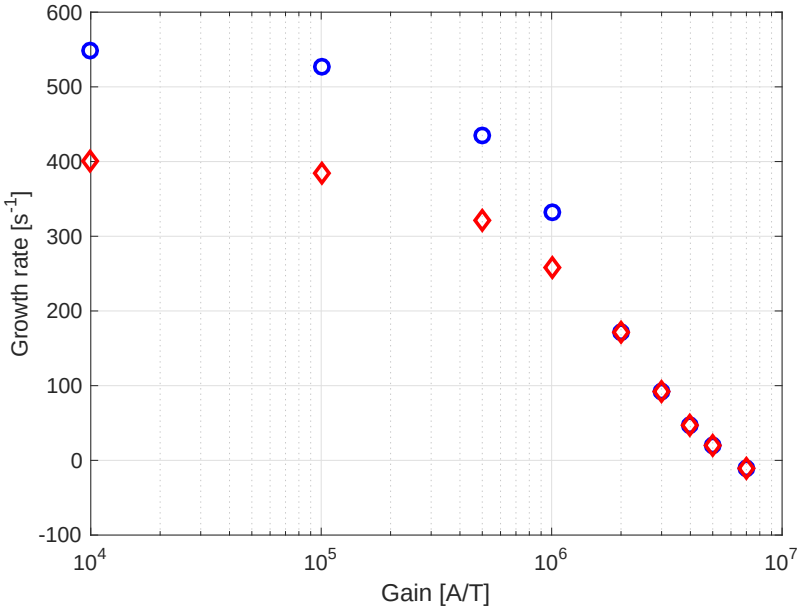

Figure 62: Eigenvalue study on the critical proportional gain required to stabilize the two modes with all the available active coils.

fast initial phase (0.01 s – 0.012 s) during which its amplitude rapidly decreases. Once the faster components have decayed the growth rate stabilizes around the expected eigenvalue. This behavior is consistent with results obtained with similar control strategies [82]. The full output of the time simulation has been considered to investigate the current required by the applied control scheme. For the most stabilizing case ($K_p = 8 \times 10^6$ A/T) the simulated magnetic field (tangential component), as measured by all the sensors, and the current flowing in each active coil is shown in Figure 64. The resulting Ampere-turns are compatible with the rated current of JT-60SA power supplies, as described in Section 5.2, and Table 2 in particular.

10.4 CONCLUSIONS

As a result of the above discussion we can conclude that Resistive Wall Mode active stabilization has been achieved in a representative of JT-60SA Scenario 5.1 plasma, with a model including realistic 3D description of the passive and active structures. The core of this model is represented by the CarMa code. A series of tools have been developed that allow user-friendly implementation of different control schemes. Both eigenvalue analyses of the closed-loop system and full time simulations

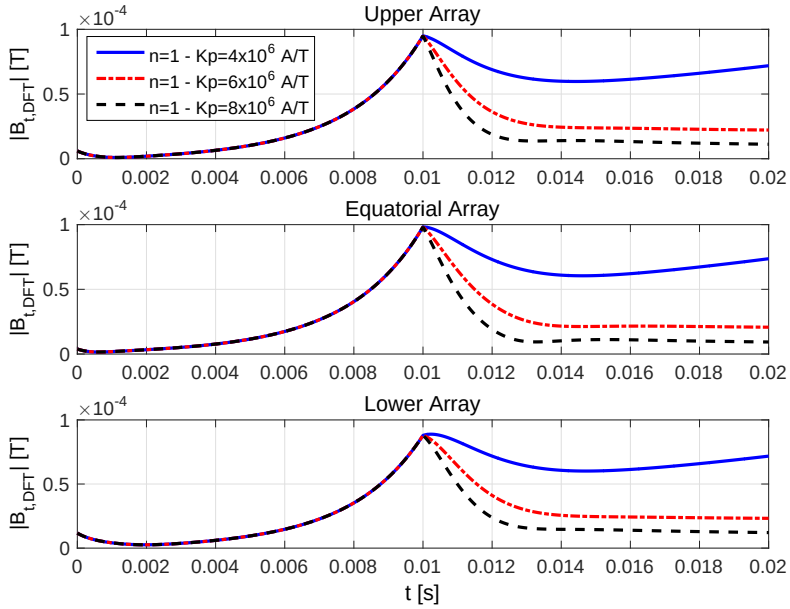

Figure 63: Amplitude of the n=1 component calculated from the tangential field measurements on each sensor array. Three different proportional gains are applied after a 10 ms lasting free evolution.

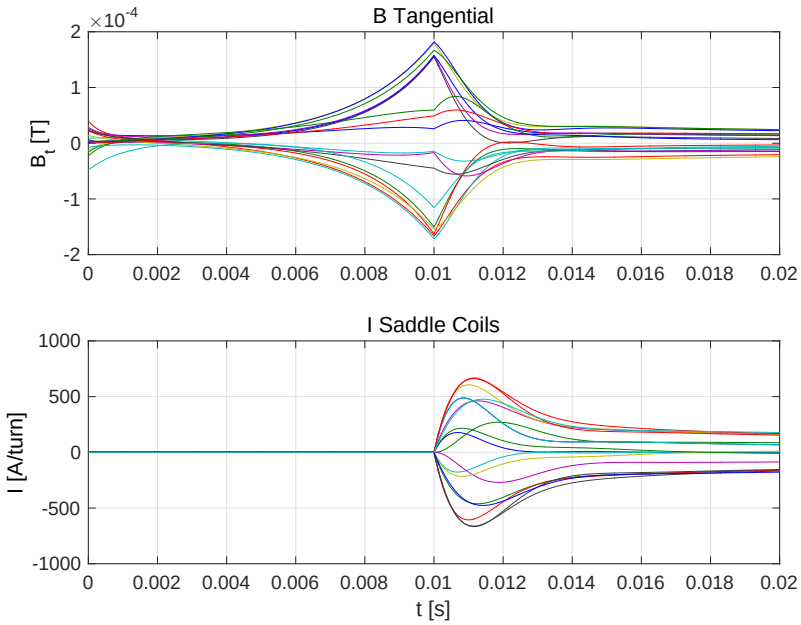

Figure 64: Tangential field (upper plot) and coil current (lower plot) for each sensor and each active coil, example taken from the highest gain case $K_p = 8 \times 10^6$ A/T.

can be performed thanks to the dedicated dynamic simulator which has been described in the present work. A purely proportional control strategy has been implemented, with an ideal current controller. Future work will involve the development of a voltage input system, with realistic evaluation of the current loop and implementation of a full PID controller. This improvement will allow increasing the level of detail in the simulations and expanding the range of applicable control schemes. The independence of the actuators is inherent in the model and it will be exploited in the future to test different control strategies, the possibility of acting with different sets of coils on different modes is also an important possibility to be exploited given the possible multi-modal nature of the instability spectrum in high β plasmas.

AFTERWORD

The work carried out during the three years of the Ph.D. program has been thoroughly described in the chapters of this thesis, and the main results already summarized in dedicated conclusion sections. As a global overview, this work has addressed a series of relevant topics for the exploitation of present and future fusion experimental devices.

With the main focus being set on ideal MHD instabilities and realistic magnetic boundaries, the first part has been devoted to fine tuning and optimization of the RFX-mod control system, developing a series of techniques that are simple enough to be implemented in real-time operation yet bringing noticeable effects. The missing coil compensation in particular has been applied in experiments referring to different topics, and it can be generally implemented to virtually any device with a set of actuators and a given degree of flexibility. The modeling activity on multi-modal RWM feedback control in RFP plasmas has extended previous work and investigated the coupling phenomena between different poloidal harmonics. A similar approach could be applied to a completely different range of plasmas, the high β_N Advanced Tokamak scenarios, in which the q profiles and high pressure would make multiple n RWMs unstable.

The second part of the thesis has investigated RWM physics in this kind of plasmas, with reference to the JT-60SA experiment which is under construction in Japan. A study of the kinetic effects in mode damping physics has been carried out, highlighting that the drift-kinetic contribution to stability, although small for β_N values close to the ideal-wall limit, is nevertheless important and possibly fundamental for RWM control. Feedback stabilization has also been considered with a proof-of-principle study. In this work the basis has been given for future analyses of RWM active control on JT-60SA. In the near future developments on this side are foreseen, with improvement of the implemented dynamic simulator and studies on possible control schemes. The obtained results are encouraging that strong instabilities such as RWMs could be controlled in future devices with a combination of plasma rotation (coupled

to drift-kinetic effects) and magnetic feedback. This represents a major step towards the development of high β operational scenarios.

ACKNOWLEDGMENTS

During my time at Consorzio RFX as a Ph.D. student, and before that while working at my M.Sc. thesis, I have found support and friendship in many people. In particular I thank Dr. Tommaso Bolzonella for being my mentor, for his guidance and advice that has played an important role in developing my professional profile. I thank Prof. Paolo Bettini for his literally constant support, by both proposing new things and backing my own ideas. I would also like to thank Dr. Giuseppe Marchiori, with whom I enjoy working and whose advice is always precious. For the always entertaining chats, and for the comments on part of this thesis, I thank Dr. Marco Veranda. Aside from my research activities, I have been involved in the organization of scientific events, which has proven to be a very instructive experience. For this opportunity, and for her commitment, I thank Margherita Basso.

For teaching me so much, introducing me to the part of my work that perhaps I enjoy the most, for always answering my questions from literally anywhere around the world, for his guidance, I want to thank Dr. Yueqiang Liu.

Of the many things done in the past three years, most I have shared with the colleagues and friends of my doctorate cycle; for this I thank Tautvydas J. Maceina, Yangyang Zhang, Carlo Baltador, Marco Gottardo and Alberto Maistrello. Along with them I also thank all the friends who have somehow contributed to the office life: Matteo Zaupa, Matteo Vallar, Daniele Aprile, Flavia Raggi, Daniele Maggio, Ondřej Kudláček, Oisin McCormack, Ferdinando Gasparini, Gustavo Grenfell (thanks for translating the abstract into Portuguese!), Mattia Dan, Michele Fadone, Dario Friso, Marco Barbisan, Marco Zanini, Pietro Vincenzi, Nicolò Visonà, Vadim Yanovskiy, Nisarg Patel.

BIBLIOGRAPHY

[1] VV.AA. *Fusion Physics*. IAEA.

[2] Jeffrey P. Freidberg. *Plasma Physics and Fusion Energy*. Cambridge, MA, USA: Cambridge University Press, 2007.

[3] J. Wesson. *Tokamaks*. 3rd. Oxford University Press, 2004.

[4] Jeffrey P. Freidberg. *Ideal Magnetohydrodynamics*. Cambridge, MA, USA: Plenum publishing, 1987.

[5] Dalton D. Schnack. *Lectures in magnetohydrodynamics: with an appendix on extended MHD*. Vol. 780. Springer, 2009.

[6] V.D. Shafranov. In: *Soviet Phys. Tech. Phys* 15 (1970), p. 175.

[7] I.B. Bernstein, E.A. Frieman, M.D. Kruskal, and R.M. Kulsrud. «An energy principle for hydromagnetic stability problems.» In: *Proceedings of the Royal Society of London A: Mathematical, Physical and Engineering Sciences*. Vol. 244. The Royal Society, 1958. Chap. 1236, pp. 17–40.

[8] F. Troyon, R. Gruber, H. Saurenmann, S. Semenzato, and S. Succi. «MHD-limits to plasma confinement.» In: *Plasma Physics and Controlled Fusion* 26.1A (1984), p. 209.

[9] D. Pfirsch and H. Tasso. «A theorem on MHD-instability of plasmas with resistive walls.» In: *Nuclear Fusion* 11.3 (1971), p. 259.

[10] A. Bondeson and DJ Ward. «Stabilization of external modes in tokamaks by resistive walls and plasma rotation.» In: *Physical Review Letters* 72.17 (1994), p. 2709.

[11] M.S. Chu and M. Okabayashi. «Stabilization of the External Kink and the Resistive Wall Mode.» In: *Plasma Phys. Control. Fusion* 52 (2010), p. 123001.

[12] B. Hu and R. Betti. «Resistive wall mode in collisionless quasistationary plasmas.» In: *Physical Review Letters* 93.10 (2004), p. 105002.

[13] S. Takeji, S. Tokuda, T. Fujita, T. Suzuki, A. Isayama, S. Ide, Y. Ishii, Y. Kamada, Y. Koide, and T. Matsumoto. «Resistive instabilities in reversed shear discharges and wall stabilization on JT-60U.» In: *Nuclear Fusion* 42.1 (2002), p. 5.

[14] G. Matsunaga, M. Takechi, G. Kurita, T. Ozeki, and Y. Kamada. «Effect of plasma-wall separation on the stability of resistive wall modes in the JT-60U tokamak.» In: *Plasma Physics and Controlled Fusion* 49.1 (2006), p. 95.

[15] EJ Strait, TS Taylor, AD Turnbull, JR Ferron, LL Lao, B. Rice, O. Sauter, SJ Thompson, and D. Wroblewski. «Wall stabilization of high beta tokamak discharges in DIII-D.» In: *Physical Review Letters* 74.13 (1995), p. 2483.

[16] TS Taylor, EJ Strait, LL Lao, M. Mauel, AD Turnbull, KH Burrell, MS Chu, JR Ferron, RJ Groebner, and RJ La Haye. «Wall stabilization of high beta plasmas in DIII-D.» In: *Physics of Plasmas (1994-present)* 2.6 (1995), pp. 2390–2396.

[17] M. Takechi, G. Matsunaga, N. Aiba, T. Fujita, T. Ozeki, Y. Koide, Y. Sakamoto, G. Kurita, A. Isayama, and Y. Kamada. «Identification of a low plasma-rotation threshold for stabilization of the resistive-wall mode.» In: *Physical Review Letters* 98.5 (2007), p. 055002.

[18] EJ Strait, AM Garofalo, GL Jackson, M. Okabayashi, H. Reimerdes, MS Chu, R. Fitzpatrick, RJ Groebner, Y. In, and RJ LaHaye. «Resistive wall mode stabilization by slow plasma rotation in DIII-D tokamak discharges with balanced neutral beam injectiona).» In: *Physics of Plasmas (1994-present)* 14.5 (2007), p. 056101.

[19] JM Finn. «Stabilization of ideal plasma resistive wall modes in cylindrical geometry: the effect of resistive layers.» In: *Physics of Plasmas (1994-present)* 2.10 (1995), pp. 3782–3791.

[20] R. Betti. «Beta limits for the N=1 mode in rotating-toroidal-resistive plasmas surrounded by a resistive wall.» In: *Physics of Plasmas (1994-present)* 5.10 (1998), pp. 3615–3631.

[21] A Bondeson and HX Xie. «Stability of ideal and resistive modes in cylindrical plasmas with resistive walls and plasma rotation.» In: *Physics of Plasmas (1994-present)* 4.6 (1997), pp. 2081–2089.

[22] VD Pustovitov. «Energy principle for the modes interacting with a resistive wall in toroidal systems.» In: *Nuclear Fusion* 55.3 (2015), p. 033008.

[23] VV Yanovskiy. «Plasma-resistivity-induced strong destabilization of the kinetic resistive wall mode.» In: *Physics of Plasmas (1994-present)* 23.10 (2016), p. 102510.

[24] EJ Strait, AM Garofalo, ME Austin, JM Bialek, MS Chu, ED Fredrickson, LL Lao, RJ La Haye, EA Lazarus, and G. McKee. «Observation and control of resistive wall modes.» In: *Nuclear Fusion* 39.11Y (1999), p. 1977.

[25] TC Hender, JC Wesley, J. Bialek, A. Bondeson, AH Boozer, RJ Buttery, A. Garofalo, TP Goodman, RS Granetz, and Y. Gribov. «MHD stability, operational limits and disruptions.» In: *Nuclear Fusion* 47.6 (2007), S128.

[26] VD Pustovitov. «Plasma stability theory including the resistive wall effects.» In: *Journal of Plasma Physics* 81.06 (2015), p. 905810609.

[27] R. Betti and JP Freidberg. «Stability analysis of resistive wall kink modes in rotating plasmas.» In: *Physical Review Letters* 74.15 (1995), p. 2949.

[28] MS Chu, JM Greene, TH Jensen, RL Miller, A. Bondeson, RW Johnson, and ME Mauel. «Effect of toroidal plasma flow and flow shear on global magnetohydrodynamic MHD modes.» In: *Physics of Plasmas (1994-present)* 2.6 (1995), pp. 2236–2241.

[29] ZR Wang, SC Guo, and YQ Liu. «Drift kinetic effects on the resistive wall mode stability: Comparison between reversed field pinches and tokamaks.» In: *Physics of Plasmas (1994-present)* 19.7 (2012), p. 072518.

[30] JE Menard, Z. Wang, Y. Liu, RE Bell, SM Kaye, J-K Park, and K. Tritz. «Rotation and Kinetic Modifications of the Tokamak Ideal-Wall Pressure Limit.» In: *Physical Review Letters* 113.25 (2014), p. 255002.

[31] ZR Wang, MJ Lanctot, YQ Liu, JK Park, and JE Menard. «Three-Dimensional Drift Kinetic Response of High-Beta Plasmas in the DIII-D Tokamak.» In: *Physical Review Letters* 114.14 (2015), p. 145005.

[32] YQ. Liu, MS Chu, I.T. Chapman, and T.C. Hender. «Toroidal self-consistent modeling of drift kinetic effects on the resistive wall mode.» In: *Physics of Plasmas (1994-present)* 15.11 (2008), p. 112503.

[33] B. Hu, R. Betti, and J. Manickam. «Application of the low-frequency energy principle to wall modes.» In: *Physics of Plasmas* 12.5 (2005), pp. 57301–57301.

[34] T. Bolzonella, M. Cavinato, E. Gaio, L. Grando, A. Luchetta, G. Manduchi, G. Marchiori, L. Marrelli, R. Paccagnella, and A. Soppelsa. «Feedback control of resistive wall modes by saddle coils in RFX-mod.» In: *Fusion Engineering and Design* 82.5 (2007), pp. 1064–1072.

[35] T. Bolzonella, V. Igochine, S.C. Guo, D. Yadikin, M. Baruzzo, and H. Zohm. «Resistive-Wall-Mode Active Rotation in the RFX-Mod Device.» In: *Physical Review Letters* 101 (2008), p. 165003.

[36] M. Baruzzo, T. Bolzonella, Y.Q. Liu, G. Manduchi, G. Marchiori, A. Soppelsa, M. Takechi, and F. Villone. «RWM control studies on RFX-mod with a limited set of active coils.» In: *Nuclear Fusion* 52 (2012), 103001 (13pp).

[37] M.S. Chu, M.S. Chance, A.H Glasser, and M. Okabayashi. «Normal mode approach to modelling of feedback stabilization of the resistive wall mode.» In: *Nucl. Fusion* 41 (2007), pp. 1425–1436.

[38] C. M. Bishop. «An Intelligent Shell for the Toroidal Pinch.» In: *Plasma Phys. Control. Fusion* 31 (1989), p. 1179.

[39] P. Zanca, L. Marrelli, G. Manduchi, and G. Marchiori. «Beyond the Intelligent Shell Concept: the Clean-Mode-Control.» In: *Nucl. Fusion* 47 (2007), pp. 1425–1436.

[40] YQ Liu, Anders Bondeson, Carl-Magnus Fransson, Bengt Lennartson, and Claes Breitholtz. «Feedback stabilization of nonaxisymmetric resistive wall modes in tokamaks. I. Electromagnetic model.» In: *Physics of Plasmas (1994-present)* 7.9 (2000), pp. 3681–3690.

[41] V.D. Pustovitov. «Comparison of RWM feedback systems with different input signals.» In: *Plasma Physics and Controlled Fusion* 44.3 (2002), p. 295.

[42] L.A. Artsimovich. «Tokamak Devices.» In: *Nuclear Fusion* 12 (1972).

[43] R.J. Bickerton, J.W. Connor, and J.B. Taylor. «Diffusion Driven Plasma Currents and Bootstrap Tokamak.» In: *Nature Physical Science* 229 (1971), pp. 110–112.

[44] C. Kessel, Jf Manickam, G. Rewoldt, and WM Tang. «Improved plasma performance in tokamaks with negative magnetic shear.» In: *Physical Review Letters* 72.8 (1994), p. 1212.

[45] A.D. Turnbull, T.S. Taylor, YR Lin-Liu, and H. St John. «High beta and enhanced confinement in a second stable core VH-mode advanced tokamak.» In: *Physical Review Letters* 74.5 (1995), p. 718.

[46] EJ Strait, LL Lao, ME Mauel, BW Rice, TS Taylor, KH Burrell, MS Chu, EA Lazarus, TH Osborne, and SJ Thompson. «Enhanced confinement and stability in DIII-D discharges with reversed magnetic shear.» In: *Physical Review Letters* 75.24 (1995), p. 4421.

[47] D.A. Baker and W.E. Quinn. *Fusion*. Ed. by Edward Teller. Vol. 1. Academic Press, 1981, pp. 438–471.

[48] G. Rostagni. In: *Fusion Engineering and Design* 25 (1995), pp. 301–313.

[49] S. Ortolani and D.D. Schnack. *Magnetohydrodynamics of Plasma Relaxation*. World Scientific, 1993.

[50] J.B. Taylor. «Relaxation of Toroidal Plasma and Generation of Reverse Magnetic Fields.» In: *Physical Review Letters* 33.19 (1974).

[51] V. Antoni, D. Merlin, S. Ortolani, and R. Paccagnella. «MHD Stability Analysis of Force-Free Reversed Field Pinch Configurations.» In: *Nuclear Fusion* 26.12 (1986), pp. 1711–1717.

[52] S. Cappello and DF Escande. «Bifurcation in viscoresistive MHD: The Hartmann number and the reversed field pinch.» In: *Physical Review Letters* 85.18 (2000), p. 3838.

[53] PR Brunsell, Y. Yagi, Y. Hirano, Y. Maejima, and T. Shimada. «Coherent magnetic field fluctuations and locked modes in a reversed-field pinch.» In: *Physics of Fluids B: Plasma Physics (1989-1993)* 5.3 (1993), pp. 885–895.

[54] S. Cappello, DF Escande, L. Marrelli, P. Martin, E. Martines, S. Ortolani, G. Spizzo, D. Terranova, and P. Zanca. «Stationary quasi single helicity states in RFX.» In: *Proc. 26th EPS Conf. on Controlled Fusion and Plasma Physics (Maastricht, 1999)*. 1999.

[55] P. Martin. «Magnetic and thermal relaxation in the reversed field pinch.» In: *Plasma Physics and Controlled Fusion* 41.3A (1999), A247.

[56] DF Escande, P. Martin, S. Ortolani, A. Buffa, P. Franz, L. Marrelli, E. Martines, G. Spizzo, S. Cappello, and A. Murari. «Quasi-single-helicity reversed-field-pinch plasmas.» In: *Physical Review Letters* 85.8 (2000), p. 1662.

[57] R. Lorenzini, E. Martines, P. Piovesan, D. Terranova, P. Zanca, M. Zuin, A. Alfier, D. Bonfiglio, F. Bonomo, and A. Canton. «Self-organized helical equilibria as a new paradigm for ohmically heated fusion plasmas.» In: *Nature Physics* 5.8 (2009), pp. 570–574.

[58] P. Piovesan, D. Bonfiglio, F. Auriemma, F. Bonomo, L. Carraro, R. Cavazzana, G. De Masi, A. Fassina, P. Franz, and M. Gobbin. «RFX-mod: A multi-configuration fusion facility for three-dimensional physics studiesa).» In: *Physics of Plasmas (1994-present)* 20.5 (2013), p. 056112.

[59] L. Marrelli, P. Zanca, M. Valisa, G. Marchiori, A. Alfier, F. Bonomo, M. Gobbin, P. Piovesan, D. Terranova, and M. Agostini. «Magnetic self organization, MHD active control and confinement in RFX-mod.» In: *Plasma Physics and Controlled Fusion* 49.12B (2007), B359.

[60] Yueqiang Liu, IT Chapman, JP Graves, GZ Hao, ZR Wang, JE Menard, M. Okabayashi, EJ Strait, and A. Turnbull. «Non-perturbative modelling of energetic particle effects on resistive wall mode: Anisotropy and finite orbit widtha).» In: *Physics of Plasmas (1994-present)* 21.5 (2014), p. 056105.

[61] TM Antonsen Jr and YC Lee. «Electrostatic modification of variational principles for anisotropic plasmas.» In: *Physics of Fluids (1958-1988)* 25.1 (1982), pp. 132–142.

[62] Francesco Porcelli, R. Stankiewicz, W. Kerner, and HL Berk. «Solution of the drift kinetic equation for global plasma modes and finite particle orbit widths.» In: *Physics of Plasmas (1994-present)* 1.3 (1994), pp. 470–480.

[63] YQ Liu, MS Chu, WF Guo, F. Villone, R. Albanese, G. Ambrosino, M. Baruzzo, T. Bolzonella, IT Chapman, and AM Garofalo. «Resistive wall mode control code maturity: progress and specific examples.» In: *Plasma Physics and Controlled Fusion* 52.10 (2010), p. 104002.

[64] B. Hu, R. Betti, and J. Manickam. «Kinetic stability of internal kink mode in ITER.» In: *APS Meeting Abstracts*. Vol. 1. 2006, 1038P.

[65] S.W. Haney and J.P. Freidberg. «Variational methods for studying tokamak stability in the presence of a thin resistive wall.» In: *Physics of Fluids B: Plasma Physics (1989-1993)* 1.8 (1989), pp. 1637–1645.

[66] James A. Cadzow and Hinrich R. Martens. *Discrete-Time and Computer Control Systems*. Electrical Engineering Series. Prentice-Hall, 1970.

[67] J. Bechhoefer. «Feedback for physicists: A tutorial essay on control.» In: *Reviews of Modern Physics* 77 (2005), 783(54).

[68] H.A.B. Bodin and A.A. Newton. «Reversed-field-pinch research.» In: *Nuclear Fusion* 20.10 (1980), p. 1255.

[69] S. Ortolani. «Active MHD control experiments in RFX-mod.» In: *Plasma Physics and Controlled Fusion* 48.12B (2006), B371.

[70] P. Sonato et al. «Machine modification of active MHD control in RFX.» In: *Fusion Engineering and Design* 66-68 (2003), pp. 161–168.

[71] N Patel, M Dalla Palma, S Dal Bello, L Grando, S Peruzzo, and P Sonato. «Vacuum boundary modifications of the RFX-mod machine.» In: *Fusion Engineering and Design* (2016).

[72] S. Ishida, P. Barabaschi, and Y. Kamada. «Overview of the JT-60SA project.» In: *Nuclear Fusion* 51.9 (2011), p. 094018.

[73] Y. Kamada, P. Barabaschi, and S. Ishida. «Progress of the JT-60SA project.» In: *Nuclear Fusion* 53.10 (2013), p. 104010.

[74] Y. Kamada, P. Barabaschi, S. Ishida, S. Ide, K. Lackner, T. Fujita, T. Bolzonella, T. Suzuki, G. Matsunaga, and M. Yoshida. «Plasma regimes and research goals of JT-60SA towards ITER and DEMO.» In: *Nuclear Fusion* 51.7 (2011), p. 073011.

[75] A. Ferro, E. Gaio, M. Tomasini, P. Milani, E. Massarelli, M. Matsukawa, and L. Novello. «A 72 kVA very fast four-quadrant converter based on hybrid Si-SiC IGBTs.» In: *17th European Conference on Power Electronics and Applications (EPE'15 ECCE-Europe), 2015*. IEEE, 2015, pp. 1–10.

[76] L. Piron, L. Grando, G. Marchiori, L. Marrelli, P. Piovesan, A. Soppelsa, and D. Terranova. «Dynamic decoupling and multi-mode magnetic feedback for error field correction in RFX-mod.» In: *Nuclear Fusion* 51.6 (2011), p. 063012.

[77] G. Marchiori and A. Soppelsa. «Development and validation of an electromagnetic model of the active control system of MHD modes in RFX-mod.» In: *Fusion Engineering and Design* 82 (2007), pp. 1015–1022.

[78] L. Pigatto, P. Bettini, T. Bolzonella, G. Marchiori, and F. Villone. «MHD control system optimization to RFX-mod real passive boundary.» In: *41st EPS Conference on Plasma Physics*. Berlin, 2014.

[79] Gianfranco Cariolaro. *Unified signal theory*. Springer Science and Business Media, 2011.

[80] L. Pigatto, P. Bettini, T. Bolzonella, G. Marchiori, and F. Villone. «Optimal strategies for real-time sparse actuator compensation in RFX-mod MHD control operations.» In: *Fusion Engineering and Design* 96-97 (2015), pp. 690–693. DOI: 10.1016/j.fusengdes.2015.06.066.

[81] R. Albanese, Y.Q. Liu, A. Portone, G. Rubinacci, and F. Villone. «Coupling Between a 3-D Integral Eddy Current Formulation and a Linearized MHD Model for the Analysis of Resistive Wall Modes.» In: *IEEE Transactions on Magnetics* 44.6 (2008), pp. 1654–1657.

[82] G. Marchiori, M. Baruzzo, T. Bolzonella, Y.Q. Liu, A. Soppelsa, and F. Villone. «Dynamic simulator of RWM control for fusion devices: modelling and experimental validation in RFX-mod.» In: *Nuclear Fusion* 52 (2012), 023020 (12pp).

[83] P. Fiorentin and N. Pomaro. «Design of a new electromagnetic diagnostic for RFX.» In: *Fusion Engineering and Design* 66 (2003), pp. 871–876.

[84] P. Sonato and P. Zaccaria. «Thermal fluxes due to plasma-wall interactions: Experimental measurements and numerical analyses.» In: *Fusion Engineering and Design* 39 (1998), pp. 401–408.

[85] F. Villone, YQ Liu, R. Paccagnella, T. Bolzonella, and G. Rubinacci. «Effects of three-dimensional electromagnetic structures on resistive-wall-mode stability of reversed field pinches.» In: *Physical Review Letters* 100.25 (2008), p. 255005.

[86] Yueqiang Liu. «Effects of Alpha particles on the resistive wall mode stability in ITER.» In: *Nuclear Fusion* 50.9 (2010), p. 095008.

[87] JF Artaud, V. Basiuk, F. Imbeaux, M. Schneider, J. Garcia, G. Giruzzi, P. Huynh, T. Aniel, F. Albajar, and JM Ane. «The CRONOS suite of codes for integrated tokamak modelling.» In: *Nuclear Fusion* 50.4 (2010), p. 043001.

[88] M. Honda and A. Fukuyama. «Comparison of turbulent transport models of L-and H-mode plasmas.» In: *Nuclear Fusion* 46.5 (2006), p. 580.

[89] J. Garcia, N. Hayashi, B. Baiocchi, G. Giruzzi, M. Honda, S. Ide, P. Maget, E. Narita, M. Schneider, and H. Urano. «Physics comparison and modelling of the JET and JT-60U core and edge: towards JT-60SA predictions.» In: *Nuclear Fusion* 54.9 (2014), p. 093010.

[90] VV.AA. *JT-60SA Research Plan - Research Objectives and Strategy Version 3.2*. 2015. URL: http://www.jt60sa.org/pdfs/JT-60SA_Res_Plan.pdf.

[91] X. Xu. *Theoretical studies of resistive wall mode and fishbone-like external kink mode in RFP plasmas and comparison with tokamaks*. 2015. URL: http://paduaresearch.cab.unipd.it/7596/.

[92] M. Honda, S. Satake, Y. Suzuki, M. Yoshida, N. Hayashi, K. Kamiya, A. Matsuyama, K. Shinohara, G. Matsunaga, and M. Nakata. «Integrated modelling of toroidal rotation with the 3D non-local drift-kinetic code and boundary models for JT-60U analyses and predictive simulations.» In: *Nuclear Fusion* 55.7 (2015), p. 073033.

[93] S. Ide, N. Aiba, T. Bolzonella, C. Challis, T. Fujita, G. Giruzzi, E. Joffrin, K. Hamamatsu, N. Hayashi, and M. Honda. «Optimization of JT-60SA plasma operational scenario with capabilities of installed actuators.» In: *Proc. the 24th IAEA Fusion Energy Conf.(San Diego, CA, 2012)*. 2012.

[94] S. Mastrostefano, P. Bettini, T. Bolzonella, M. Furno Palumbo, YQ Liu, G. Matsunaga, R. Specogna, M. Takechi, and F. Villone. «Three-dimensional analysis of JT-60SA conducting structures in view of RWM control.» In: *Fusion Engineering and Design* 96 (2015), pp. 659–663.

[95] P. Zanca, L. Marrelli, R. Paccagnella, A. Soppelsa, M. Baruzzo, T. Bolzonella, G. Marchiori, P. Martin, and P. Piovesan. «Feedback control model of the m= 2, n= 1 resistive wall mode in a circular plasma.» In: *Plasma Physics and Controlled Fusion* 54.9 (2012), p. 094004.